



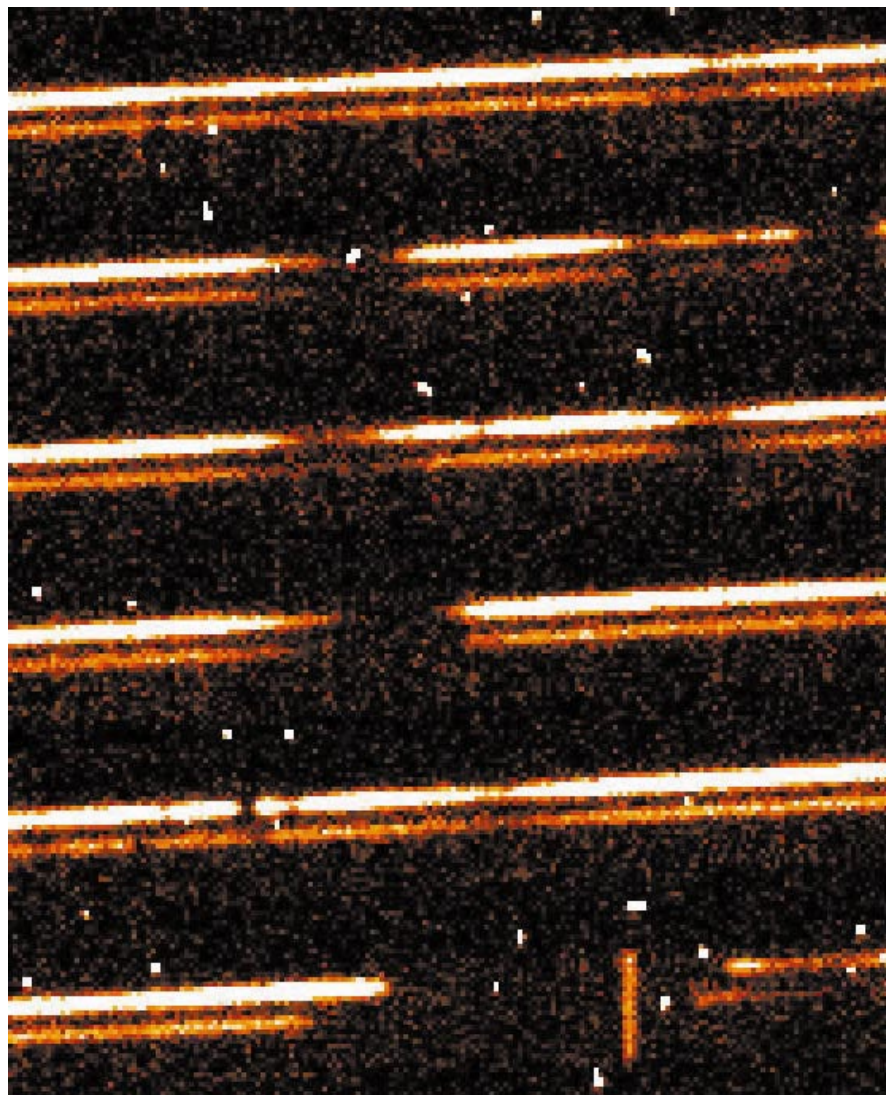
No. 99 – March 2000

Successful Commissioning of UVES at Kueyen

Finally, we are there: as of April 1, 2000, UVES, the UV-Visual Echelle Spectrograph built by ESO, will start operation at the Nasmyth focus of the VLT telescope Kueyen. The instrument commissioning has been completed in December 1999, eight years after the first proposal to build a high-resolution spectrograph for the VLT was circulated and in perfect schedule with the first detailed VLT planning dated March 1994. UVES will be the third instrument after FORS1 and ISAAC to enter into regular use at the VLT. The second version of FORS, FORS2, will start operating at the same date at the Cassegrain focus of the telescope.

The figure to the right is an unprocessed section of a 1-hour integration in the blue arm showing the central portion of a few echelle orders centred at 380 nm. It clearly illustrates some of UVES prime capabilities: the UV-blue efficiency and the image quality of the atmosphere/telescope/spectrograph system (see page 2).

The two parallel tracings correspond to the two images of a gravitationally lensed QSO (HE1104-1805) separated on the sky by 3.2 arcsec, blue magnitudes ~ 16.7 and 18.6 respectively. The CCD was read-out in binned 2×2 mode. The vertical line at the bottom is a sky-emission line and it visualises well the spectral resolution of $\sim 55,000$. The redshifts, widths and equivalent widths of the absorption lines along the 2 lines of sight provide a mini-"tomography" of the intergalactic/interstellar medium up to the distance corresponding to $z = 2.1$. Some of the broad absorption lines (Ly α) and the narrow metal absorption (e.g. in the second order from the bottom) reveal column density and velocity variations over a scale of a few kpc.



UVES at Kueyen: Bright Prospects for High-Resolution Spectroscopy at the VLT

S. D'ODORICO, ESO

After the successful completion of the commissioning period, the UV-Visual Echelle Spectrograph starts regular operation at the Paranal Observatory.

Introduction

The ESO scientific community has a rich tradition of research based on the detailed analysis of high-resolution spectra of stars. One of the very first spectrographs to enter into operation at ESO was in 1968 the coudé high-resolution spectrograph at the 1.52-m at La Silla, followed in 1973 by the Echelec at the same telescope.

The first ESO-built echelle spectrograph for the 3.6-m, CASPEC, was installed in 1983 and opened the possibility to study faint stellar and extragalactic sources, thanks to its new (at that time almost exotic) CCD detector (a high efficiency 320×512 RCA CCD, with a read-out-noise of $40 e^-/\text{pixel}$ and a dark current of $15 e^-/\text{hr}/\text{pixel}$). For the first time, the ESO community had access to an instrument that was fully competitive with, and in some areas superior to, other high-resolution spec-

trographs at large telescopes worldwide. CASPEC was followed by the CES spectrograph coupled to the 1.5-m CAT giving resolving powers larger than 100,000 on stars down to magnitudes ~ 10 and in 1991 by the echelle mode of the EMMI spectrograph at the NTT, which again offered optimal performance in $R = 25,000$ spectroscopy of faint sources in the visual-red spectral region.

In 1993, the HIRES echelle spectrograph came into operation at the first 10-m Keck telescope. The excellent quality of the instrument and the collecting power of the largest telescope ever built successfully combined to form a unique tool for all programmes, which require spectra of faint targets at resolution up to 50,000 in the 400–800 nm range. ESO astronomers working on research topics, which rely on high-resolution spectra, for both stellar and extragalactic targets, often had to face

a powerful, almost unbeatable competition or to concentrate on objects at declinations lower than -40 degrees. After six years of justified frustration, the ESO community has now access to an instrument, UVES, which is more efficient, provides larger spectral coverage in a single exposure, and can reach higher resolving power with proper sampling than its main competitor in its present configuration.

Not surprisingly, in the first semester of Kueyen observations (Period 65, starting April 1, 2000), about 70% of the time has been assigned to UVES observations. The Observing Programmes Committee has selected programmes for 78 nights in UVES visitor mode and for 312 hours of service observations. Scanning through the titles of these approved programmes, we find most of the research topics identified as scientific drivers of the instrument when it was first proposed. Going from the very close to the distant universe, UVES observations will aim at highly accurate radial velocity measurements of nearby stars to search for associated planets, at the determination of the abundance of various critical elements in the atmospheres of stars in the Galaxy and in nearby systems and at the study of absorption systems down to the atmospheric cut-off in QSO's spectra.

The Instrument Layout

There are a few basic choices taken early in the project which have been crucial in determining its present good performance: the configuration fixed with respect to gravity (advantages: less weight and space restrictions, more stability, shortcomings: need of derotator and more relay optics), the splitting of the optical path in a UV-blue and in a visual-red arm (giving the possibility to optimise the efficiency over the entire spectral range from 300 to 1000 nm) and the early selection of detectors of a format ($2k \times 4k$, $15 \mu\text{m}$ pixels) for which we had to find a supplier who would deliver to specifications. The optical design of both arms is of the



Figure 1: This aerial view of the Nasmyth platform of Kueyen at the end of the integration shows UVES with the top of its enclosure partially lifted to have access to the table where the various components are mounted. The bar connecting the enclosure to the telescope fork is for safety in case of earthquake.

white pupil type. To maximise the resolution while keeping the beam size reasonable (200 mm) we went for two 214 × 840 mm mosaics (each made by two replicas on a single blank) R4 echelle gratings, the first ones of this type and size ever produced. The design of UVES is fully ESO made, the various components were produced in Europe and the USA: the optics in France, the mechanics in Germany and Switzerland, the gratings in the USA and Russia, the detectors in the UK and USA and most of the high-level software in Italy at the Observatory of Trieste.

Two main parts compose UVES (see Fig. 1). The preslit area is attached to the Nasmyth rotator and includes the *calibration unit* with the arc lamp and different FF lamps for each spectral range, an insertable *iodine cell*, a slide mounting three *image slicers* for observations at the highest resolution in mediocre seeing conditions and the *derotator*. Along the optical path, now on the steel table bolted to the Nasmyth platform, the beam encounters the *atmospheric dispersion corrector*, a *depolarise slide*, a *variable pupil stop* and the *arm selector unit*, which can feed the two arms individually or in parallel with *dichroics*. The blue and red *slit units* are adjustable in width and height, they reflect the light over a field of 30 arcsec diameter to two CCDs which are used for target acquisition and centring, for monitoring the telescope guiding and for recording the slit position on the sky. After the slits, each of the two parallel arms (which intersect each other to minimise the overall volume) includes an *order sorter filter wheel*, the *collimator mirrors*, the *echelle grating*, the *exposimeter* and the *cross-disperser unit* with two gratings mounted back to back. The *cameras* are dioptric with an external focus to facilitate detector exchange; the largest lenses are CaF₂ (220 mm di-



Figure 2: During the frantic days of the instrument integration at the telescope, J.L. Lizon takes advantage of the robust design of the UVES functions for a short rest. Most of the subsystems are already mounted on the table fixed to the Nasmyth platform: from the left the preslit units, the shiny back of the blue echelle mount, the blue CD unit, camera and CCD.

ameter) and SFPL51 (246 mm) in the blue and red respectively. The blue-arm CCD is an EEV-44 device with enhanced UV efficiency (55% at 340nm). The red detector is a mosaic of one EEV-44 device and one MIT-LL CCID-20 device, to optimise the spectral response with wavelength. The CCDs are operated by the ESO-built FIERA controller. In the configurations they are offered in UVES, both detectors are read out in ~ 40 s with a rather good r.o.n. of 2 and 4 e⁻ r.m.s. The operating temperature of the CCDs (~ 150° K) is maintained by liquid nitrogen fed from a tank which secures an autonomy of at least 10 days. The table is protected from dust and light by a motorised enclosure that can be lifted to give access to the functions. It provides a passive thermal insulation which, combined with the air conditioning of the telescope enclosure during the day, smoothes out the temperature variations inside the instrument.

A more detailed description of the spectrograph and its main components can be found in the UVES User Manual and in Dekker et al. (Proceedings of the SPIE Conference 4008, Munich, 2000).

Who is Who in the UVES Project?

The table includes the names of the engineers, technicians and astronomers who have contributed to the design, building and testing of the various subsystems and of the instrument in the last seven years. This serves as recognition of a job well done and also as a reminder of the different expertises that are needed to complete and put successfully into operation a complex instrument at the VLT. Starting from the optical designer to the astronomers who verify the quality of the first astronomical data, from the skilled technicians who integrate and test the optomechanical functions to the software specialists who wrote more than 140,000 lines of code for instrument control, all had to complete their task properly and in schedule for the instrument to be successful. A total of approximately 40 person-years and 6.7 MDM went into project.

UVES through Commissioning

Hardware and software were first put together, tested and optimised in the ESO Integration Laboratory in Garching. The results in the laboratory confirmed the quality of the optics, the capability to reach the specified resolving power, and the robust, reliable behaviour of the electro-mechanics and of the software. The tests were completed in May 1999, the instrument was then fully dismantled, its hundreds of components properly packed and sent part by plane, part by ship to Chile. At

TABLE 1. THE UVES TEAM

Project Manager, Optical Engineering:	H. Dekker
Instrument Scientist:	S. D'Odorico
Optical Design:	B. Delabre
Mechanical Engineering and Design:	H. Kotzlowski, G. Hess
Control Electronics:	S. Moureau
Control Software:	A. Longinotti, P. Santin and P. Dimarcantonio (Obs. Trieste), R. Schmutzer
CCD Detector Integration and Testing:	R. Dorn, C. Cumani
Opto-mechanical Integration and Testing, Cryogenics:	J.L. Lizon à l'Allemand, C. Dupuy, A. Silber
Data Flow System (Pipeline, Instrument Model and ETC, P2PP):	P. Ballester, O. Boitquin, M. Chavan, A. Modigliani, S. Wolf
Testing in Europe, Commissioning, Calibration and Operation at Paranal:	A. Kaufer
Astronomical Support, Documentation, Data Reduction, Testing of Pipeline:	S. Cristiani, V. Hill, L. Kaper, T. Kim, F. Primas
(All from ESO, except where indicated differently)	



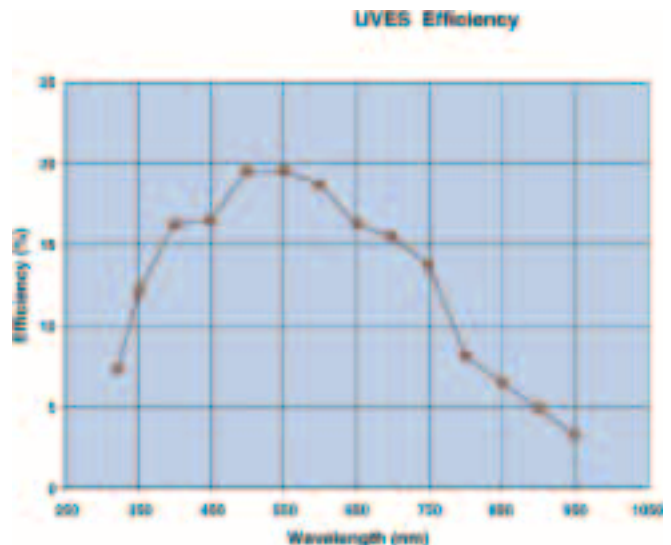
Figure 3: After the successful first light, part of the UVES team proudly poses close to the instrument with its partially lifted enclosure. From the left, back: A. Kaufer, C. Dupuy; front: A. Longinotti, P. Santin, P. Dimarcantonio, H. Dekker, S. Moureau and R. Schmutzer. The almost total compliance with the Observatory safety regulations, even at a time of undisputed euphoria, is worth praise.

the Observatory, first the table was installed on the Nasmyth platform of UT2, the Kueyen Telescope, and then the complex layout of optics, mechanics, cables, detectors was reassembled and the optical path re-aligned (Fig. 2). We went through this usually critical phase (it is the time one discovers whether proper care has been taken of the interfaces with the telescope) with a minimum of bad surprises: a few holes were not in the right places, the table plane a few millimetres below the expected height. The optics, and especially the large lenses of the cameras had survived the loading from the plane and the bumpy road from Antofagasta to Paranal but the blue camera did show a degraded optical quality and had to be dismounted and re-aligned. In the last week of September, we were finally ready and eager to verify whether the operation of UVES at the telescope and its overall efficiency on the sky were in line with the model prediction. A crucial point to check was the acquisition and guiding of the targets on the slit plane and the parallel operation of the two arms in the dichroic modes.

The first stellar photons entered the spectrograph on September 26. Jason Spyromilio and Anders Wallander had just concluded the commissioning on the Kueyen telescope with the Test Camera reporting record performance in image quality and tracking performance. We had already gone through extensive testing and optimisation with the calibration lamps and knew that the instrument's optical quality was basically all right. The first target was a flux standard star. From the very beginning we were ready to carry out target ac-

quisition, instrument setting, observations and archiving of the data starting from Observation Blocks prepared in advance with the instrument templates. We launched the first OB and the star landed within one arcsecond from both slits and was centred without problems (except the mandatory wrong sign in one of the formula to convert pixels to coordinates) using the slit viewers. On the same night, a quick analysis of the spectra produced an overall efficiency that is very close to the predicted values at all wavelengths but in the far-red region. The following night, on September 27 (the official first light) was blessed by a seeing between 0.6 and 0.4 for 90% of the time and we could

Figure 4: The overall efficiency of UVES derived from observations of the standard stars EG21 and Fei 110 taken with a wide open slit. The values refer to the top of the blaze function in each order and have been obtained from observations with two dichroic standard settings. They are corrected for losses in the atmosphere and in the three-mirror reflections of the telescope. The decrease of efficiency toward the UV and the far-infrared are mostly due to the lower efficiency of the CCDs and of the cross-disperser gratings at these wavelengths. Both components could be easily substituted with new ones of higher performance, when they become available.



confirm the capability of UVES on the first scientific targets (see the ESO 15/99 press release on the ESO Web pages). At that point, we knew that with UVES+Kueyen, we had on line the most powerful combination for high-resolution spectroscopy available to the astronomical community worldwide. It was, and still is, a nice feeling which helped us to go through the subsequent less exciting but necessary three weeks of testing and calibration of all the instrument modes, of the acquisition procedures and of the software interfaces.

The smoothness of the commissioning of UVES is best testified by the very low number of hours lost due to technical problems of the telescope or instrument: around 7 in total over three weeks of continuous operation, of which three were due to the sudden death of the power supplier of the instrument WS, three to a failure of the telescope M2 unit, due to a gust of wind well above the safe operation conditions and one to a rebooting of the instrument control software.

A substantial chunk of data of scientific value taken for Commissioning has been released with their calibration for public use. They correspond to more than 94 hours of integration on the sky.

A second, shorter commissioning period in December was mainly dedicated to the optimisation of the blue arm optical alignment, to the test of the iodine cell and the final editing of the instrument observing templates.

The performance of the instrument at the time of the handing-over to the Observatory in December 1999 is summarised in Table 2. An additional important parameter is the stability of the wavelength calibration. When allowance is made for the variation of the refractive index of air with temperature and pressure (both recorded in the file headers), the velocity stability of the

Central wavelength: 580.0 nm, slit: 0.5 arcsec, CCD: EEV, 11.9 °C
 Filename : UVES_RED_CAL349.19.fits, Observ. date: 1999-12-15T21:08:08
 Median(DX) = 2.854 pix , Mean(DX) = 3.0 pix , σ (DX) = 0.8 pix
 Median(RES) = 82620.641 , Mean(RES) = 80800.0 , σ (RES) = 8036.0

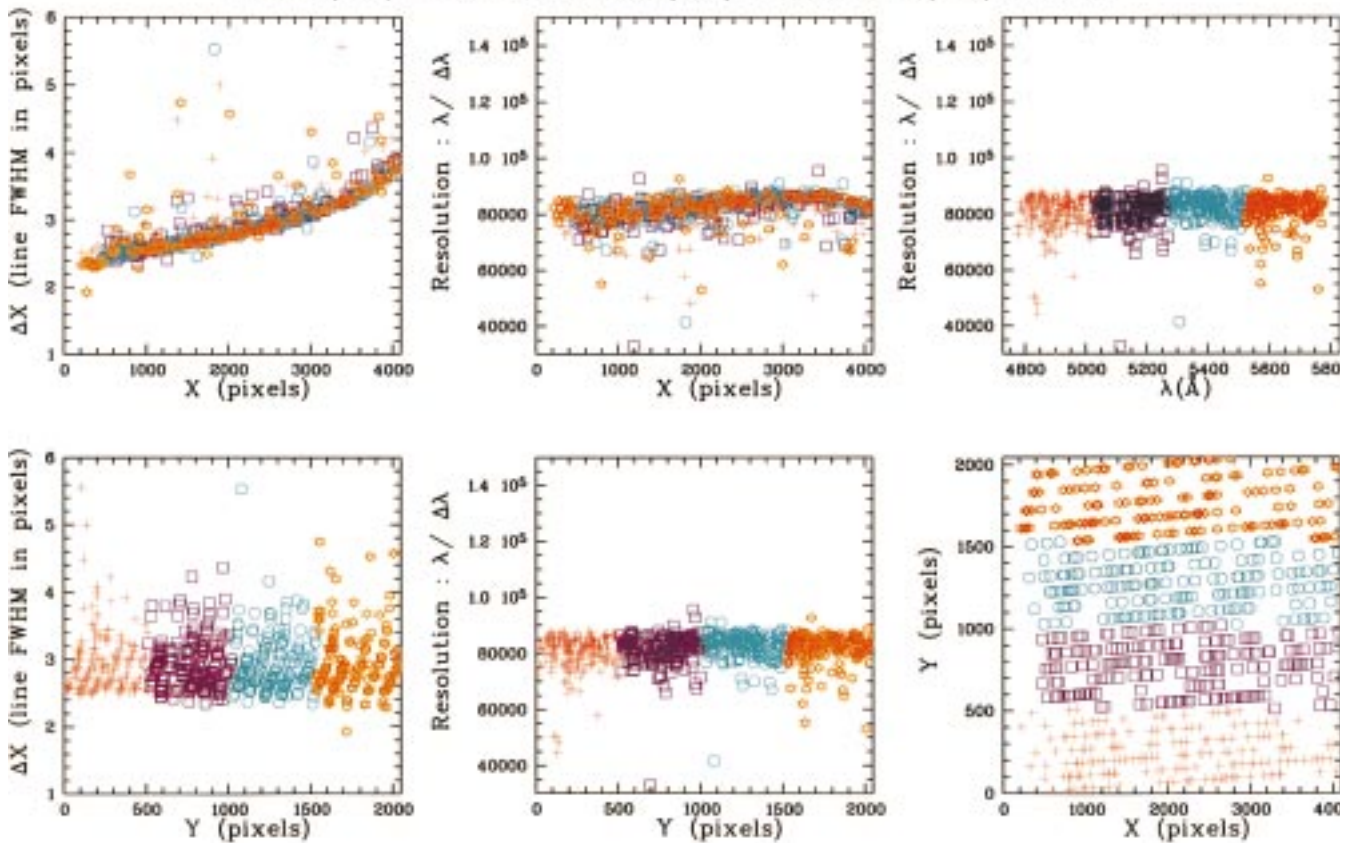


Figure 5: This plot, a by-product of the automatic data-reduction pipeline running for the instrument standard wavelength settings, maps the instrument resolution from measurements of the FWHM widths of the lines of the ThA lamp distributed over the whole CCD (see subplot bottom-right). Resolution and FWHM in pixels for each line are given as a function of position on the chip and wavelength. This particular diagram refers to a spectrum obtained with a 0.5-arcsec-wide slit and to the region covered by the EEV CCD-44 chip in the red arm.

instrument over days was found to be of the order of 50 m/s. The use of the iodine cell, not yet tested in full, should further lower this limit to a few meters/sec but it requires an effort by a

specialised team on the data-reduction software.

While the overall status of the instrument at the end of Commissioning is very satisfactory, there are a few pend-

ing problems on which we need to work. The tracking of targets observed with the image slicers was found to require an unplanned modification of the TCS. The Cross-Dispersers #1 and #4

TABLE 2. UVES OBSERVING CAPABILITIES AND MEASURED PERFORMANCE

	Blue Arm	Red Arm
Wavelength range	300 –500 nm	420 –1100 nm
Echelle	41.59 g/mm, R4 2 mosaicked replicas on a Zerodur block	31.6 g/mm, R4 2 mosaicked replicas on a Zerodur block
Cross-dispersers	CD1: 1000 g/mm, λ_b 430 nm CD2: 660 g/mm, λ_b 460 nm	CD3: 600 g/mm, λ_b 560 nm CD4: 312 g/mm, λ_b 770 nm
CCD format and pixel scale ⊥ disp (1 pixel = 15 μ m)	2048 × 4096, windowed to 2k × 3k (.25"/pix)	4096 × 4096, 2 × 1 mosaic (.18"/pix)
Resolution-slit product/wavelength bin	41400 0.0019 nm at 450 nm	38700 0.0025 nm at 600 nm
Max. resolution	80,000 (0.4" slit or IS)	115,000 (0.3" slit or IS)
Throughput (TEL+UVES, no slit, no atmosphere)	10 % at 400 nm	12% at 600 nm
Limiting magnitude (90m. exp., S/N =10, 0.7" slit & seeing)	18 (R = 58,000) at 360 nm	19.2 (R = 62,000) at 600 nm
$\lambda\lambda$ /frame, CD1, CD3 CD2, CD4	85 nm in 33 orders 126 nm in 31 orders	200 nm in 37 orders 403nm in 33 orders
Order separation (minimum)	10" ↔ 40 pixels	12" ↔ 70 pixels

are not the ones ordered for the instrument but prototypes of inferior quality. This results in a lower efficiency especially in the far red and in stronger optical ghosts in the UV and far red (in the most unfavourable configurations up to a few per cent of the primary spectrum). The final gratings should be installed by the end of this year.

In February 2000, UVES was used in service mode for nine nights of Science Verification on a variety of scientific programmes (see for details <http://www.eso.org/science/ut2sv>).

Everything went smoothly and the weather co-operated: a total of more than 70 hours of integration mostly in excellent seeing conditions were suc-

cessfully completed. The data will be released to the community in late spring.

Acknowledgements

The UVES project team gratefully acknowledges the steady support of many ESO staff, in particular C. Nieuwenkamp and G. Wieland (Contracts and Procurement) and E. Zuffanelli (INS) in Garching and of the Paranal staff P. Gray, G. Gillet, G. Rahmer and P. Sangsasset during the instrument integration. Special thanks are due to J. Spyromilio who was there to help, advise and support when requested, throughout the entire commissioning.

In the framework of a long-standing collaboration with ESO, the Observatory of Trieste provided a substantial, highly professional contribution to the project with the work of P. Santin and P. Dimarcantonio on the instrument control, observing and maintenance software.

We are particularly grateful to the members of the UVES Science Team B. Gustafsson (Uppsala Observatory), H. Hensberge (R.O.B., Brussels), P. Molaro (Osservatorio di Trieste) and P.E. Nissen (Aarhus University) for their advice and the support to the project throughout its development.

E-mail: sdodoric@eso.org

VLT Pipeline Operation and Quality Control: FORS1 and ISAAC

R. HANUSCHIK and P. AMICO

Quality Control, ESO

1. Introduction

It is well known in the community that April 1, 1999, marked the beginning of operations for ANTU, the first VLT telescope. It is less well known, however, that this date also marked the beginning of real life for VLT data-flow operations (DFO) at ESO Headquarters in Garching. Forming the back end of the Data-Flow life cycle, DFO has to act as data-production, data-distribution and data-storage machine. All these functions form what is called Quality Control (QC). For achieving data products of the highest possible quality, all components have to perform well and collaborate closely.

At the moment of writing this, two VLT instruments are operational: FORS1 and ISAAC, with the next two waiting at the front door (FORS2 and UVES). We will briefly describe in the following the different QC tasks for the two first VLT instruments.

2. General Functions

The most important tasks for QC Garching are:

- commission the instrument data-reduction pipeline,
- create master calibration data and calibration solutions,
- reduce science data,
- sort and distribute all kinds of data (raw, reduced, calibration, logs, listings) for the Service Mode package,
- check the quality of processed data,
- provide instrument health checks,
- perform trend analysis of quality parameters.

Present ESO strategy for processing and distributing data is as follows: calibration data are processed irrespective of the observing mode (both Visitor and Service Mode), science data are processed for Service Mode (SM) observing only. SM programmes (of supported instrument modes) receive a full set of raw, reduced and calibration data. Processed calibration data will become generally available as soon as the Archive storage project has been realised.

Hence a Visitor Mode (VM) night, from the QC point of view, requires only processing of calibration data, while a SM night needs the full machinery producing master calibration and reduced science files. For a typical 50:50 mix of SM/VM nights and an average QC fish¹ with 4-days-per-week duty, there is presently about one QC working day per ANTU operational night available. Any time more than that will produce a backlog.

3. FORS1

Data. Being a complex instrument with many different modes, FORS1 produces data from the very beginning of operations in a huge amount and variety. Period 63 produced about 24,000 raw FORS1 files – about 200 GB – , about half of them in Service Mode. 68.0% of all raw files were calibration data, 17.9% science data, the rest

(12.7%) TEST data (acquisition, slit view, etc.). The vast majority of all FORS1 files (70.9%) was obtained in imaging mode (IMG), the second largest fraction (18.4%) in multi-object spectroscopy mode (MOS), 5.2% in long-slit spectroscopy (LSS), 3.9% in polarisation imaging (IPOL) or polarisation MOS (PMOS). Typically 100–200 files are produced per SM night which correspond to 1–1.5 GB of raw data resulting in another 1–1.5 GB of reduced data.

Pipeline operations. Due to the complexity of the task, we decided to start pipeline operations with the simplest modes, IMG and LSS. These together cover already 76% of all FORS1 data. Master calibration files routinely created are:

- Master BIAS files for all 4 CCD modes (high and low gain; 1-port and 4-port readout).
- Master flats for IMG mode: master SCREEN_FLAT_IMG, master SKY_FLAT, master NIGHT_FLAT. They come in two CCD modes (high and low gain, 4-port readout). Master SKY_FLATs are used for science reduction (see below) and hence are measured in all filters available for imaging, the most commonly used are the Bessell UBVR_I filters. They are frequently measured in dusk and dawn.
- Tables with photometric zeropoints (ALIGNED_PHOTOMETRY_TABLE) from standard star frames for IMG mode: these are exposed in the five standard Bessell filters (UBVR_I), usually in the high-gain, 4-port CCD mode. Sets of such five stan-

¹Since this process bears some resemblance to trout held in purification plant basins to indicate water quality, we have dubbed ourselves the 'QC fishes'.

ANTU/FORS1 trend analysis: BIAS

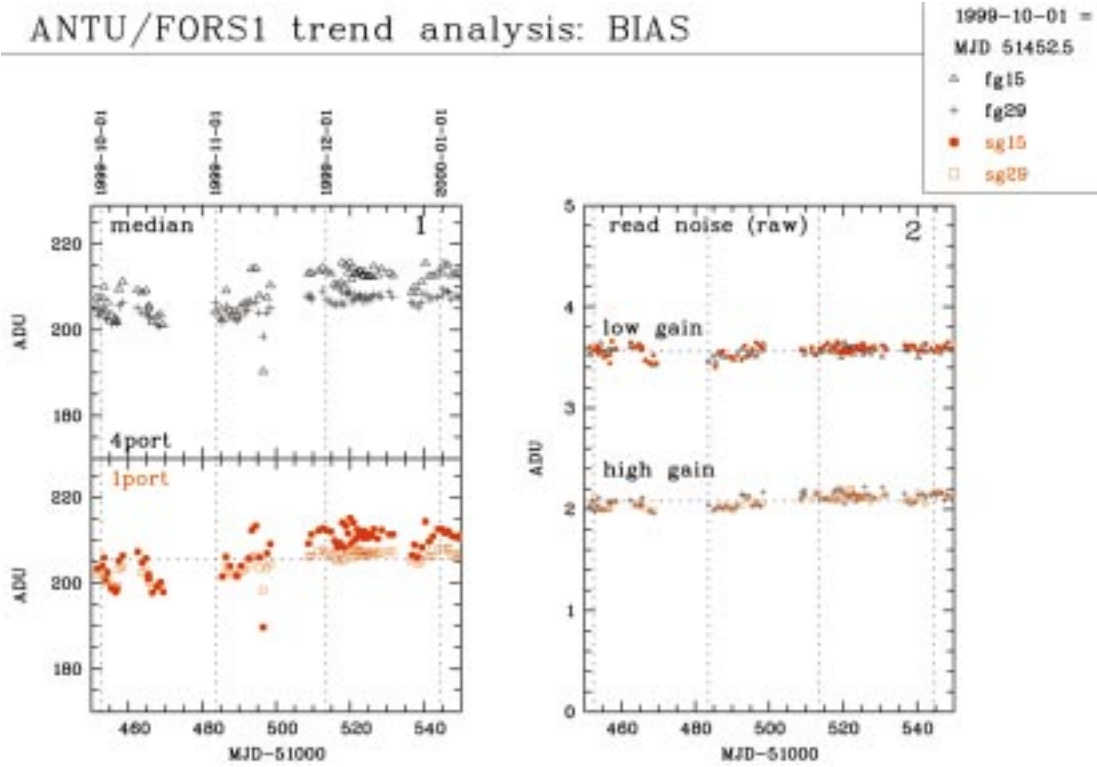


Figure 1: FORS1 trend plot of the BIAS QC parameters median value (diagram 1) and read noise (diagram 2) for the four CCD modes low and high gain / 1-port and 4-port readout. The period covered is 1999-10-01 to 2000-01-01. These plots are used to assess the stability of the CCD system and identify outliers.

ANTU/FORS1 trend analysis: SCREEN_FLAT_IMG

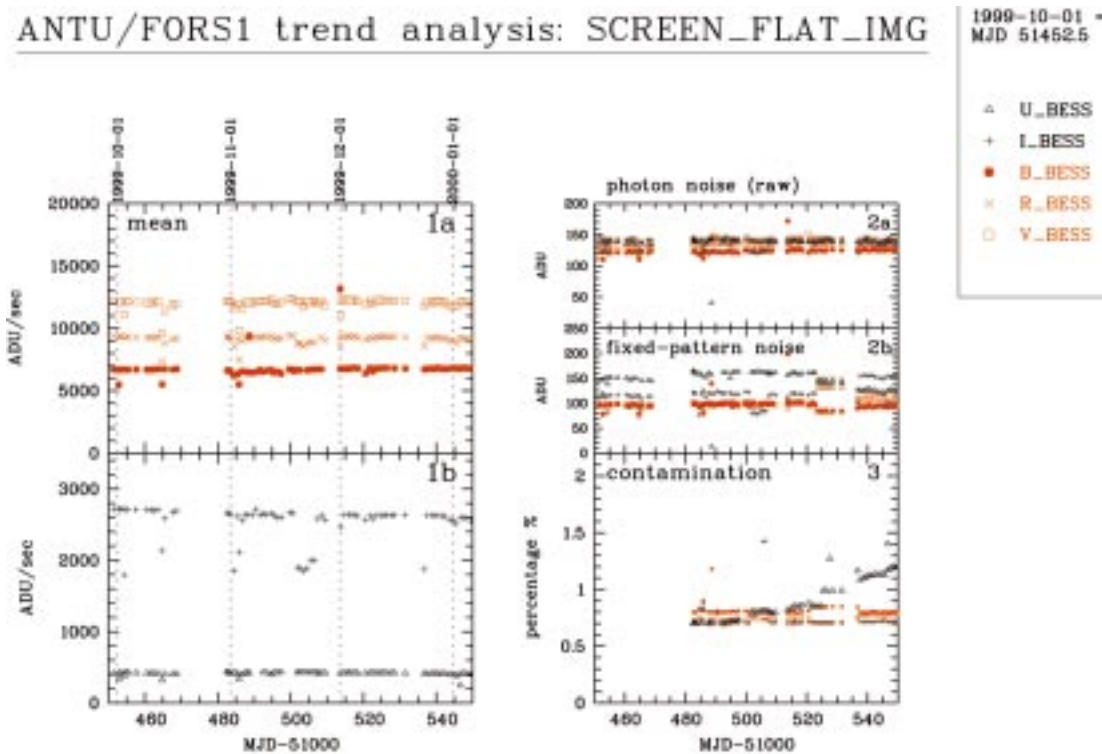


Figure 2: Trend plot for QC parameters of SCR_FLAT_IMG calibration files. Diagram 1 shows mean values, diagram 2 photon noise (in raw frames) and fixed-pattern noise, diagram 3 large-scale structure (both in master files). Data are for the five Bessell UBVRI filters. The last plot clearly shows the CCD contamination slowly increasing with time, mainly affecting the U filter.

ard exposures are taken at least once, usually several times per night.

- Master flats SCREEN_FLAT_LSS and dispersion solutions WAVE_DISPERSION_LSS for LSS mode.

These come in 6 grisms which could be combined with any of 9 longslits.

Hence for a typical IMG mode night about 30–40 master calibration files have to be created by the pipeline.

pattern is very different from sky conditions. They are primarily used for monitoring the CCD performance.

Photometric standard stars are reduced the same way as science data, with the added step of source identifi-

Master files are median averages from input sets of typically 3–5 raw files. The master creation recipe uses a kappa-sigma clipping routine to reduce random noise, suppress cosmics and stellar sources.

Science data are reduced using these calibration products. SCIENCE_IMG files are debiased and flattened. The pipeline uses twilight SKY_FLATs taken in dusk or dawn. These flats remove all small-scale CCD structure ('fixed-pattern noise'), the four-port pattern and all large scales except for the largest ones of order 1000 pixels. This is due to illumination gradients differing between night and twilight, and amounts to 1–2%. A NIGHT_FLAT would remove even this gradient perfectly, but is not routinely available. If possible, the pipeline extracts such flats from jittered science images. Success depends on the offset chosen for jittering, the nature of the sources and their density. If available, these NIGHT_FLATs are delivered as part of the SM data package, but they are not used for pipeline science reductions. Master SCREEN_FLATs are available, but their illumination

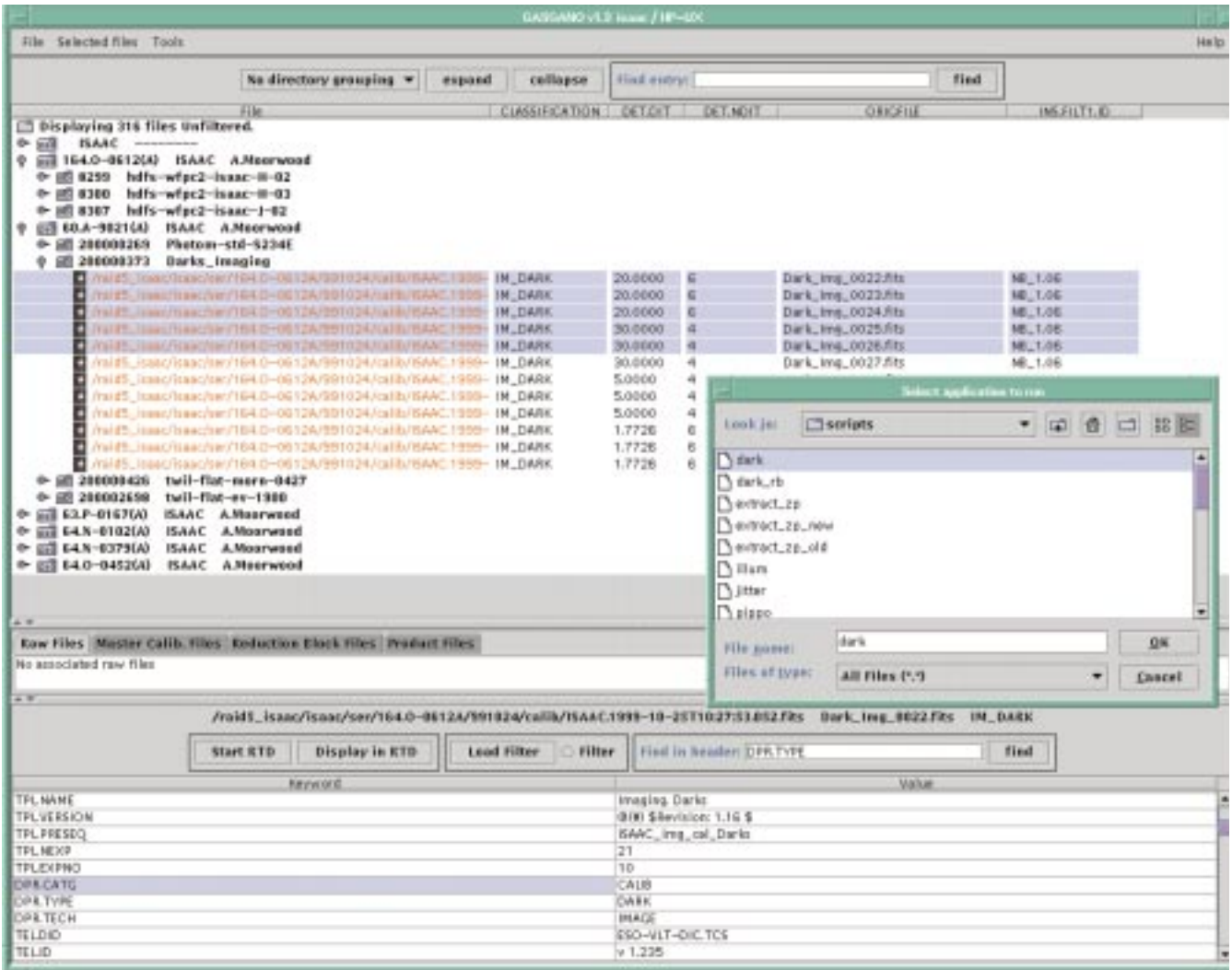


Figure 3: Snapshot of the Gasgano GUI in use with ISAAC data. The tool allows interactive selection of classified frames and their input to the corresponding pipeline recipes.

cation and extraction. At the moment, they produce photometric solutions (zero points) for the night. Currently this information is used to assess the quality of the night and trace telescope efficiency. SM data packages receive the zeropoint tables and the reduced standard star files.

LSS data are de-biased and flattened using master SCREEN_FLAT_LSS files which contain high spatial frequencies only. The data are rebinned to wavelength space but not extracted. Hence fixed-pattern noise, slit noise and slit function are removed, as is slit curvature.

Planned next steps are the photometric calibration of the IMG files, and removing of the instrumental efficiency curve for LSS data. Finally the MOS pipeline will become operational in Period 65.

A total of about 3000 master calibration files, and about the same number of reduced science files, has been created in Period 63. 93% of these files are IMG files.

Distribution. The proper distribution of files in the Service Mode packages is not trivial, if calibration files are concerned. As the simplest example, look

at science files taken in IMG mode and assume that the OB was taken with just one filter and in one CCD mode. This would make a minimum set of one master BIAS and one master SKY_FLAT taken with these parameters (plus, of course, the corresponding raw and reduced science files). Since it is not known, however, whether the programme requires photometry data, we always add all available STD_IMG files (raw, reduced, photometry table). To further enable the PI to reprocess all reduction steps, this requires all applicable SKY_FLATs and BIASses as well. Hence we actually blow up the amount of data delivered by a factor which can go up to 5 or more, but only this approach guarantees completeness. To slim down the CD-ROM package a little bit, we usually do not include those raw calibration files that successfully produced master files. These raw calibration files can be retrieved by the user from the ESO Archive (see article by Leibundgut et al. in this issue).

For the LSS mode, things become more complicated since spectrophotometric standard stars are taken in MOS mode. Hence LSS programmes receive full sets of LSS and MOS calibration

files, and the blow-up factor is even larger than for IMG files.

Quality Control. Post-pipeline operations involve quality checks of the raw and the produced data. As a simple but time-consuming check, scanning the night logs is fundamental. This is presently done in the old-fashioned way, i.e. reading and, if needed, editing by hand. In the near future there will be tools to have night-log information accessible for automatic processing, distribution and storage.

On raw and produced calibration data, several checks are done. From the BIAS frames, median values for the bias level (both across the whole CCD and per port), for the value of large-scale structure, and for the read noise for raw and master files are determined (Fig. 1). On the SCREEN_FLATs and the SKY_FLATs, the mean values (across the whole CCD and per port), the random photon noise, the fixed-pattern noise, and the large-scale structure are measured (Fig. 2). SCREEN_FLATs are also used to measure actual gain values. It is checked how random the 'random' noise is.

Photometric zeropoints are determined. The quality of the LSS disper-

Table 1: List of templates supported by the ISAAC pipeline recipe set. The recipe's products are made available to the user community during the indicated observing period. The description briefly explains what the recipe does. For more detailed explanations, please refer to the ISAAC web page and references therein (<http://www.eso.org/instruments/isaac/>).

Supported imaging templates	Period	Description
Jitter	63	It reduces images taken in jitter and jitter + offset modes. The jitter data reduction process is divided into flat-fielding/dark subtraction/bad pixel correction, sky estimation and subtraction, frame offset detection, frame re-centring, frame stacking to a single frame, and optional post-processing tasks.
Jitter+Offset	64	
Darks (including spectroscopy)	63	Creation of master dark frame. The process sorts out frames with an identical DIT and produces the averaged frames. It computes also the read-out noise.
Zero-points	64	Calculation of zero points. It computes the number of counts, and relates that measurement to a standard star database. The identified infrared star database at present contains about 800 star positions with magnitudes in bands J, H, K, K _s , L and M.
Twilight flats	63	Creation of master flat frames. It takes as input a list of files taken at twilight and produces the flat-field of the detector by observing this rapidly increasing or decreasing signal. Since it computes a characteristic curve per pixel, it also creates a bad pixels map.
Illumination frame	64	Creation of master illumination frames. It subtracts dark, divides by flat-field and corrects bad pixels if the adequate calibration files are available. The final product is a 2d polynomial surface normalised to a value of 1.
Supported spectroscopy templates	Period	Description
NodOnSlit	64 (partly)	It reduces images taken in jitter spectroscopic mode. The process is divided into the classification of the input files, correction of the distortion, shifting the frames and averaging, wavelength calibration, creation of a combined image, detection and extraction of a spectrum. The wavelength-calibrated spectrum is provided for all calibration standard star observed in this mode. It is not provided for science frames.
Spectroscopic flatfield	64	Creation of master spectroscopic flat frames. This algorithm is applied to each pair of frames (lamp on and off). The difference 'on'-'off' is computed and the result frame is divided by its mean.
Arcs	65	It detects vertical or horizontal arcs in a spectral image, models the corresponding deformation (in the x or y direction only) and corrects the found deformation along the x or y direction. Finally, it computes a wavelength calibration using a lamp spectrum catalogue.
Star trace	65	It performs star-trace analysis. It takes as input an image and produces two tables of output: a line position table (containing the fitted coordinates of the curved lines) and a polynomial coefficient table (describing the found deformation).
Slit position	65	It finds the exact position of a slit.
Response function	65	Determination of the spectroscopic response function, by means of the extraction and wavelength calibration of a standard star spectrum.

sion solutions and the effective resolution are measured.

All these parameters are stored in tables and their trends monitored. There are also checks whether random noise and fixed noise scale with signal as expected.

In reduced science IMG files, the quality of the flattening process is controlled.

Feedback. Since part of the results of the QC process is a direct health check for the CCD and the instrument, a natural task for QC Garching is providing feedback to the CCD group and to Paranal Science Operations. This is mostly channelled through the Instrument Operation Teams which

combine expertise about the instrument.

Generally, it is important to store and provide QC results in a centralised way open to anyone interested. Options are putting results onto the web, have quality-control parameters stored in a QC database, and ingest QC information into the Archive. As a first step, check the newly created QC page to be found under http://www.eso.org/observing/dfo/quality/index_fors1.htm.

Software for operations. For FORS1 and ISAAC, software for the lower-level functions existed when operations started, provided by ESO or by the instrument consortia: the data reduction pipeline and tools for or-

ganising the data and processing them.

All higher-level tasks, such as distributing raw and product files to the final SM data packages, pre-selecting data for processing, assessment of data quality, storage of QC parameters, etc. started during Period 63 without software support. Tools had to be developed during operations. Such 'hot development' offers the advantage of being extremely efficient since any new script could be tested and improved under real life conditions. Evolutionary cycles were short. However, the price to pay was a very tough schedule since certain elementary tasks had to be provided, no matter whether tools existed or not.

It soon became clear that there is only one option for keeping one's head above water: create (UNIX shell) scripts and (MIDAS) procedures for automatic processing. The strategy to survive is: clearly identify the jobs which can be routinely done and those which can't. Then leave the routine stuff to the machine preferably for overnight processing, and do the non-routine work during daytime. This primarily involves decision making, i.e. quality assessment of master calibration and reduced files, commissioning of pipeline recipes, and keeping control of the whole process.

The backbone of the FORS1 QC job is formed by about 30 shell scripts which translate the basic steps of data-flow operations into well-defined functionalities. This package is called 'SMORS' (Service Mode Optimised Reduction Scheme). It produces results which are repeatable and predictable, and its operation is safe. With this package, we do the full data processing from the very beginning (provide listings for newly arrived raw data) up to the end of the life cycle (delete all data for an SM programme once the CD-ROMs have been distributed).

SMORS being the backbone, a second package is the 'brain' of FORS1 quality control: 'qc_dec' (QC decision), a number of MIDAS procedures developed for post-pipeline assessment of data quality, measuring QC parameters and trending. These tools enable decision making, e.g. accept or reject a master calibration file, measure the fixed-pattern noise in a master_screen_flat, check the removal of stellar sources in a master_night_flat, check the degree to which a SCIENCE_IMG file has been flattened, create nightly averages for photometric zeropoints.

As a by-product of the tools developed for pipeline operations, a script package 'Pipe' has recently been installed on Paranal to facilitate the operation of the FORS1 quick-look pipeline. This tool can be used by staff astronomers to create their own master calibration files and obtain photometric zeropoints during the night, so that real-time assessment of the quality of the night becomes possible.

4. ISAAC

Quality-control operations for ISAAC resemble in broad sense those described in the previous section for FORS1. The differences between the two instruments, especially in terms of operations, lead to a different approach from a QC point of view.

P63 statistics. During Period 63 there have been 92 nights with ISAAC data (science and calibration frames) and a total of 59 service mode nights (with science data), which have produced a total of 24087 files (including commissioning and science verification data), divided into 13349 science

frames, 9985 calibration frames and 753 test frames. The total number of SM programmes was 35, 4 of which required quick releases (that is, release of the data soon, typically 1 day, after observations). At the end of the Period, 29 programmes had been shipped to the users, while the remaining 6 were put on hold by User Support Group (USG) and Science Operations in Paranal (PSO) to allow for follow up observations during Period 64. A total of 69 CDs were prepared and cut, the biggest programme received 12 CDs, the smallest only 1. The longest programme spanned 5 months and the densest was observed in 12 different nights.

CD packing. Each PI of a SM programme receives a set of CDs containing data subdivided by night of observation. Each "night" contains the following data:

- Science raw frames and programme specific calibration files (if required by the observer).
- Calibration raw frames taken following the calibration plan (only those pertaining the specific settings required for the science raw frames). For example, a programme that required observations in short wavelength mode (SWI1) in K_s band with a single value of the detector integration time (DIT) will receive the twilight flats in K_s , the standard star frames for that night in all bands and the dark frames for all the DITs used (science plus calibration frames).
- Master calibration data – the master files as created by the ISAAC pipeline recipes set. For the above example, the user will receive the master dark frames for all DITs and the master twilight frame in K_s .
- Reduced science frames – all science frames sets observed using the autojitter and autojitter + offset templates are sky-subtracted and coadded.

During Period 63 the pipeline produced a total of 268 master calibration frames (SWI1 mode only, master flats and darks) and 55 coadded images (in jitter mode). The average number of frames used to produce a single master frame was 18 for calibration and 17 for science frames.

In addition to the data, for each night of observation and each set of data (raw science and calibration, reduced science and calibration) a table with the list of files and their most relevant keywords (e.g. RA, DEC, DIT, filters, central wavelength, etc.) is included. Each CD contains the night logs for the relevant night of observations with all pertinent log entries written during observation by the operation staff astronomers in Paranal, and a data reduction log, which contains information on the data package, the reduced frames, the OB list, etc.

The packing process for a specific programme starts upon receipt of a "completion" signal from USG and finishes when the package is sent to the PI. In the worst case in Period 63, the delivery time had been 40 days after the signal while in the best case less than 1 day. It has to be noted that the delivery time decreased steadily during the Period, and now, for Period 64, the average is 1 day after receiving the completion signal.

When operations for ISAAC started in April 1999, it was decided to concentrate on SWI1 mode only and to progressively increase the number of products delivered to the users. This choice was driven mainly by the specific need of further testing for the recipe set in short wavelength spectroscopic modes (SWI1 and SWI2) and by the more general fact that, running operations for the first time ever, was a task full of unknowns. Now that the whole data-flow process is better understood, we progressively add tasks to quality control and services for the user community.

ISAAC Pipeline Recipes. Each VLT instrument has its own pipeline set of recipes, which support all or part of the instrument modes. In the case of ISAAC, presently the pipeline supports the short wavelength modes, imaging and spectroscopy and will probably be extended in the future to include the long wavelength modes. In Period 63, the ISAAC pipeline set of recipes was into SWI recipes, all developed as part of the Eclipse software (N. Devillard, "The eclipse software", *The Messenger* No. 87 – March 1997 and <http://www.eso.org/projects/aot/eclipse/>), and SWS recipes, developed in MIDAS by Y. Jung. As for Period 64, and starting with operations in Period 65, all SWS recipes have been also included in the Eclipse software, thanks to the work of Y. Jung and T. Rogon. Table 1 lists the entire set of templates supported by the pipeline.

Among the responsibilities of QC, testing of the pipeline recipes is one of the most important, since the work of QC relies entirely upon this set of recipes for the great part of the work. The quality control scientist produces master calibration frames and certifies their quality before shipment to the users. In the near future all frames will be inserted in the calibration database and made available to the user community. As for Period 64/65 the following by-products of the pipeline are calculated and their trending monitored: read-noise of the detector, zero points for each night. Zero point values are also made available to the users with SM programmes. Shortly, they will be published on the Web for the entire user community. In addition, the goodness of sky-subtraction and coaddition, as well as image quality is monitored in all coadded images produced for SM

programmes. Further checks will be introduced for all products produced by the pipeline (e.g. spectroscopic jitter mode images).

For additional information on the supported templates and operating modes see the ISAAC home page online and the ISAAC manual (<http://www.eso.org/instruments/isaac/> and references therein) and the PSO web pages for ISAAC (http://www.eso.org/paranal/sciops/ISAAC_Info.html).

Software for Operations. When operation started in April 1999, we had clearly understood the general picture of the data-flow, but we missed first-hand experience on the actual amount and the type of work, on the most efficient way to do it and of course on all those unknowns, which are to be expected every time a new enterprise is started.

To perform the first 4 tasks listed in section 2, QC could from the beginning make use of the data-flow system, which includes, among the others, the Data Organiser (DO), a software which classifies the raw data and creates reduction blocks, which are in turn used by the Reduction Block Scheduler (RBS) software to fire the proper recipe and run it for the list of raw frames previously classified. Both DO and RBS work in a completely automated way. For the particular case of ISAAC, the different science operations needs, which change according to the particular observing programme to be executed, and the wish to keep them as flexible and efficient as possible, require a greater level of “human” interaction than what allowed by automated software. In the majority of cases, it is necessary to classify the files, to select the frame-set as input to a data reduction recipe and to tailor the configuration parameters of the recipe itself manually. Given the great amount of data that reaches Quality Control and that has to be processed and distributed, a new software tool had to be foreseen. The main requirements for it were: flexibility and interactivity of operations, compatibility with the data-flow model and with the needs of QC work, speed (in a typical ISAAC night a minimum of 300 files can be produced and in a typical QC working session many nights of data must be loaded, classified and reduced at the same time) and configurability. The Software Engineering Group (SEG), namely N. Kornweibel and M. Zamparelli, developed a software named Gasgano (see Fig. 3), which provides these and many other functionalities, which make it the tool routinely used by QC for ISAAC. The tool has been recently officially released to PSO, but has been tested and used by QC since its very first “unofficial” release.

Since the creation of a CD package for a SM programme is not yet feasible by means of Gasgano, a set of UNIX

shell scripts, similar to those created for FORS1, was developed for ISAAC. These scripts allow to quickly and (semi) automatically assemble all science and calibration raw data, their corresponding reduced frames and the reduction logs; in addition the scripts produce a reduction and packing log, file listings, useful statistics (number of frames divided by type – science or calibration –, Programme ID and OB ID and list of rejected frames, typically files with incorrect or missing keywords) and check logs. The latter are compared with information retrieved by the scripts themselves from various database tables of the ESO archive (OB repository, Observations, etc.). The difficulty of the packing process lies almost entirely in the non-uniform distribution in time of the calibration files and in the vastness of the science data parameter space: the script must be able to “intelligently” choose a proper set of calibration frames, observed as a rule under a different program id and in general in different days than those of science frames. Those may also vary, for different SM programmes and within a single programme, in all possible modes allowed by the instrument.

We have already started to develop an extra set of scripts/tools to check the quality of processed data, up to now performed manually on each frame, to provide instrument performances checks and to perform trend analysis of quality parameters. It is foreseen that they will be fully ready to support QC operations within Period 65.

5. Instrument Operations Teams

From the user point of view, Quality Control activities represent the last element of the data flow life-cycle chain, in the sense that the final delivery of the data, which ends the cycle, relies upon it. Less evident for outside observers is that the entire operation process reckons upon the work of a fairly large group of persons with different responsibilities within the chain and owes its success to the interactions that occur among them. This group forms the so-

called Instrument Operations Team (IOT) and every instrument for the VLT has a similar team assigned to it to ensure operations.

6. Lessons Learnt

After more than one period of operation, it is clear that the basic concepts of Quality Control are routinely working. Data are processed and their quality checked, PIs receive their SM data packages. These data packages add value to the simple traditional raw file collections.

Some important issues could be identified during operations. One is: keep the instruments simple, if you want to have simple operations. There is a close correlation between, e.g., the many modes offered by FORS1 and the complexity of its data flow operations.

Operationally, do as much as possible in automatic mode. This is reliable, reproducible, and can be done in batch mode. Scripts are preferable over interactive tools if you go for mass production. The evolutionary development approach, though dictated by circumstances, proved to be efficient.

Data integrity is very important. We cannot afford to manually correct errors introduced upstream: either files arriving in Garching are syntactically (DICB conform) and logically integral (e.g. have proper programme and OB ID), or they are useless. DICB conformity is also extremely important for Archive integrity. Data with wrong keyword contents will never be properly retrieved. They are just wasting disk space.

Relevant information has to be kept central. Facilities like web pages, relational databases and the Archive are crucial.

All in all, the tasks of QC Garching combine astronomical challenges with information technology challenges. They close the loop for VLT data production, provide added value to the community and create a sound database for assessment of instrument performance.

rhanusch@eso.org, pamico@eso.org

Table 2: Members and their respective roles within the team for ISAAC and FORS1.

Role	ISAAC	FORS1
Instrument Scientist	Jean-Gabriel Cuby	Gero Rupprecht
Operations Staff Astronomers	Chris Lidman, Gianni Marconi	Hermann Boehnhardt, Thomas Szeifert
User Support Astronomer	Almudena Prieto, Fernando Comerón	Palle Møller
Pipeline Development	Nicolas Devillard, Yves Jung, Thomas Rogon	Stefan Bogun
Quality Control Scientist	Paola Amico	Reinhard Hanuschik (future: Ferdinando Patat)

Access to VLT Data in the ESO Archive

B. LEIBUNDGUT, B. PIRENNE, M. ALBRECHT, A. WICENEC, and K. GORSKI

The science archive at ESO doesn't just collect the data from the telescopes, it has a number of other functions. These include the distribution of the service mode data obtained at the VLT, the immediate availability of all calibration data from all telescopes from which data are archived (in addition to the VLT data we are currently archiving the data from the 3.6-m, the NTT, and the 2.2-m), the public access to the science data after the proprietary period has expired, and the collection of all master calibrations. Other services offered through the archive are the seeing databases from La Silla and Paranal, several astronomical catalogues (e.g. USNO, GSC 1, Tycho-2), and on-line access to the digital sky survey, among other things. The archive is a joint operation of the ECF and ESO and contains all the HST data as well. The archive staff is shared between these two groups. The ESO archive is accessed at <http://archive.eso.org> or by clicking on 'Observing Facilities and Operations' on the ESO home page (<http://www.eso.org>) and then choosing the 'Science Archive Facility'. This article gives an overview over the current status and some of the new features in the ESO/HST archive.

1. Data Available in the Archive

Currently the archive collects data from FORS1 and ISAAC at UT1, EFOSC2 and CES at the 3.6-m, EMMI, SUSI2, and SOFI at the NTT and the Wide-Field Imager (WFI) at the MPG/ESO 2.2-m. A graphical overview over the number of data sets in the archive at the beginning of February

2000 can be seen in Figure 1 for the ESO and Figure 2 for the HST archive, respectively. The commissioning and science verification data of UVES and FORS2 have already entered the archive. Relevant information on each observation is entered into a relational database, which can be queried through a Web page. The database can be searched for specific celestial objects by their regular names (resolved to positions by querying either SIMBAD or NED), position on the sky, by ESO's programme identification, data type, telescope or instrument, or any combination of these parameters. In addition, the FITS headers of the VLT data are included online and for FORS1 imaging data previews can be investigated. Archive data can be requested through the results page of any query. Please note that you have to be a registered user of the ESO/ECF archive to retrieve data. Registration can be done directly from the archive Web page.

EMMI/NTT data have systematically been archived since 1991 (see *The Messenger* No. 93, page 20). The other telescopes and instruments have been added continuously. The one-year proprietary period for the first VLT data will expire at the beginning of April and all further science data will successively become public. The raw commissioning and science verification data of FORS1, ISAAC, and UVES are already publicly available through the archive. The science verification data can also be retrieved in processed form at <http://www.eso.org/science/ut1sv> and <http://www.eso.org/paranal/sv>. The raw ESO Imaging Survey data (da Costa et al. 1999, *The Messenger* No. 98, page 36) can also be retrieved from the archive.

Data from the wide-field imager are entering the public domain as well.

To ease the access to the various public data sets we have created a special page (http://archive.eso.org/archive/public_datasets.html). This page contains links to the above data sets and some new test data that are publicly available. Recently, data of polarisation measurements of the bright Type II Supernova SN 1999em (IAU Circulars 7296, 7296, 7305, and especially 7355) have become available. These data have been taken during the technical night of 2 November 1999 shortly after the supernova was discovered. The raw data with some information from the night logs can be found there. We will make data sets public in the future through this page, so please keep your eyes open.

2. Data Delivery

Once you made your selection from the archive, you can request data sets from the results page. After submission of the request you will be notified by email at the address you entered when you registered. Please make sure that this address is up to date. You have a choice of which medium you prefer for the data delivery. In most cases for small (< 200 Mb) requests the data are provided through ftp. Larger requests receive the data by regular mail on CD-ROMs, like in the case of service mode programmes. For high data volumes, e.g. requests for WFI data above 10 Gb, the choice is limited to DLT tapes. Other media options are DAT tapes (DDS-1 and DDS-3 formats) and Exabyte tapes. We are now also starting to ship data on DVD-R disks.

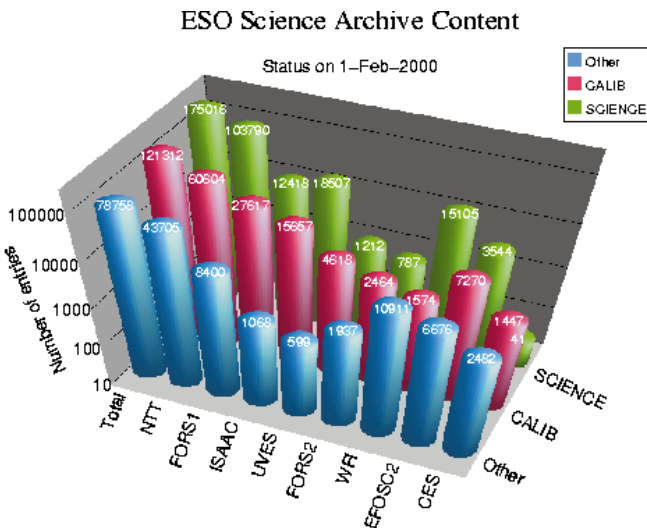


Figure 1.

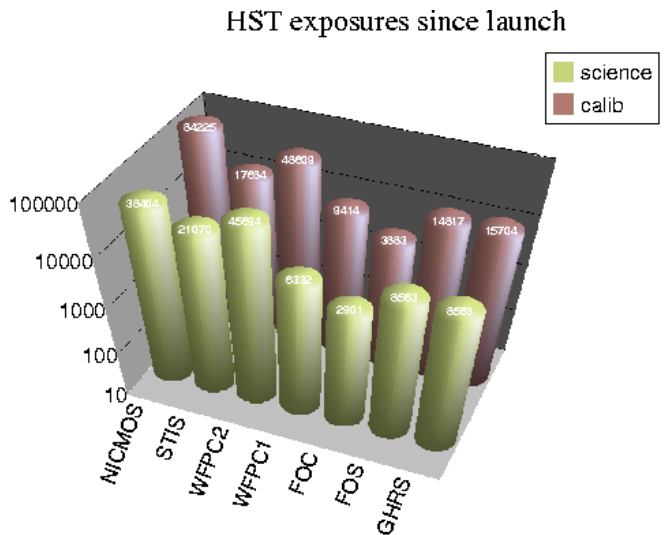


Figure 2.

Please contact catalog@eso.org for special cases.

Once the data set has been created you are again notified by e-mail about the dispatch of the data from ESO.

3. Future Developments

We are currently redesigning the archive web pages and their layout. A first example is the archive entry page (Fig. 3). This should result in an improved presentation of the available data and their usefulness for specific research projects. We also will add new parameters to the database to make sure that we cover most of the requests and make the selection criteria as varied as possible to make the searches for specific data sets easier.

A typical example is the search for calibration data that correspond to a given scientific data set. Right now, these calibrations have to be selected manually which is a tedious process. We are planning to implement a more automatic procedure in the future, which would simplify the search significantly. One of the main ongoing projects is the inclusion of the master calibration data produced by the quality control group into the archive. You then should be able to find the corresponding calibration data in a processed form in the archive.

Please let us know if you find deficiencies in the archive so that we can address them. You can contact any of us at the e-mail addresses given at the end of this article.



Science Archive Facility

The ESO/ST-ECF Science Archive is a joint collaboration of the European Southern Observatory (ESO) and the Space Telescope - European Coordinating Facility (ST-ECF). To retrieve offline observational data you have to register as an ESO/ST-ECF Archive user.

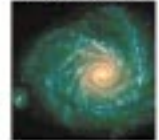
On-Line Services

- ESO Databases
VLT Science Exposures [go](#)
- HST Databases
HST Science Exposures [go](#)
- Catalogs & DSS
Digitized Sky Survey [go](#)
- Tools & Development
The JSky Initiative [go](#)
- Data Dictionaries
ESO's Data Interface [go](#)
- Related External Services
The Vizier catalogs, CDS [go](#)

News and updates

- Special Page with the Public Datasets.
- New Archive Facility Web Site: should you have any comments on the new web site layout, please send us a mail.
- Astrometric catalogs server (Hipparcos, Tycho, TRC).
- New DSS-1/DSS-2 client with Red and Blue surveys available. New client software available: just download. Interactive dss2 Blue or Red available.
- The JSky initiative: Building a repository of reusable Java Components for Astronomy.
- What's New in the Archive Web [Last update: 17 Jan 2000].

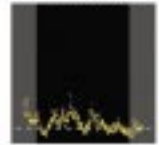
Public Datasets



Digitized Sky



Paranal Metro



Collaborations of ESO and ST-ECF Archive staff members with the Canadian Astronomy Data Centre (CADC) and the Centre des Données astronomiques de Strasbourg (CDS) take place in the areas of software development and data reduction.

ESO HOME ST-ECF HOME Help Search
Send comments to catalog@eso.org
Last modified: Tue Jan 18 15:20:49 MET 2000

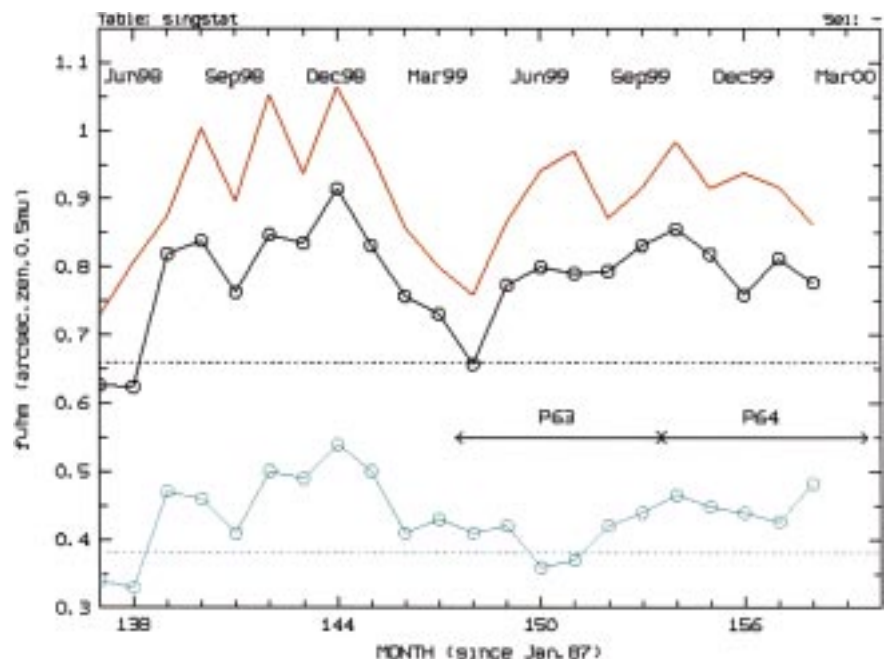
bleibund@eso.org; bpirene@eso.org – malbrech@eso.org; awicenec@eso.org – kgorski@eso.org

Chile Astroclimate, a Biannual Update

M. SARAZIN, ESO

Not long ago (*The Messenger* 97, September 99), climate change was identified as the main responsible for the degradation of observing conditions (seeing) at Paranal. It was pointed out in particular that the weakening of the traditional westerly wind pattern was more frequently allowing turbulent air from inland to blow over the coastal cordillera.

Figure 1: Seeing Statistics at Paranal since UT1 first light: monthly average (red), median (black) and 5th percentile (blue). The dashed lines give the respective long-term (1989–1995) site characteristics. Seeing is reconstructed from DIMM measurements taken at 6 m above ground, at 0.5 micron and at zenith. Because of the finite outer scale of the atmospheric turbulence, actual large-telescope image quality can be better than predicted by DIMM (see e.g.: *The seeing at the William Herschel Telescope*, R.W. Wilson et al., *MNRAS* 309, 379–387, 1999).



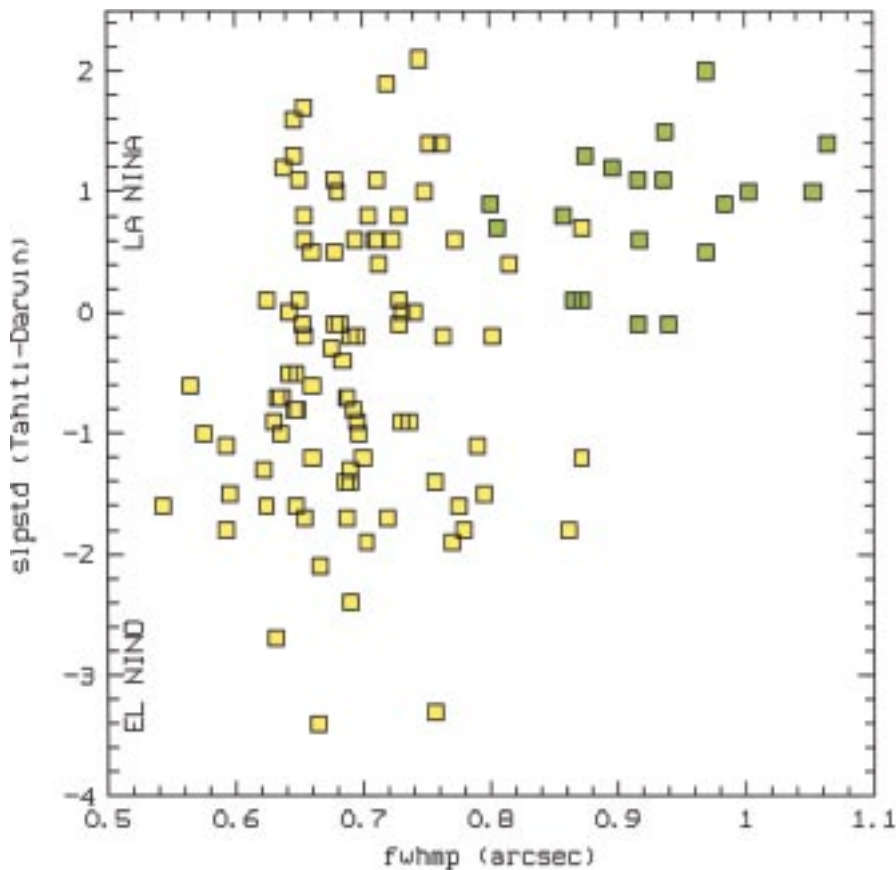


Figure 2: Correlation of the standardised monthly Southern Oscillation Index (SOI) with monthly average seeing at Paranal during 1988–1997 (yellow) and since April 1998 (green). The SOI represents the sea level pressure anomaly between Darwin and Tahiti (<http://www.cpc.noaa.gov/data/indices/>). A negative index corresponds to warmer waters (El Niño), a positive index to cooler ones (La Niña).

Six months later, and in spite of much wishful thinking, the site quality has only marginally improved and remains way below the standards established during the extensive site survey (dashed lines, Fig. 1). This means for the observatory that Period 64 should not be better than Period 63 which provided sub-half arc-second seeing only 13% of the time (R.

Gilmozzi, *The Messenger* 98, December 99, to be compared 21% in the period 1989–1995). During that same period, La Silla, which is not undergoing any visible climate change but is rather on a favourable phase of its own cycles, had been producing 8% of such good-quality observing time and promises even more in Period 64.

It was reported (*The Messenger* 90, December 1997) that cloudiness at Paranal was obviously increasing with warmer sea water, i.e., El Niño events. The dependency of Paranal seeing to El Niño cycles had been indeed similarly tested over a decade in the past (1988–1997) but without unveiling any correlation (yellow squares in Fig. 2). It was thus concluded that the basic Paranal observing conditions were weather independent. The seeing increase of the past 20 months (green squares in Fig. 2 corresponding to the period shown in Fig. 1) is mainly due to a particular North-East wind pattern which lasts part of the night, a few times per month. As shown in Figure 2, all these poor months belong to the current La Niña and the seeing trend even shows some correlation with the standardised Southern Oscillation Index (SOI) which is commonly used to define the state of the Pacific Ocean surface temperature.

The El Niño and La Niña cycles are hardly predictable and many past attempts failed. Some success was apparently obtained by a model based on solar-activity cycles which correctly predicted the 1997–1998 El Niño event (<http://www.microtech.com.au/daly/sun-enso/sun-enso.htm>). If one can believe such models, the next El Niño event should arrive in 2002, perhaps bringing to an end the current phase of poorer than average astroclimate on Paranal.

Moreover, recent analyses of sea surface elevation measured by the Topex-Poseidon satellite (NASA/JPL News release, Jan. 20, 2000) lead researchers to suspect the Niño-Niña oscillations to sit on, and therefore partially hide, a much wider (20–30 years period) so-called Pacific decadal oscillation. If this phenomenon was confirmed and quantified, it would provide new perspectives to astroclimatological surveys; let us thus wait and see.

msarazin@eso.org

ESO Demonstration Project with the NRAO 12-m Antenna

R. HEALD (NRAO) and R. KARBAN (ESO)

During the months of September through November 1999, an ALMA joint demonstration project between the European Southern Observatory (ESO) and the National Radio Astronomy Observatory (NRAO) was carried out in Socorro/New Mexico. During this period, Robert Karban (ESO) and Ron Heald (NRAO) worked together on the ESO Demonstration Project. The project integrated ESO software and existing NRAO software (a prototype for the future ALMA control software) to control the motion of the Kitt Peak 12-m antenna. ESO software from the VLT provided the operator interface and coordi-

nate transformation software, while Pat Wallace's TPOINT provided the pointing-model software.

On the 26 to 28 November, the project had its highlight – the final test with the Kitt Peak 12-m antenna at the NRAO Observatory in Tucson/Arizona. Since the test period lasted only 72 hours, it was essential to prepare, plan and test the software thoroughly and systematically. To accomplish this, practices of ESO Software Engineering were applied. ESO configuration management, systematic regression testing, build procedures, development environment, test preparation and docu-

mentation procedures were used. Using these methods enabled us to manage efforts among the various persons in the project locally, as well as to provide remote support from ESO. The project was successfully completed. For the test results and more details on the project, see <http://www.alma.nrao.edu/development/computing/news/index.html>

We would like to thank Bob Freund and the other members of the Tucson operations staff who provided us excellent system support during these three days at the 12-m.

NEWS from the NTT

O. Hainaut and the NTT Team

Since the last article in this series, the NTT has been through a complete rejuvenation process: during a period of 5 technical nights in December 1999, the main mirror has been re-aluminised and the telescope, the walls of the telescope room, and the main parking lot have been painted. The NTT looks brand new, while it has just passed its 10th anniversary.

The result of the aluminisation is excellent: the reflectivity is back to 91% and the micro-roughness to 10Å. These values are similar to those we obtained after the previous aluminisation, which took place 3.5 years ago. It should however be noted that, thanks to the weekly CO₂ cleaning and the water cleaning every 3–6 months, just before the aluminisation, the reflectivity was still at 87%, and the micro-roughness at 60Å. The amount of diffused light was measured before and after the aluminisation (using the radial profile of bright stars): a significant improvement is noted in the U, B, and V filters, of the order of 40, 30, and 20% respectively, at 40" from the star. No significant improvement was measured in R, I, J, H and K.

The outside parking lot and platform were repainted in white, in order to minimise the amount of heat that is accumulated during the day and released during the night. Be sure not to forget your sunglasses when you exit the telescope during daytime: the platform's

albedo is now very close to 1! The inner walls of the telescope room have been painted with a high-diffusion paint to cut down the reflection of the Moon during the night. Indeed, the former grey walls were quite glossy, and we often had some nasty reflections when observing with the Moon up. The telescope itself has also been painted (we did not change the colours) to protect the structure, which was starting to oxidise in places.

During Period 64, the NTT schedule includes 14 nights of service observing. Unfortunately, the weather is not very co-operative, but the programmes are being executed. The User Support Group maintains a web page where the progress of these programmes can be monitored, see URL

<http://www.hq.eso.org/observing/df/>

Since the last article, the data-reduction pipeline has significantly grown thanks to the intensive work of B. Joguet (NTT). All the imaging modes of the three instruments are now supported, and data from some of the spectroscopic modes are also processed: a couple of minutes after you take a RILD spectrum, you get a wavelength-calibrated, flat-fielded version of your spectrum. The remaining modes (i.e. echelle spectroscopy, IR polarimetry imaging) should be implemented in the coming months. Consequently, we are now keeping a library of standard

calibrations: you can request from your support astronomer the flat-field, biases, darks, etc., from the previous weeks.

SOFI, the IR spectro-imager, is still misbehaving. Over the past months, we had an alert with the closed-cycle cooling system (now under control), with the Detector Control System (under investigation, but now behaving properly) and with the Grism wheel. The latter is still not working, and is kept in the "open" position, in order to permit imaging observations. An intervention on that wheel is foreseen in April, but until that date, no spectroscopic (or polarimetric) observations will be possible. The PIs of the affected programmes have been contacted. After the April intervention, the problem should be solved in a permanent way.

To conclude this message, I am happy to announce that the change from 1999 to 2000 did not cause any problem at the NTT: we stopped the whole system on December 31 at 18:00 (the control room with all its 17 switched-off monitors is a depressing sight), and restarted everything at 21:30 (January 1, 2000, 00:30 UT). By 23:30, i.e. after the time to start everything, we were on the sky.

Finally, the IR staff position has finally been filled: Leonardo Vanzi, former NTT fellow, is now the SOFI instrument scientist.

New Pictures from Paranal Observatory



Imaging With UT1/FORS1: The Fossil Record of Star-Formation in Nearby Dwarf Galaxies

E. TOLSTOY¹, J. GALLAGHER², L. GREGGIO³, M. TOSI³, G. DE MARCHI¹
M. ROMANIELLO¹, D. MINNITI⁴, A. ZIJLSTRA⁵

¹ESO; ²University of Wisconsin, Madison, WI, USA; ³Bologna Observatory, Italy;
⁴Universidad Católica, Santiago, Chile; ⁵UMIST, Manchester, United Kingdom

Abstract

In August 1999 we used FORS1 on UT1 in excellent seeing conditions over three nights to image several nearby galaxies through the B and R broadband filters. The galaxies observed, Cetus, Aquarius (DDO 210) and Phoenix, were selected because they are relatively close-by, open-structured dwarf irregular or spheroidal systems. Owing to the excellent seeing conditions we were able to obtain very deep exposures covering the densest central regions of these galaxies, without our images becoming prohibitively crowded. From these images we have made very accurate Colour-Magnitude Diagrams of the resolved stellar population down below the magnitude of the Horizontal Branch region. In this way we have made the first detection of Red Clump and/or Horizontal Branch populations in these galaxies, which reveal the presence of intermediate and old stellar populations. In the case of Phoenix, we detect a distinct and populous blue Horizontal Branch, which indicates the presence of quite a number of stars >10 Gyr old. These results further strengthen evidence that most, if not all, galaxies, no matter how small or metal poor, contain some old stars. Another striking feature of our results is the marked difference between the Colour-Magnitude diagrams of each galaxy, despite the apparent similarity of their global morphologies, luminosities and metallicities. For the purposes of accurately interpreting our results we have also made observations in the same filters of a Galactic globular cluster, Ruprecht 106, which has a metallicity similar to the dwarf galaxies.

1. Introduction

Deep Colour-Magnitude Diagrams (CMDs) of resolved stellar populations provide powerful tools to follow galaxy evolution directly in terms of physical parameters such as age (star formation history, SFH), chemical composition and enrichment history, initial mass function, environment, and dynamical

history of a system. Some of the physical parameters that affect a CMD are strongly correlated, such as metallicity and age, since successive generations of stars may be progressively enriched in the heavier elements. Thus, detailed numerical simulations of CMD morphology are necessary to disentangle the complex effects of different stellar populations overlying each other and make an effective quantitative analysis of possible SFHs (e.g., Tosi et al. 1991; Tolstoy and Saha 1996; Dohm-Palmer et al. 1997). For every galaxy for which an accurate CMD has been derived, down to the Horizontal Branch (HB) luminosity ($M_R \sim 0. \pm 0.5$) or fainter we have learnt something new and fundamentally important about the SFH that was not discernable from images containing the red giant branch (RGB) alone (e.g., Smecker-Hane et al. 1994; Tolstoy et al. 1998; Cole et al. 1999).

Accurate CMD analysis benefits enormously from the high spatial resolution and excellent image quality, as crowded-field stellar photometry is ex-

tremely sensitive to seeing, which affects both the degree of crowding and the speed with which an image becomes sky noise limited. Previous programmes on ESO telescopes have been carried out with the 2.2-m telescope (e.g., Tosi et al. 1989) and more recently with the NTT (e.g., Minniti and Zijlstra 1996). Here we show that in ideal conditions, and with a large, high-performance telescope and closed-loop active optics spectacular improvements can be obtained on previous results.

Because of the significant gains in image quality and collecting area now available with the VLT on Paranal, it is worthwhile and fundamentally important to survey resolved stellar populations down to the HB of all nearby galaxies in our Local Group and beyond (see Fig. 1). This will provide a uniform picture of the evolutionary properties of galaxies with a wide variety of mass, metallicity, gas content, etc. and thus guide our understanding of galaxy evolution in conditions of extremely low metallicity, presumably similar to those

Table 1: The Sample

Object	Distance (kpc)	M_V	[Fe/H] (dex)	type	ref
Aquarius	800	-10.0	-1.9	dl/dSph	Mateo 1998
Phoenix	445	-10.1	-1.9	dl/dSph	Mateo 1998
Cetus	800	-10.1	-1.7	dSph	Whiting et al. 1999
Ruprecht 106	20	-6.45	-1.7	globular cluster	Da Costa et al. 1992

Table 2: The Observations

Galaxy	date	filter	exp. time (secs)	<seeing> (arcsec)
Aquarius	17Aug99	R	3000	0.45
		B	3600	0.45
Phoenix	19Aug99	R	1600	0.80
		B	1800	0.80
Cetus	17Aug99	R	3000	0.45
		B	3600	0.55
Ruprecht 106	19Aug99	R	30	0.60
		B	80	0.75

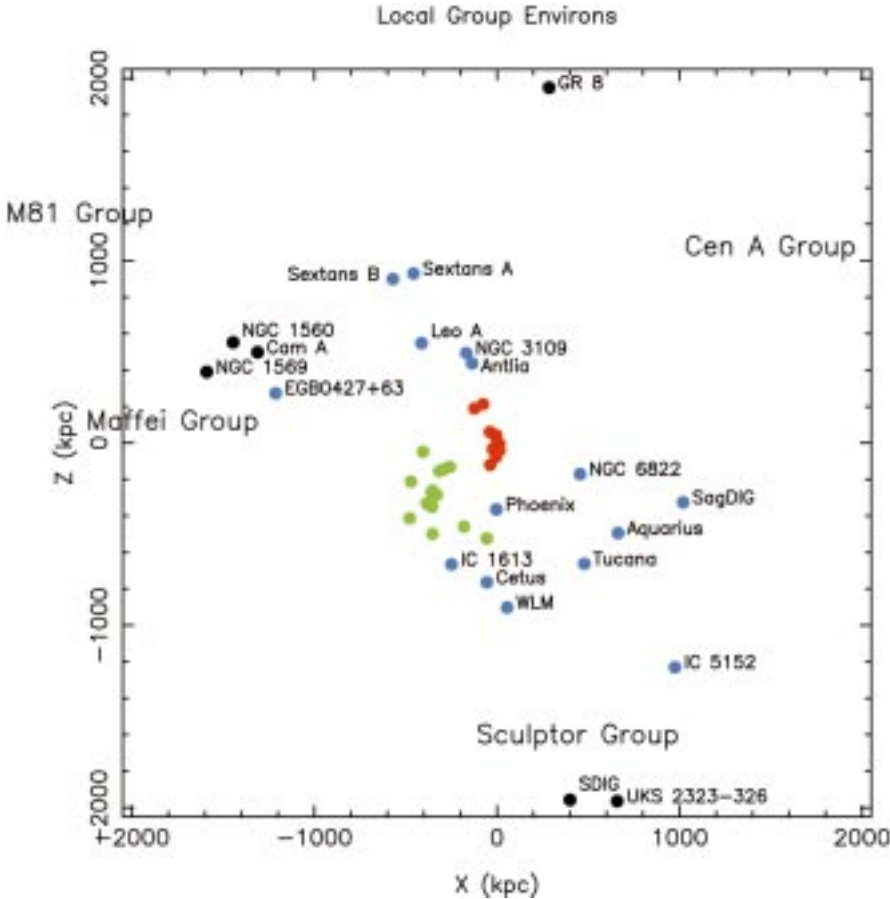


Figure 1: The spatial distribution of the Local Group plus neighbouring galaxies in X-Z galactic coordinates. Our Galaxy is at the origin of this plot, and our dwarf spheroidal neighbours are all marked by red dots. M31 and its colony of neighbouring dwarf ellipticals and spheroidals are marked in green. The more free-floating dwarf irregular/spheroidal galaxy components of the Local Group are marked in light blue dots (including Aquarius, Phoenix and Cetus) and also labelled. In black are the more distant galaxies on the fringes of the Local Group. This figure was kindly provided by Mike Irwin, and comes from Whiting et al. (1999).

expected in the early Universe. A complete survey of the SFH of the nearby Universe should also be broadly consistent with those determined from high redshift surveys (e.g., Steidel et al. 1999).

2. The Sample

Despite the advances in ground-based image quality at the VLT, we still have to carefully select galaxies that will be relatively uncrowded, i.e. systems with a stellar density of 0.01–0.5 stars/arcsec², down to the magnitude of the HB region. Dwarf Irregular (dI) and Spheroidal (dSph) galaxies at 400–800 kpc distance fit perfectly into this category (see Table 1). These types of galaxies are also the most numerous in the Local Group (see Fig. 1) and beyond, and there is considerable evidence for widely varying evolutionary histories, with periods of active star formation interspersed with quiescent periods (e.g., Smecker-Hane et al. 1994; Gallart et al. 1999). They have thus been suggested as good candidates for present-day counter-parts to the “faint blue galaxies” seen in redshift surveys

(e.g., Ellis 1997). Two of the objects we looked at are known as “transition” objects, which means they are intermediate in class between dSph (no current star formation, or HI gas) and dIs (current star formation and HI gas), and are particularly interesting because they may help us to understand why galaxies may turn on and off their star-formation process galaxy-wide and thus why dwarf galaxies can exhibit such widely differing SFHs.

3. The Observations

Our observing run, from 17–19 August 1999, had varying seeing conditions (0.3”–0.9” on the seeing monitor), but there were several periods lasting 1–2 hours with stable, excellent seeing. It was these periods which we used to image the resolved stellar populations of nearby galaxies. At other times we observed in narrow-band filters, or went to a separate programme of spectroscopy of individual stars in nearby galaxies. We present the data for three of the galaxies we imaged during our run (see Table 2). The sensitivity characteristics of the FORS1 CCD

(Tektronix) led us to observe in B and R filters. The B filter is very useful for characterising HB morphology, especially the blue HB.

We typically split our observations into short (500–600 sec) dithered groups of images to help minimise flat-fielding problems and removal of cosmic rays and bad pixels. The readout characteristics of the CCD with FIERA (4-port readout in 27 secs, with a read noise of $\sim 6 e^-$) make this an efficient way to observe. To make an accurate photometric solution, we made observations at a different airmass of a standard field (PG1657) containing several stars over a large range in colour ($B - R = -0.21$ – 1.64) on our first night. We then observed two fields (PG1657 and PG2331) on the second night and one on the third at airmass close to those at which our observations were made to confirm that the photometric solution obtained on night 1 was stable all through our run, and to confirm that all three nights were clear and photometric. The photometric solution is:

$$R - R' = 27.38 - 0.018 * X - 0.025 * (B' - R')$$

$$B - B' = 27.21 - 0.213 * X - 0.039 * (B' - R')$$

where R' and B' are the observed magnitudes (in e^-/s), R and B are the true magnitudes, and X is the airmass. In Figure 2 we show the central 4 arcmin of the combined 3600 sec of B filter imaging of Cetus. The average FWHM of the more than 11,000 stars “photometered” over the whole 6.8 arcmin FORS1 image is 0.45”. All the extended objects visible in Figure 2 are distant galaxies *behind* Cetus.

4. Results

We carried out PSF fitting photometry using a modified version of DoPHOT, following the precepts laid out by Saha et al. (1996), over each of our reduced and combined images, and matched the stars detected with sufficient signal-to-noise in both filters. The resulting calibrated but not reddening corrected CMDs are shown in Figure 3. These are the most detailed CMDs ever made from the ground of such distant systems.

In each CMD in Figure 3 we have clearly detected the Red Clump (RC) / HB region ($M_R \sim 0 \pm 0.5$). This region contains an evolutionary sequence of Helium Burning low-mass stars 1 Gyr and older. The relative number of stars in each phase determines the age mix of the stellar populations older than 1 Gyr. There is a clear diversity of morphologies in Figure 3, where each galaxy (and the globular cluster) are all distinctly different suggesting quite different past SFHs.

The *Aquarius dwarf* which was also studied in the original ESO-MPI/2.2-m study (Greggio et al. 1993), has recently been shown to be at a distance consistent with Local Group membership (Lee et al. 1999). Its CMD (Fig. 3a) has a narrow RGB ($B - R > 1.2$), and what looks like a relatively young RC ($M_R \sim -0.5$, $B - R \sim 1.1$), and very little, if any, older HB population. It also has evidence of a fairly young stellar population from He burning blue loop stars (sequence going left to right in the CMD between $M_R \sim -4$ and -0.5 and in colour $B - R \sim 0$ and 1 and intersecting with the RC) and a main sequence (vertically at $M_R \sim 0$). Aquarius thus appears to resemble Leo A, a galaxy which is completely dominated by stars younger than 2 Gyr (Tolstoy et al. 1998).

The *Phoenix dwarf* CMD (Figure 3b) has an extraordinarily complex HB and possibly an overlying, young RC. The distinct and well populated blue HB (at $M_R \sim 0$ and $B - R \sim 0 \pm 0.2$ to $B - R \sim 0.4$) is an unambiguous indication that this galaxy contains quite a number of stars that are older than 10 Gyr. There are also a sprinkling of young main-sequence and blue loop stars, as defined for Aquarius. This looks like a galaxy that has been forming stars, perhaps on and off, for a Hubble time.

The *Cetus dwarf* is a newly discovered member of the Local Group (Whiting et al. 1999). From this CMD (Fig. 3c) it looks like it may contain a blue HB population, although much less prominent than the one in Phoenix. It has a very densely populated red HB/RC (lying between $B - R \sim 0.5$ and 1.2), with a lot of structure that might resemble that predicted in the recent models of Girardi (1999). This galaxy is probably predominantly of intermediate age, and there is no evidence for star formation in the last 1.5 Gyr or so.

Ruprecht 106, a Galactic globular cluster, known to have a similar metallicity as these galaxies (Da Costa et al. 1992), was also observed as a basic test of our calibration and modelling procedures. From the CMD (Fig. 3d) we made an RGB and an HB fiducial line, to facilitate the comparison between it and the galaxy CMDs. These lines are overplotted in red on each of the galaxy CMDs in Figure 3. The normalisation is somewhat arbitrary because careful modelling has not yet been made to ascertain the optimum reddening and distances with these new accurate CMDs. Ruprecht 106 is a single old population (12–13 Gyr old), whereas all the galaxies are composite with a spread of age and/or metallicity broadening their HB/RC and RGB. However, Ruprecht 106 serves as a good starting point to characterise the properties of each galaxy, and we will also use it to help determine how accurate the theoretical isochrones are.



Figure 2: This is a $4'$ square piece of a FORS1 image in the centre of the Cetus dwarf galaxy, taken through the B filter. It is the composite of six 600sec images. Each image was registered to the nearest pixel and co-added. On the resulting images the stellar sources have a PSF measuring FWHM $\sim 0.45''$. The extended sources seen in this image are galaxies behind Cetus.

5. Interpreting Colour-Magnitude Diagram Morphology

These data will be fully interpreted using quantitative synthetic modelling techniques – making use of theoretical stellar evolution tracks (e.g., Girardi et al. 2000) and, where possible, globular/open cluster observations.

The Main-Sequence and Blue-Loop stars are fairly straightforward indicators of what the star formation rates have been in these galaxies for the last 0.5–1 Gyr. The RGB is an indicator of star formation which has taken place more than ~ 1 Gyr ago. Unfortunately it is not straight forward to disentangle the details of the precise SFH more than 1 Gyr ago because of difficulties like the age-metallicity degeneracy. That the galaxy RGBs are spread in colour in comparison to Ruprecht 106 RGB is clear, but the effects which cause this can be either or both of age and metallicity variations.

We can obtain additional information on the older populations from the RC/HB populations. The RC evolves strongly with age through the 1–6 Gyr age range (Caputo et al. 1995, Tolstoy 1998), and if we are lucky enough to have a population in this age range, quite a lot can be said about the SFH of

this galaxy. After about 6–8 Gyr, we start to see a red HB extension to the RC. This feature in Cetus and Phoenix probably means that in addition to RC populations a few Gyr old, there are also populations older than ~ 6 Gyr. In the case of Phoenix the presence of a blue HB population is a definitive indicator of an ancient stellar population older than 10 Gyr.

However, although the HB region of a CMD provides the brightest unambiguous indicators of old and intermediate stellar populations, it is difficult to use them to uniquely quantify ancient star formation rates. Basically the problem is that the colour spread of observed HBs cannot be reproduced by theoretical isochrones without invoking variable amounts of mass loss from the RGB progenitors. This is often called the “Second Parameter Effect” (e.g., Fusi Pecci & Bellazzini 1997) which results in some metal poor clusters having redder HBs than models of their metallicity would predict. Thus it is possible for globular clusters of identical age and metallicity to have very different HBs. The implications for a composite population in a galaxy of unknown age and metallicity variations are clearly dire. However, careful modelling of the number of stars on a HB

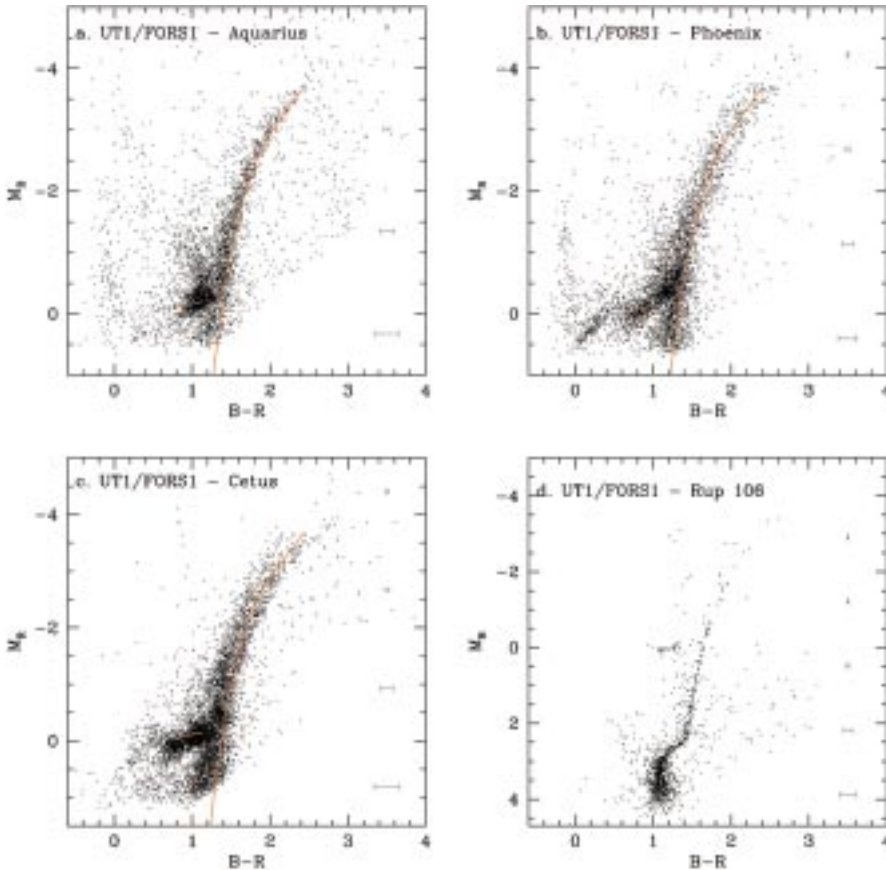


Figure 3: Here are plotted the Colour-Magnitude Diagrams which resulted from the data summarised in Table 2 for the Cetus, Aquarius and Phoenix dwarf galaxies, and the globular cluster Ruprecht 106. Representative error bars are also plotted for each data set. These data have not been corrected for any reddening effects. From the Ruprecht 106 data a fiducial mean was found for the ROB and HB. This is then overplotted on each of the galactic CMDs in red. An accurate fit has not been made, these have just been overlaid on each CMD for the purposes of comparison only. Before accurate conclusions can be drawn a detailed analysis of the reddening and distance uncertainties in all cases have to be made.

(and not where they lie) in conjunction with the RC and the RGB can constrain the plausible SFHs and put limits on the number of stars which could have been formed more than 6–8 Gyr ago, even if the precise SFH at these times cannot be extracted (e.g., Han et al. 1997; Gallagher et al. 1998; Tolstoy et al. 1998; Tolstoy 1998). The ratio of red to blue HB stars can also be used as an indicator of the age and metallicity spread of the oldest stellar populations in a galaxy (e.g., Da Costa et al. 2000).

6. Summary

The earliest epochs of star formation in the Universe must have occurred in low-metallicity environments. The only place where we can study on-going extremely low metallicity star formation in detail is in nearby dwarf irregular galaxies. They typically have metallicities in the range 3–10% of solar values (e.g., Skillman et al. 1989). Looking at galaxies which appear to be in transition between a period of star formation and a period of quiescence may help to determine what can effect star formation on a galaxy wide-scale (albeit a small galaxy) and result in the tre-

mendous diversity of SFHs seen in dwarf galaxies.

The SFH of the nearby universe should also reflect that determined from redshift surveys (e.g., Steidel et al. 1999). To make this comparison an accurate one, we need data like these to determine when nearby galaxies, even the smallest ones, formed most of their stars and if bursts were ever common enough or bright enough to produce faint blue galaxies at intermediate redshifts (e.g., Tolstoy 1998). The giant galaxies (M 31, the Galaxy, M 33) contain something like 90% of the stellar mass in the Local Group, so this is undeniably where the dominant mode of star formation occurs. However, the concern remains that, because the properties of faint blue galaxies resemble more late-type irregular galaxies, the redshift surveys are picking up dwarf systems which are very bright for only a short time and do not constitute a significant fraction of the star formation in the universe (e.g., Fukugita et al. 1998, Tolstoy 1998).

To date, the limiting factors in determining accurate SFHs in the Local Group have been crowding, sensitivity and resolution limits for accurate stellar

photometry. HST first showed us the magnificent improvements in understanding SFHs from CMDs made possible by high-resolution imaging (e.g., Tolstoy 1999). The large collecting area and impressive image quality and stability of UT1 combined with the extremely good seeing attainable at Paranal makes it possible to obtain accurate CMDs of relatively uncrowded dl/dSph systems. FORS1 also allows us to extend our knowledge of faint stellar populations into the blue, something with which HST has difficulty, and also to image the entire area of a dwarf galaxy (typically 3–5' across) in one shot. FORS1 is thus an extremely important complement to WFPC2 on HST, which is needed to push deeper down the main sequence to detect faint main-sequence turnoffs to quantify the contribution of the older populations seen in the HB. FORS imaging would inevitably have crowding problems at these faint magnitudes and with the increase in crowding.

We have shown that under good conditions the VLT can deliver high-quality images that result in exquisitely detailed CMDs which can be used to determine the SFHs of all the galaxies in our Local Group and ways beyond. It is also worth looking further afield to start surveying the high-mass stellar populations of other groups.

Acknowledgements: We thank the support staff at Paranal Observatory (particularly Thomas Szeifert, Andreas Kaufer and Chris Lidman) who helped us to make very efficient use of the telescope.

References

- Caputo F., Castellani V. & Degl'Innocenti S. (1995) *A&A*, **304**, 365.
- Cole A.A., Tolstoy E., Gallagher J.S., Hoessel J.G., Mould J.R., Holtzman J.A., Saha A., & the WFPC2 IDT team 1999 *AJ*, **118**, 1657.
- Da Costa G.S., Armandroff T.E. & Norris J.E. 1992 *AJ*, **104**, 154.
- Da Costa G.S., Armandroff T.E., Caldwell N. & Seitzer P. 2000 *AJ*, in press (astro-ph/9911020).
- Dohm-Palmer R.C., Skillman E.D., Saha A., Tolstoy E., Mateo M., Gallagher J.S., Hoessel J. & Chiosi C. 1997 *AJ*, **114**, 2514.
- Ellis R. 1997 *ARAA*, **35**, 389.
- Fukugita M., Hogan C.J. & Peebles P.J.E. (1998) *ApJ*, **503**, 518.
- Fusi-Pecci F. & Bellazzini M. 1997 *Third Conference on Faint Blue Stars*, in press (astro-ph/9701026).
- Gallagher J.S., Tolstoy E., Saha A., Hoessel J., Dohm-Palmer R.C., Skillman E.D. & Mateo M. 1998, *AJ*, **115**, 1869.
- Gallart C., Freedman W.L., Aparicio A., Bertelli G. & Chiosi C. 1999 *AJ*, **118**, 2245.
- Girardi L. 1999 *MNRAS*, **308**, 818.
- Girardi L., Bressan A., Bertelli G. & Chiosi C. 2000 *A&A*, **141**, 371.
- Greggio L., Marconi G., Tosi M. & Focardi P. 1993 *AJ*, **105**, 894.
- Han M., Hoessel J.G., Gallagher J.S., Holtzman J. & Stetson P.B. 1997, *AJ*, **113**, 1001.

Minniti D. & Zijlstra A. 1996 *ApJ*, **467**, L13.
 Lee M.G., Aparicio A., Tikonov N., Byun Y.-I. & Kim E. 1999 *AJ*, **118**, 853.
 Saha A., Sandage A., Labhardt L., Tammann G.A., Macchetto F.D. & Panagia N. 1996 *ApJ*, **466**, 65.
 Skillman E.D., Kennicutt R.C. & Hodge P. 1989 *ApJ*, **347**, 875.
 Smecker-Hane T.A., Stetson P.B., Hesser J.E. & Lehnert M.D. 1994 *AJ*, **108**, 507.

Steidel C.C., Adelberger K.L., Giavalisco M., Dickinson M. & Pettini M. 1999, *ApJ*, **519**, 1.
 Tolstoy E. & Saha A. 1996, *ApJ*, **462**, 672.
 Tolstoy E., Gallagher J.S., Cole A.A., Hoessel J., Saha A., Dohm-Palmer R.C., Skillman E.D., Mateo M. & Hurley-Keller D. 1998, *AJ*, **116**, 1244.
 Tolstoy E. 1998, XVIIIth Moriond Astrophysics Meeting: *Dwarf Galaxies and*

Cosmology, eds. T.X. Thuan et al., in press (astro-ph/9807154).
 Tolstoy E. 1999, IAU Symposium 192, *The Stellar Content of Local Group Galaxies*, eds. Whitelock & Cannon, p. 218.
 Tosi M., Focardi P., Greggio L. & Marconi G. 1989, *The Messenger*, **57**, 57.
 Tosi M., Greggio L., Marconi G. & Focardi P. 1991, *AJ*, **102**, 951.
 Whiting A.B., Hau G.K.T. & Irwin M. 1999, *AJ*, **118**, 2767.

FIRES at the VLT: the Faint InfraRed Extragalactic Survey

M. FRANX¹, A. MOORWOOD², H.-W. RIX³, K. KUIJKEN⁴, H. RÖTTGERING¹,
P. VAN DER WERF¹, P. VAN DOKKUM¹, I. LABBE¹, G. RUDNICK³

¹Leiden Observatory, ²ESO, ³MPIA, ⁴University of Groningen

One of the unique capabilities of the VLT is the near-infrared imaging mode of ISAAC. The wide field of view, detector stability, and image quality that ISAAC can provide are currently unparalleled at other observatories.

In order to take advantage of this window of opportunity, we have proposed a non-proprietary, deep imaging survey. The survey consists of very deep exposures in the J_s , H and K_s bands of the Hubble Deep Field South (Williams et al. 2000), and somewhat shallower imaging on a wider field in the cluster MS1054-03 at $z = 0.83$ (Gioia and Luppino 1994, van Dokkum et al. 1999, 2000). The survey is aimed at the study of distant galaxies in both fields, although many other applications will be possible. The same fields are observed at other wavelengths by several other groups. The full complement of data will range from the radio to the X-ray. The fields were selected based on their superb optical imaging from the Hubble Space Telescope. Both fields will be observed for a total of 96 hours, split evenly between J_s , H and K_s . In the field of MS1054-03, this integration time will be divided between four pointings to cover the full Hubble Space Telescope mosaic of images (van Dokkum et al. 2000). For the Hubble Deep Field South, one single pointing will cover the WFPC image. The expected depth of the images is a K_s magnitude of 24.4 (26.3) in the HDF South, and a K_s magnitude of 23.7 (25.6) in MS1054-03; these are 3σ limits in Johnson and AB magnitudes, respectively. The OPC has been very generous and has allocated the full requested time to this survey.

The first data on the Hubble Deep Field South were obtained at the end of 1999. Even the first quarter of the total integration provided K_s -band data of unprecedented image depth and quality for the HDFs. A colour image is

shown in Figure 1, which is a combination of the HST I band data, and J_s and K_s ISAAC data. The variations among the infrared colours of galaxies are striking, and several very red galaxies are immediately apparent in the image.

Some of these galaxies are absent, or very faint in the extremely deep I band data from the Hubble Space Telescope.

Some examples of distant galaxies are shown in Figure 2. The morphologies of the very red galaxies span a

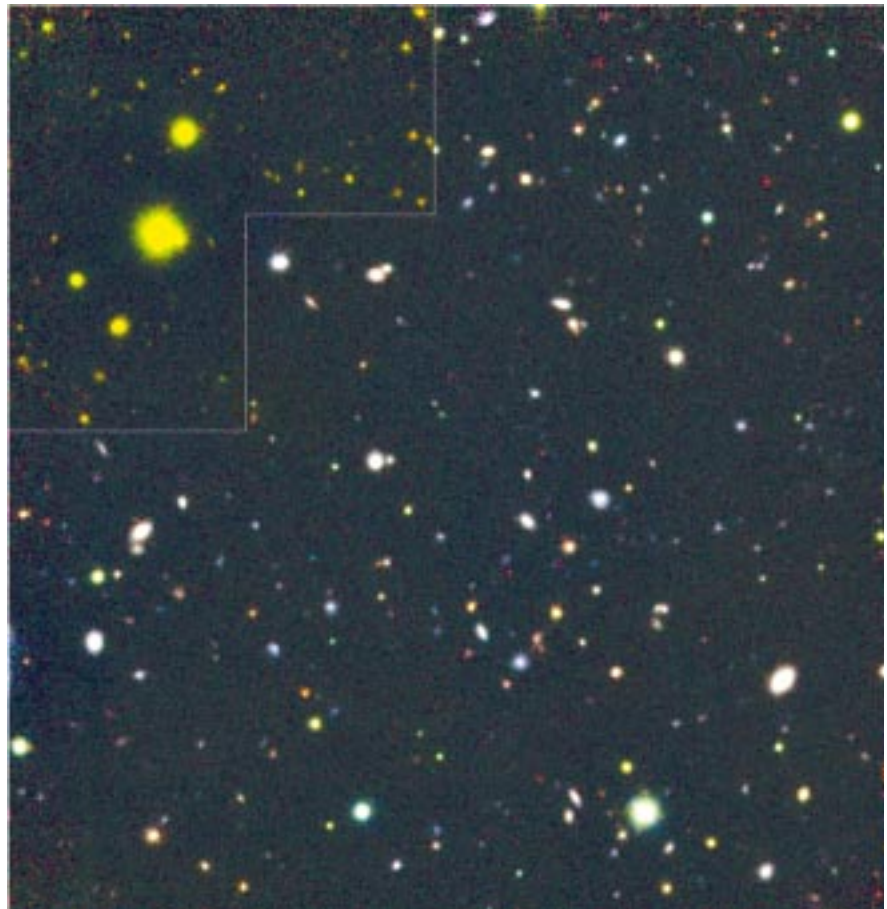


Figure 1. A colour image of the Hubble Deep Field South, observed with the Hubble Space Telescope, and ISAAC on the VLT. The colour image is constructed from the I band images from HST, and the J_s and K_s images taken with ISAAC. The outline indicates the size and shape of the WFPC2 field, and the galaxy colours outside of that are yellow-green because of the absence of I band data in the image. The great variety of galaxy colours is striking. These differences are often caused by redshift: at higher redshifts, the Balmer break and 4000 Angstrom break will move in or beyond the bandpass of the I band filter. Some very red galaxies can be identified, these have very low I and J_s fluxes.

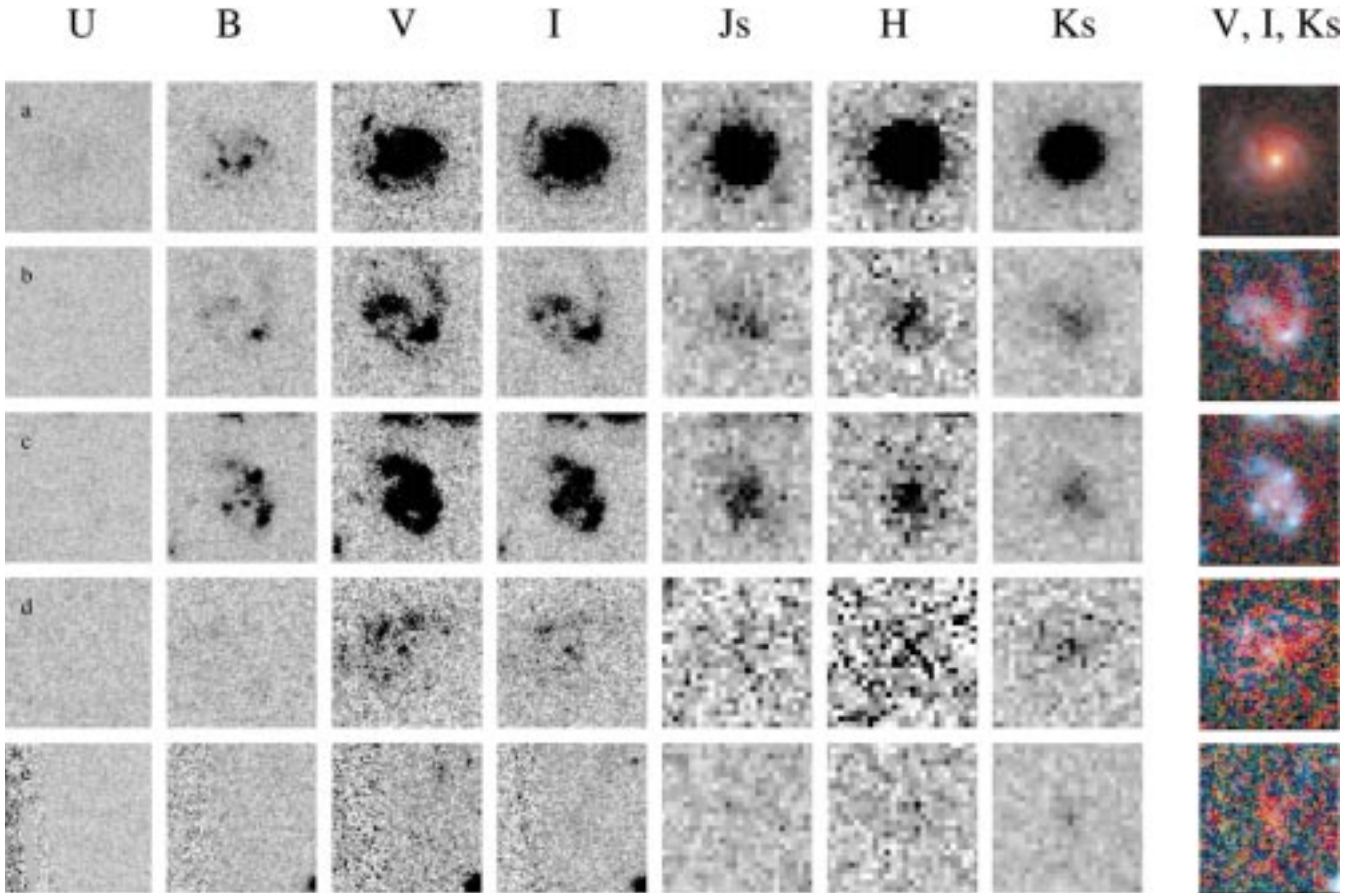


Figure 2. A close-up of several high-redshift galaxies in the Hubble Deep Field South. The individual panels show the images of the galaxies in the optical from HST (U, B, V, I), and in the infrared from the VLT (J_s , H, K_s). The differences in morphology are quite striking. Thanks to the good image quality of the VLT data, many of the galaxies are resolved in the infrared. The large galaxy in panel d is similar to spiral galaxies in the nearby universe. It is likely at a redshift above 2. The galaxy in panel e has not been identified as a galaxy from the HST-WFPC data, whereas it is bright in the infrared. Such very red galaxies can contribute substantially to the stellar mass density at high redshift.

wide range: some are compact at all wavelengths, others are compact in the infrared, but much more extended in the optical wavelengths. The very red colours of these galaxies are likely caused by the redshifted Balmer or 4000-Angstrom breaks or by dust. The spectral energy distributions of three of the galaxies are shown in Figure 3. The redshift of the galaxy in Figure 3a is expected to be above 1.6, whereas the others are expected to be above 2 based on their spectral energy distribution.

Some of the morphologies are quite remarkable. The very large galaxy in Figure 2d is an example. It is very extended in the I band, which most likely corresponds to the rest-frame UV. The HST images show spiral structure, similar to that of spiral galaxies nearby. The K_s band image show a centrally concentrated component, which is likely the bulge of the galaxy. This galaxy is therefore possibly the progenitor of a large-disk galaxy at low redshift. If this is confirmed with deeper data, it would be in conflict with theories of disk formation which predict generally small disks at high redshift. Another striking example is shown in Figure 2e. This galaxy has extremely weak I band emission, and was not included in the source list of galaxies for the HDF South (Williams et al. 2000), but we

note that it is close to the edge between WF and PC. The galaxy in Figure 2c is red in the I- J_s , but very blue in the optical colours. It is a regular Ly-Break galaxy, with a remarkable difference in morphology between the IR and optical. The Ly-break would predict the Balmer break to occur further to the red (redward of J_s). Further study is required to see whether dust or other factors may play a role.

The first results of the survey are very promising. When the survey is completed, it will be unique in terms of depth and coverage. The data can be used for many purposes: the study of J drop-out objects, which are possibly the highest redshift galaxies (e.g., Dickinson et al. 1999); the study of the rest-frame optical properties of Ly-break galaxies, the determination of photometric redshifts of a large sample of galaxies, especially for galaxies with redshifts between 1 and 3; the weak lensing signal in the Hubble Deep Field South and MS1054-03, aided by accurate photometric redshifts; the faint end of the luminosity function at lower redshifts, both for the field and MS 1054-03, etc.

One of the interesting applications is the selection of distant galaxies purely based on their observed infrared fluxes. As we have shown in Figures 2 and 3, some galaxies are very red in their J_s -

K_s and/or J_s -H colours. These galaxies are so faint in the optical, that they will generally not be in samples selected by the Ly-break technique (Steidel et al. 1996). Nevertheless, their contribution to the total (rest-frame) optical luminosity density at high redshift can be quite substantial. Given the fact that their mass-to-light ratio is also expected to be higher than that of Ly-break galaxies, their contribution to the stellar mass density at high redshift could be significant. Analysis of this aspect is in progress.

The reduced data of the survey will be made available to the public. We expect a first release of the preliminary HDF South data later this year. The data reduction is relatively complex due to the large number of frames taken in jitter mode, some of which were affected by scattered moonlight. For the most accurate astrometry and combination with other images, it is also necessary to correct for a small amount of field distortion.

We have currently written our own reduction routines based on the IRAF "dimsum" package. The observations on the cluster field MS1054-03 are expected to be done soon, but they have not yet started.

Updates on the programme can be found at our web site <http://www.strw.leidenuniv.nl/~franx/fires>.

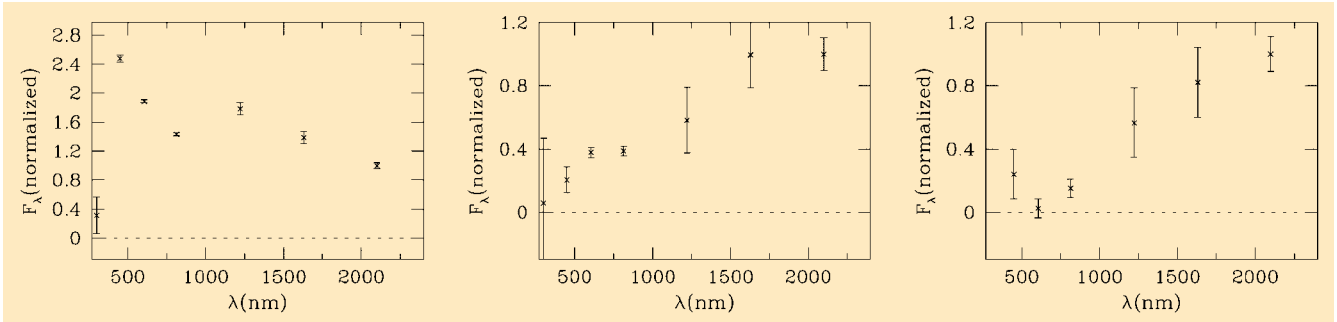


Figure 3: The normalised spectral energy distribution of 3 galaxies. From left to right we show a regular Ly-break galaxy (Fig. 2c), the “spiral” galaxy (Fig. 2d), and the very red galaxy from Figure 2e. The red continuum feature of the last two galaxies can be due to the Balmer/4000 Angstrom break or due to dust. Only one of these would be selected by the regular Ly-break selection technique, as the others are too faint in the optical (rest-frame UV).

Acknowledgement

It is a pleasure to thank the staff at ESO who contributed to the construction and operation of the VLT and ISAAC. This project has only been possible because of their enormous efforts.

References

Dickinson, M., et al, 1999, preprint, astro-ph/9908083.
 Gioia, I., and Luppino, G. A., 1994, *ApJS*, **94**, 583.
 van Dokkum, P. G., Franx, M., Fabricant, D., Kelson, D., Illingworth, G. D., 1999, *ApJL*, **520**, L95.

van Dokkum, P. G., Franx, M., Fabricant, D., Kelson, D., Illingworth, G. D., 2000, submitted to *ApJ*.
 Steidel, C. C., Giavalisco, M., Pettini, M., Dickinson, M., Adelberger, K. L., 1996, *ApJL*, **462**, L17.
 Williams, R. E., et al, 2000, in preparation.

Optical Observations of Pulsars: the ESO Contribution

R.P. MIGNANI¹, P.A. CARAVEO² and G.F. BIGNAMI³

¹ST-ECF, rmignani@eso.org; ²IFC-CNR, pat@ifctr.mi.cnr.it; ³ASI bignami@asi.it

Introduction

Our knowledge of the optical emission properties of neutron stars has been remarkably improved by the results obtained during the last 15 years. At the beginning of the 80s, only two of the about 500 isolated neutron stars at that time detected as radio pulsars had been identified also at optical wavelengths. These were the two young (2000–10,000 years) optical pulsars in the Crab (Cocke et al. 1969), the first and for about 10 years the only one, and Vela (Wallace 1977) supernova remnants. Soon after the identification of the Crab, a model to explain the optical emission of young pulsars was developed by Pacini (1971) in terms of synchrotron radiation emitted by charged particles injected in the pulsar’s magnetosphere. According to this model, the optical luminosity of a pulsar is predicted to scale proportionally to B^4P^{-10} , where B and P are its magnetic field at the light cylinder and its period, respectively. This relation, known as the “Pacini’s Law”, proved correct for both the Crab and the Vela pulsars and was thereon assumed as a reference.

The panorama of neutron stars’ optical astronomy changed rapidly when few more pulsars started to be identified (or discovered) in the X-ray data of the EINSTEIN satellite (see Seward and Wang 1988 for a review) and a possible X-ray counterpart for the enig-

matic gamma-rays source Geminga, not yet recognised as an X/gamma-ray pulsar, was proposed. This triggered the search for their optical counterparts,

and ESO telescopes gave to the European astronomers the chance to boost a virtually new field of investigation (see Table 1 for a summary of the

	1985	90	95	00
CRAB		NTT*	2.2m*	VLT VLT
B1509–58		NTT*	3.6m* NTT*	NTT* VLT
B0540–69		3.6m 3.6m NTT*	3.6m NTT	→HST VLT
VELA	3.6m* 2.2m 3.6m*	NTT*	3.6m 3.6m NTT*	→HST VLT
B0656+14		3.6m* NTT*	→HST	
GEMINGA	3.6m*	NTT*	NTT* NTT* NTT	→HST
B1055–52	3.6m*		NTT* →HST	

IMAGING SPECTROSCOPY
TIMING POLARIMETRY

Table 1: Summary of (published) ESO observations of the pulsars with an optical counterpart. For each pulsar the observing epochs and the telescopes are listed. Observations performed by the authors are marked by an asterisk. The observing modes are specified by the colour code. Arrows indicate HST follow-ups. The results are summarised in Table 2 and described in the text.



Pulsar	Age	Id.	PM	Tim	Spec	Pol	I	R	V	B	U
Crab	3.10	Tim	Y	P	Y	Y	15.63	16.21	16.65	17.16	16.69
B1509-58	3.19	Pos		UP	-	u.l.	19.8	20.8	22.1	23.8	
B0540-69	3.22	Pos, Tim		P	Y	Y	21.5	21.8	22.5	22.7	22.05
Vela	4.05	Tim	Y	P		Y		23.9	23.6	23.9	23.8
B0656+14	5.05	Pos, Tim	Y	P			23.8	24.5	25	24.8	24.1
Geminga	5.53	PM, Tim	Y	P	Y		<26.4	25.5	25.5	25.7	24.9
B1055-52	5.73	Pos									24.9
B1929+10	6.49	Pos								>26.2	25.7
B0950+08	7.24	Pos									27.1

Table 2: Summary of the existing optical database for all the pulsars identified so far. The objects (first column) are sorted according to their spin-down age in years (second column, in logarithmic units). For PSR B1509-58 both the original and the most recent candidate counterparts are reported. The row colour identifies (in increasing intensity) young, middle-aged and old pulsars. The 3rd column gives the identification evidence either from positional coincidence (Pos), timing (Tim), proper motion (PM) or polarimetry (Pol). Proper-motion measurement, timing – either resulting in the detection (P) or non-detection (UP) – of optical pulsations, spectroscopy and polarimetry observations are flagged in columns 4–7. Null results (–) and upper limits (u.l.) are also noted. The remaining columns list the available (time integrated) UB-VRI photometry.

published ESO observations). Also taking advantage of the improved performances of the NTT and its new detectors, more optical identifications of X-ray pulsars were achieved in few years, some brand new, some the confirmation of previous detections obtained with the 3.6-m. In particular, middle-aged ($\geq 100,000$ years) pulsars were observed for the first time. This opened the way to the study of their optical emission properties, which turned out to be very different from the ones of young Crab-like pulsars, thus changing a well-established scenario. In parallel, fast photometry observations were pursued at the 3.6-m, also experimenting the new technology of the MAMA detectors, to monitor the light-curve evolution of the known optical pulsars and to search for new ones (a case for all: the long quest for a pulsar in SN 1987A). Last, but not least, precise proper-motion measurements of pulsars, so far obtained only in the radio band, were started at ESO using classical optical astrometry techniques, yielding results of comparable (or even higher) accuracy.

Thereafter, the stage was taken by the HST, which, exploiting its higher sensitivity in B/UV, obtained three new likely identifications and complemented the explorative work done with ESO telescopes for the pulsars already identified. Indeed, one can go as far as saying that almost all the HST time so far allocated for the study of isolated neutron stars has been a follow-up of ESO programmes (see Table 1).

Observations Review

The total number of pulsars with an optical counterpart, either secured or tentative, amounts now to nine. The available optical database (consisting of timing, spectroscopy, polarimetry

and photometry) is summarised in Table 2, where the objects have been sorted according to their spin-down age ($P/[2dP/dt]$). From the table, it can be immediately appreciated how the observations with the ESO telescopes played an important role in the optical studies of pulsars, claiming a number of absolute firsts. For each pulsar, the major results achieved so far by ESO observations are discussed in the following sections.

The Crab Pulsar

The bright pulsar (33 ms) in the Crab Nebula (PSR B0531+21) was the first one to be identified in the optical (Cocke et al. 1969). Although the Crab is relatively bright ($V = 16.6$), the first good spectrum was taken only 20 years after the pulsar discovery with EMMI at the NTT (Nasuti et al. 1996a,b). The pulsar spectrum appears flat (see Fig. 1 of Nasuti et al. 1996a), as expected from a synchrotron origin of the optical radiation, apart from an unidentified broad absorption feature observed around 5900 Å, which could be originated in the pulsar magnetosphere. Photometry of the Crab pulsar, performed at different epochs from ESO, was used to critically investigate the reality of the so-called secular decrease of the pulsar's optical luminosity. This effect, predicted by the Pacini's Law as a consequence of the pulsar's spin-down, was never convincingly measured. By comparing the V flux measurements of the Crab taken over 15 years, a decrease of 0.008 ± 0.004 mag/yr was indeed found (Nasuti et al. 1996a,b), consistent with the theoretical prediction (0.005 mag/yr), but still too uncertain to prove the reality of the effect.

PSR B1509-58

With a spin-down age close to 1500 years, the pulsar PSR B1509-58 is the youngest after the Crab. Its period ($P = 150$ ms) is relatively long with respect to the Crab one, but it spins down much faster than almost any other pulsar (Kaspi et al. 2000). A candidate counterpart to PSR B1509-58 ($V = 22.1$) was first detected by the NTT (Caraveo et al. 1994b), with a corresponding optical luminosity much higher than the one expected from the Pacini's Law. The proposed identification was investigated in the following years through multi-colour imaging, spectroscopy and timing performed at the NTT (EMMI and SUSI1/2) and at the 3.6-m, which, however, lead to inconclusive results (see Mignani et al. 1998a for a summary). In particular, the non-detection of optical pulsations raised doubts on the proposed identification. Recently, the pulsar field was observed in polarimetry mode with the FORS1 instrument at the VLT/UT1. Exploiting excellent seeing conditions (0.46"), the proposed counterpart of Caraveo et al. (1994b) was resolved in a triplet of objects. Of these, only one ($R = 25.7$) showed evidence of a significant polarisation (Wagner and Seifert 2000), as expected from pure magnetospheric optical emission from a young pulsar. Although its luminosity would still exceed the predicted one, the polarisation signature makes this new candidate a viable counterpart to PSR B1509-58.

PSR B0540-69

The fourth youngest pulsar (50 ms) known so far ($\sim 1,700$ years) is PSR B0540-69 in the Large Magellanic Cloud. With the discovery of optical pulsations (Middlethitch & Pennypacker

1985), it became the third optical pulsar after the Crab and Vela ones. When beaming effects were taken into account (Pacini and Salvati 1987), the optical luminosity of PSR B0540-69 was found to be consistent with the predictions of the Pacini's Law. The pulsar was monitored between 1989 and 1991 through fast-photometry observations performed at the ESO/3.6-m (Gouiffes et al. 1992). These observations allowed to measure very accurately the pulsar's timing parameters (dP/dt and d^2P/dt^2), to be used as input to derive the value of its *braking index*, i.e. a quantity of paramount importance for neutron star models (see e.g. Shapiro & Teukolsky 1983). Since the discovery of the weak radio emission from PSR B0540-69 is quite recent, optical (as well as X-ray) observations were the only way to perform a very accurate pulsar timing.

Although optical pulsations had been detected from the direction of PSR B0540-69 soon after the X-ray discovery, its counterpart remained unidentified due to the lack of a very precise positioning. The first deep search was carried on in January 1992 with SUSI at the NTT (Caraveo et al. 1992). The clue for identifying the optical counterpart of the pulsar came from an H α image of the host supernova remnant (SNR 0540-69), which unveiled a strange spiral-like structure, somehow recalling a sort of jet-like emission activity. A point-like source ($V = 22.5$) was indeed observed coincident with the centre of the "spiral". The identification proposed by Caraveo et al. (1992) was later confirmed by time-resolved imaging of the field performed at the NTT with the guest TRIFFID camera equipped with a MAMA detector (Shearer et al. 1994), which allowed to determine the position of the optical pulsar. Recently, a new piece of information was added by the first measurement of the pulsar's optical polarisation, obtained by Wagner & Seifert (2000) using FORS1 at the VLT/UT1.

The Vela Pulsar

The Vela pulsar (PSR B0833-45) is the older (11,000 years) of the "young pulsar" group. Together with the Crab, it is the only one originally detected on a photographic plate (Lasker 1976). Its optical pulsations (89 ms) were extensively studied by Gouiffes (1998) through fast-photometry observations carried out at the 3.6-m thus yielding the most accurate characterisation of the pulsar's light curve.

Multi-epoch imaging with the NTT and the 3.6-m was fundamental to assess the actual value of the Vela pulsar proper motion, measured several times in radio with different instruments and techniques but with conflicting results. Indeed, optical astrometry is not affected by pulsar's timing irregularities, very

frequent in the case of Vela, which hamper significantly radio proper-motion measurements. After an upper limit first obtained by Bignami & Caraveo (1988) with the 3.6-m, the measurement of the proper motion was carried out by Ogelman et al. (1989) at the 2.2-m. A few years later, the proper motion was revisited with the aid of new NTT observations by Nasuti et al. (1997a,b), who computed the angular displacement of the pulsar during 20 years and obtained a value of 52 ± 5 mas/yr, recently confirmed by DeLuca et al. (2000) using the HST.

Amongst the most recent results, imaging observations of the Vela pulsar, performed with EMMI at the NTT, allowed to improve its multicolour photometry and to add the first detection in R (Nasuti et al. 1997a). As expected from this young pulsar, the UBV flux values are clearly indicative that the optical emission is of magnetospheric origin. This conclusion is supported by the first measurement of a significant optical polarisation from the pulsar (Wagner & Seifert 2000), obtained using FORS1 at the VLT/UT1. However, as remarked by Nasuti et al. (1997a), the broad-band spectral behaviour of Vela is significantly different from the one observed in the other young optical pulsars Crab and PSR B0540-59. While in all cases the UBV colours appear to follow the same flattish spectral distribution, the relatively lower R flux of Vela represents a clear spectral turnover in the red region of the spectrum. The origin of this turnover is unclear. We note that a similar trend was observed for the Crab in the NIR region and was interpreted as a synchrotron self-absorption taking place in the pulsar magnetosphere (see Nasuti et al. 1997a and references therein).

PSR B0656+14

With a spin-down age of 100,000 years, PSR B0656+14 (384 ms) is one of the two middle-aged pulsars identified from ESO. A possible optical counterpart was detected by Caraveo et al. (1994a) in a faint ($V \sim 25$) point source detected in images obtained in 1989 (3.6-m) and 1991 (NTT) and later confirmed by an HST/WFPC2 observation (Mignani et al. 1997b). Since proper motion is a very distinctive characteristic of each pulsar, the known radio displacement of PSR B0656+14 was searched in the optical but, owing to the poorer angular resolution of the 3.6-m and NTT images, only a marginal result was obtained.

Geminga

The optical identification of the middle-aged (340,000 years) Geminga pulsar (237 ms) with a faint star named G" ($V = 25.5$), proposed by Bignami et al. (1987), was initially substantiated by its

unusual colours (Halpern & Tytler 1987). In particular, multicolour photometry observations performed at the 3.6-m (Bignami et al. 1988) showed for the first time that its optical flux distribution could not be explained by a simple spectral model, as happens e.g. for the Crab, and that different emission mechanisms were at work. A few years later, the optical identification of Geminga was supported by the measurement of the G" proper motion, obtained thanks to a new NTT/SUSI observation (Bignami et al. 1993) and later reassessed both with the NTT/SUSI (Mignani et al. 1994) and with the HST/WFPC2 (Caraveo et al. 1996). The definitive proof of the optical identification came when the gamma-ray light curve of Geminga was found to be sensitive to the G" proper motion (Mattox et al. 1996), finally closing the loop.

NTT/SUSI observations of the Geminga field were also fundamental to tie, through a multi-step astrometric procedure, the Hipparcos reference frame to the HST/WFPC2 one and to obtain the absolute coordinates of the pulsar with an accuracy of only 40 mas (Caraveo et al. 1998). This, together with the refined measurement of the proper motion, obtained by the HST (Caraveo et al. 1996), makes it possible to compute the absolute position of Geminga at a given epoch, a critical information to phase together its gamma-ray pulsations over 20 years of observations (Mattox et al. 1998).

The last, although still weak, proof of the optical identification of Geminga came recently with the tentative detection of optical pulsations from G" (237 ms), a result partially obtained using the TRIFFID camera at the 3.6-m (Shearer et al. 1998).

The Chase Goes On

A few more pulsars were observed through the years from ESO but no new optical identification was achieved. Among the best-studied targets, we recall the middle-aged (540,000 years) pulsar (197 ms) PSR B1055-52, observed for the first time from the 3.6-m (Bignami et al. 1988) and later also from the NTT. With a flux comparable to the one of Geminga (see Table 2), this pulsar would probably have been detected if it were not buried in the PSF's wings of a very close and bright star (see Fig. 1 of Mignani et al. 1997a), which made mandatory the use of the HST. The more recent (and deeper) optical investigations are those of two young pulsars: the Crab-like PSR J0537-6910 (5,000 years) and the Vela-like PSR B1706-44 (17,000 years), observed respectively with the NTT and the VLT.

The X-ray pulsar PSR J0537-6910 in the Large Magellanic Clouds supernova remnant N157B is the fastest (16

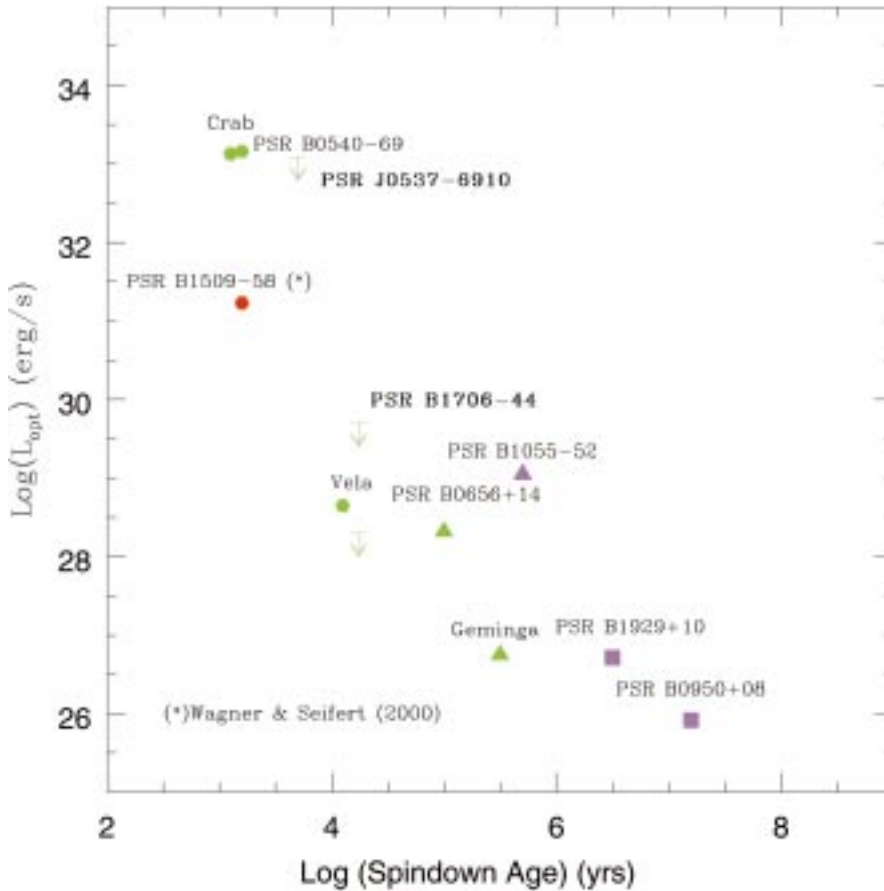


Figure 1: Extinction-corrected optical luminosities of identified pulsars plotted vs. their spin-down ages. In all cases but Geminga, for which an optical parallax measurement exists (Caraveo et al. 1996), the luminosities have been calculated assuming the nominal radio distances. Available upper limits are reported for PSR J0537-6910 and PSR B1706-44 (in this case for the extreme values of the interstellar extinction). The different symbols indicates young (hexagons), middle-aged (triangles) and old (squares) pulsars, with luminosities computed in the V (green), R (red) and U (magenta) bands.

ms) known isolated (non-recycled) pulsar and the most energetic (together with the Crab). Although the X-ray detection has been confirmed by all operating X-ray satellites, PSR J0537-6910 is still undetected in radio (see Mignani et al. 2000 and references therein). In the optical, the field was observed in 1998 in the BVI bands with the SUSI2 camera at the NTT. Few objects were detected close/inside the X-ray error circle but none of them could be convincingly associated to the pulsar, which appears undetected down to $V \sim 23.4$ (Mignani et al. 2000). This result has been independently confirmed by the upper limits on the pulsed optical flux obtained by Gouiffes & Ogelman (2000) from the reanalysis of fast-photometry observations of the field performed with the ESO fast photometer at the 3.6-m.

PSR B1706-44 is a radio/gamma-ray pulsar ($P = 102$ ms) and a weak soft X-ray source (see Mignani et al. 1999 and references therein), very similar to the Vela pulsar both in its dynamical parameters and in its multiwavelength phenomenology. After a few (unpublished) trials with the NTT, deep optical observations of PSR B1706-44 were obtained in August 1998 during the

Science Verification programme of the VLT/UT1 using the Test Camera (Mignani et al. 1999; Lundquist et al. 1999). Unfortunately, no candidate optical counterpart to the pulsar has been detected down to $V \sim 25-27$, depending on the computed image astrometry.

The General Picture

Although still incomplete, the information obtained so far is sufficient to draw a first, general, picture of the optical emission properties of pulsars (see Mignani 1998 for a review). To summarise, two different processes can contribute to the optical emission: (i) synchrotron radiation from the magnetosphere, fuelled by the neutron star's rotational energy loss dE/dt , and (ii) thermal ($T \approx 10^5-10^6$ °K) radiation from the cooling neutron star's surface, which peaks in the soft X-ray band.

The first process is dominant in young and bright objects but its efficiency seems to decay rapidly (Fig. 1), to wit, the case of the Vela pulsar, which is only 5 times older than the Crab but channels in the optical approximately a 1,000 times smaller fraction of its global energy budget. For the middle-aged and fainter pulsars, the scenario is less

clear. First, the optical luminosity falls well below the value predicted by the Pacini's Law and its dependence on the spin-down age is smoother. Second, the available multicolour flux measurements are clearly inconsistent with a single spectral model, thus implying that both the emission processes described above probably contribute to the optical luminosity. In the case of PSR B0656+14, the optical flux distribution can be fit by the combination of both a magnetospheric and a thermal component (Pavlov et al. 1997). On the other hand, for the slightly older Geminga, the optical continuum seems to be thermal with a broad emission feature at $6,000 \text{ \AA}$ (Mignani et al. 1998b), which, following the original idea of Bignami et al. (1988), has been interpreted as a possible Hydrogen cyclotron emission line originated in the neutron star's atmosphere (Jacchia et al. 1999). For older pulsars ($>1,000,000$ years), thermal emission is thought to become finally dominant over the magnetospheric one (Pavlov et al. 1996).

The Future

Although the last years marked a big step forward in the optical astronomy of pulsars, much work remains to be done to understand the emission properties of these objects. While the above picture seems substantially correct, the question of when and how the optical emission of young pulsars starts to fade away and switches from a pure magnetospheric to a thermal regime is still an open issue. Optical observations of more pulsars, especially in the age interval 5000-100,000 years, are thus crucial to find an answer. Starting from the updated pulsar database, now counting ≈ 500 additional detections (e.g. Camilo et al. 2000), future Chandra and XMM observations should pinpoint targets worth of optical follow-ups.

The knowledge of the pulsars spectra in the optical domain is also rather poor. Up to now, it was based on spectral information gathered through multicolour photometry and hidden in timing and polarimetry data. Only for the bright Crab pulsar (Nasuti et al. 1996a,b) and PSR B0540-69 (Hill et al. 1997) a rather accurate spectroscopy is available. Future observations of pulsars should certainly be more focussed on spectroscopy. Amongst young optical pulsars, Vela is certainly the one that could benefit more from a comprehensive spectral study. An accurate determination of its spectral shape would be crucial both to unveil emission/absorption mechanisms in the pulsar's magnetosphere and to trace the transition in the emission physics between young and middle-aged pulsars. Spectroscopic observations are also needed to resolve the different components (magnetospheric and thermal) so far only hinted in the multicolour flux distribu-

tion of the middle-aged PSR B0656+14 and Geminga, including possible atmospheric cyclotron lines. A joint fit of the optical/X-ray thermal components would provide a better measurement of the observed neutron star surface temperature, important to investigate both its internal structure and the physical/chemical properties of its atmosphere. On the other hand, fitting well-resolved cyclotron lines would allow to obtain the first direct measurements of the neutron star magnetic field (Bignami 1998). For Geminga, a spectrum was recently obtained from the ground (Martin et al. 1998) but with a very low S/N, while no spectroscopy observation has yet been tried for the slightly brighter PSR B0656+14.

To pursue all the above goals, deep imaging, timing and spectroscopic observations, as feasible with 8-m-class telescopes, are required. Needless to say, in all cases the VLT could offer an invaluable contribution. In particular, with FORS1 and FORS2, both Antu and Kueyen fulfil the imaging/spectroscopy requirements. On the other hand, timing observations can be performed either by using FORS2 in trailer mode (see e.g. ESO/PR 17/99) or by using MAMA detectors attached to the visitor focus of Yepun. Thus, we can certainly say that the VLT has all the potentialities to open a new era in the optical astronomy of pulsars, giving back to ESO the leadership achieved before the advent of the HST.

References

Bignami, G.F., Caraveo, P.A., Paul, J.A., Salotti, L. and Vigroux, L. 1987, *ApJ* **319**, 358.
Bignami, G.F., Caraveo, P.A. and Paul, J. A. 1988, *A&A* **202**, L1.

Bignami, G.F., Caraveo, P.A. and Vacanti, G. 1988, *A&A* **196**, 191.
Bignami, G.F. and Caraveo, P. A 1988, *ApJ* **325**, L5.
Bignami, G.F., Caraveo, P.A. and Mereghetti, S. 1993, *Nature* **361**, 704.
Bignami, G.F. 1998, *Adv.Sp.Res.* Vol. 21/1, 243.
Camilo, F. et al. 2000, Proc. of IAU Coll. N.177 PULSAR ASTRONOMY – 2000 and Beyond.
Caraveo, P.A., Bignami, G.F. and Mereghetti, S. 1994a, *ApJ Lett.* **422**, L87.
Caraveo, P.A., Mereghetti, S. and Bignami, G.F. 1994b, *ApJ* **423**, L125.
Caraveo, P.A., Bignami, G.F., Mignani, R. and Taff, L.G. 1996, *ApJ* **461**, L91.
Caraveo, P.A., Lattanzi, M., Massone, G., Mignani, R., Makarov V.V., Perryman, M.A.C. and Bignami, G.F. 1998, *A&A* **329**, L1.
Cocke, W.J., Disney, M.J. and Taylor, D.J. 1969, *Nature* **221**, 525.
De Luca, A., Mignani, R.P. and Caraveo, P.A. 2000, *A&A* **354**, 1001..
Gouiffes, C., Finley, J.P. and Ogelman, H. 1992, *ApJ* **394**, 58.
Gouiffes, C. and Ogelman, H. 2000, Proc. of IAU Coll. N.177 PULSAR ASTRONOMY – 2000 and Beyond.
Gouiffes, C. 1998, Proc. Neutron Stars and Pulsars: 30 years after the discovery Eds. N. Shibazaki, N. Kawai, S. Shibata and T. Kifune, p.363, Universal Academic Press.
Halpern, J.P. and Tytler, D. 1987, *ApJ* **330**, 201.
Hill, R.J. et al. 1997, *ApJ* **486**, L99.
Jacchia, A., DeLuca, F., Lazzaro, E., Caraveo, P.A., Mignani, R. and Bignami, G.F. 1999, *A&A* **347**, 494.
Kaspi, V.M. et al. 2000, Proc. of IAU Coll. N. 177 PULSAR ASTRONOMY – 2000 and Beyond.
Lasker, B. M. 1976, *ApJ* **203**, 193.
Lundqvist, P. et al. 1999, *A&A* **343**, L15.
Martin, C., Halpern, J.P. and Schiminovich, D. 1998, *ApJ* **494**, L211.
Mattox, J.R., Halpern, J.P. and Caraveo, P.A. 1996, *A&A Supp.* 120, 77.
Mattox, J.R., Halpern, J.P. and Caraveo, P.A. 1998, *ApJ* **493**, 891.
Middleditch, J. and Pennypacker, C. 1985, *Nature* **313**, 659.
Mignani, R., Caraveo, P.A. and Bignami, G.F. 1994, *The Messenger* No. **76**, 32.
Mignani, R., Caraveo, P.A. and Bignami, G.F. 1997a, *ApJ* **474**, L51.
Mignani, R., Caraveo, P.A. and Bignami, G.F. 1997b *The Messenger* **87**, 43.
Mignani, R. et al. 1998a, *The Messenger* **94**, 25.
Mignani, R., Caraveo, P.A. and Bignami, G.F. 1998b, *A&A* **332**, L37.
Mignani, R. 1998, Proc. Neutron Stars and Pulsars: 30 years after the discovery Eds. N. Shibazaki, N. Kawai, S. Shibata & T. Kifune, p.335, Universal Academic Press.
Mignani R., Caraveo, P.A. and Bignami, G.F. 1999, *A&A* **343**, L5.
Mignani, R., Pulone, L., Marconi, G., Iannicola, G. and Caraveo, P.A. 2000, *A&A* – in press.
Nasuti, F. P., Mignani, R., Caraveo, P. A. and Bignami, G.F. 1996a, *A&A* 1996, **314**, 849.
Nasuti, F. P., Mignani, R., Caraveo, P.A. and Bignami, G.F. 1996b, *The Messenger* No. **83**, 38.
Nasuti, F.P., Mignani, R., Caraveo, P.A. and Bignami, G.F. 1997a, *A&A* **323**, 839.
Nasuti, F.P., Mignani, R., Caraveo, P.A., and Bignami, G.F. 1997b, *The Messenger* No. **87**, 48.
Ogelman, H. et al. 1989, *ApJ* **342**, L83.
Pacini, F., 1971 *ApJ* **163**, L17.
Pacini, F. and Salvati, M. 1987, *ApJ* **321**, 447.
Pavlov, G.G., Stringfellow, G.S. and Cordova, F.A. 1996, *ApJ* **467**, 370.
Pavlov, G.G., Welty, A.D. and Cordova, F.A., 1997 *ApJ* **489**, L75.
Seward, F. D. and Wang, Z. 1988, *ApJ* **332**, 199.
Shapiro, S. L. and Teukolsky, S.A. 1983, in *Black Holes, White Dwarfs and Neutron Stars*, Eds. Wiley and Sons.
Shearer, A. et al. 1994, *ApJ* **423**, L51.
Shearer, A. et al. 1998, *A&A* **335**, L21.
Wagner, S. and Seifert, W. 2000, Proc. of IAU Coll. N.177 PULSAR ASTRONOMY – 2000 and Beyond.
Wallace, P.T. et al. 1977, *Nature* **266**, 692

The ROSAT Deep Cluster Survey: Probing the Galaxy Cluster Population out to $z = 1.3$

P. ROSATI¹, C. LIDMAN¹, R. DELLA CECA², S. BORGANI³, M. LOMBARDI¹, S.A. STANFORD⁴, P.R. EISENHARDT⁵, G. SQUIRES⁶, R. GIACCONI⁷, C. NORMAN⁷

¹European Southern Observatory; ²Osservatorio Astronomico di Brera, Milano; ³INFN, Sezione di Trieste;

⁴Institute of Geophysics and Planetary Physics, Lawrence Livermore National Laboratory;

⁵Jet Propulsion Laboratory; ⁶California Institute of Technology; ⁷Johns Hopkins University

1. Introduction

The redshift evolution of the space density of galaxy clusters has long served as a valuable tool with which to test models of structure formation and to set constraints on fundamental cosmological parameters. Being recognisable out to large redshifts, clusters are also ideal laboratories to study the evo-

lutionary history of old stellar systems, such as E/SOs, back to early cosmic look-back times. It is therefore not surprising that a considerable observational effort has been devoted over the last decade to the construction of homogeneous samples of clusters over a large redshift baseline. Until a few years ago, however, the difficulty of finding high-redshift clusters in deep optical images

and the limited sensitivity of early X-ray surveys had resulted in only a handful of spectroscopically confirmed clusters at $z > 0.5$. The ROSAT satellite, with its improved sensitivity and spatial resolution, made clusters high-contrast, extended objects in the X-ray sky and has thus allowed for a significant leap forward. About a thousand clusters have now been selected from the ROSAT

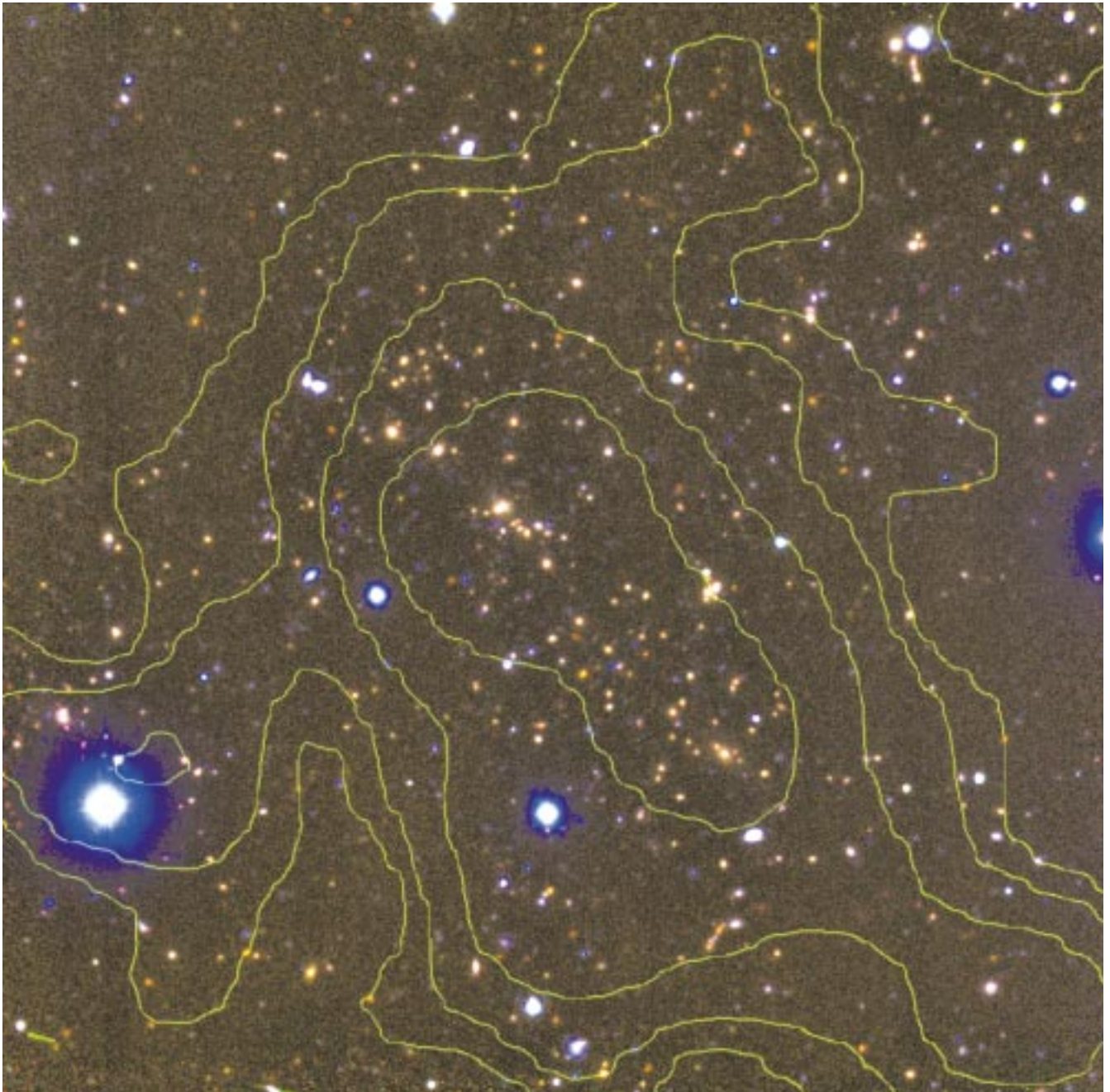


Figure 1: RXJ0152.7-1357 ($z = 0.83$) – one of the most X-ray luminous clusters known at $z > 0.5$. The ROSAT PSPC X-ray contours are overlaid on a (V+R, J, K) composite image obtained with VLT/FORS1 and NTT/SOFI. The field of view is $4.7' \times 4.7'$ (corresponding to $2.3 \text{ Mpc } h_{50}^{-1}$ at $z = 0.83$). The overall morphology of the X-ray emission, and the apparent galaxy distribution, are clearly elongated with two clumps present.

All-Sky Survey at $z \gtrsim 0.3$ and several statistical complete subsamples have been used to obtain a firm measurement of the local abundance of clusters and their spatial distribution (cf. Böhringer et al. 1998). Soon after the ROSAT archive of pointed observations was opened, it was realised that deep PSPC pointings could be used for serendipitous searches for distant clusters.

In this spirit, we embarked in 1994 on the ROSAT Deep Cluster Survey with the aim of constructing a large, X-ray flux-limited sample of distant galaxy clusters. In the period 1995–1998 we engaged in an intense optical identification programme, a substantial fraction of which was carried out with the EFOSC spectrograph at the 3.6-m at La

Silla. Over the last two years, our efforts have shifted to the near IR study of the most distant candidates and, most recently, to spectroscopic follow-up of these systems with the VLT. This observational effort has produced the largest sample of spectroscopically-confirmed distant clusters to date, with four clusters confirmed beyond redshift one. We summarise here some results and highlights from the entire survey.

2. Cluster Selection and the Optical Follow-up Work

The RDCS was designed to compile a purely X-ray selected sample of galaxy clusters, selected via a serendipitous search for extended X-ray

sources in ROSAT-PSPC deep pointed observations (Rosati et al. 1995). The limiting X-ray flux and the solid angle of the survey were chosen to probe an adequate range of X-ray luminosities over a large redshift baseline. Approximately 160 candidates were selected down to the flux limit of $1 \times 10^{-14} \text{ erg s}^{-1} \text{ cm}^{-2}$, over a total area of $\sim 50 \text{ deg}^2$, using a wavelet-based detection technique. This technique is particularly efficient in discriminating between point-like and extended, low surface brightness sources.

Optical follow-up observations of the cluster candidates in both hemispheres consisted primarily of optical imaging in the I-band with 2- and 4-m-class telescopes at NOAO and ESO, followed by

multi-object spectroscopy with 4-m-class telescopes at KPNO and ESO. Candidates were observed in order of decreasing X-ray flux to have a flux-limited sample at any given time. EFOSC at the 3.6-m was used for the identification of the southern and equatorial clusters, and indeed, it proved to be an ideal instrument for this work. Typically, a 10-minute snapshot image was obtained and if a galaxy overdensity was visible around the X-ray peak, a MOS exposure was obtained the following night. Even with the old IHAP system, overheads were relatively small and mask alignment very reliable. This contributed to the overall efficiency of identification, and approximately 60 southern cluster redshifts were secured over 3 years with 20 allocated nights (80% clear). About a quarter of these clusters were confirmed at $z > 0.5$. The highest redshift cluster (RXJ0152.7-1357) was identified with EFOSC1 at $z = 0.83$ (Rosati et al. 1998, Della Ceca et al. 2000). This cluster, shown in Figure 1, is one of the most X-ray luminous known at $z > 0.5$ and possibly also one of the most massive distant systems, perhaps akin to MS1054.4-0321 (Gioia & Luppino 1994).

To date, the entire RDCS sample contains 115 new clusters or groups with secure spectroscopic redshifts, 21 of which lie at $z > 0.6$ and 10 at $z > 0.8$. The redshift distribution is shown in Figure 2 and compared with the EMSS cluster sample, which has been the basis of numerous studies of distant clusters in previous years. The RDCS has clearly considerably extended the high-redshift tail.

The spectroscopic identification is 90% complete to $3 \times 10^{-14} \text{ erg s}^{-1} \text{ cm}^{-2}$; at this limiting flux, the completeness level and the selection function are both well understood. At fainter fluxes, the effective sky coverage progressively decreases and the X-ray surface brightness limit becomes increasingly important. However, it is precisely in this lowest flux bin that the most distant clusters of the survey are expected to lie. To improve the success rate of identifying $z \gtrsim 1$ clusters, we have begun a programme of near-IR imaging of unidentified faint candidates in the RDCS. Near-IR imaging is essential at these large redshifts to compensate the k-correction, which significantly dims the dominant population of early-type cluster galaxies at observed optical wavelengths. A dramatic example of this effect is illustrated in Figure 3. A deep I-band image with a 4-m-class telescope (CTIO 4-m) had not shown any significant galaxy overdensity at the X-ray position. On the other hand, a moderately deep image with SOFI at the NTT (bottom right) clearly revealed a red clump of galaxies with a narrow $J - K$ colour distribution typical of early-type galaxies at $z > 1$ (see the ‘‘yellow clump’’ in the colour composite image). The same

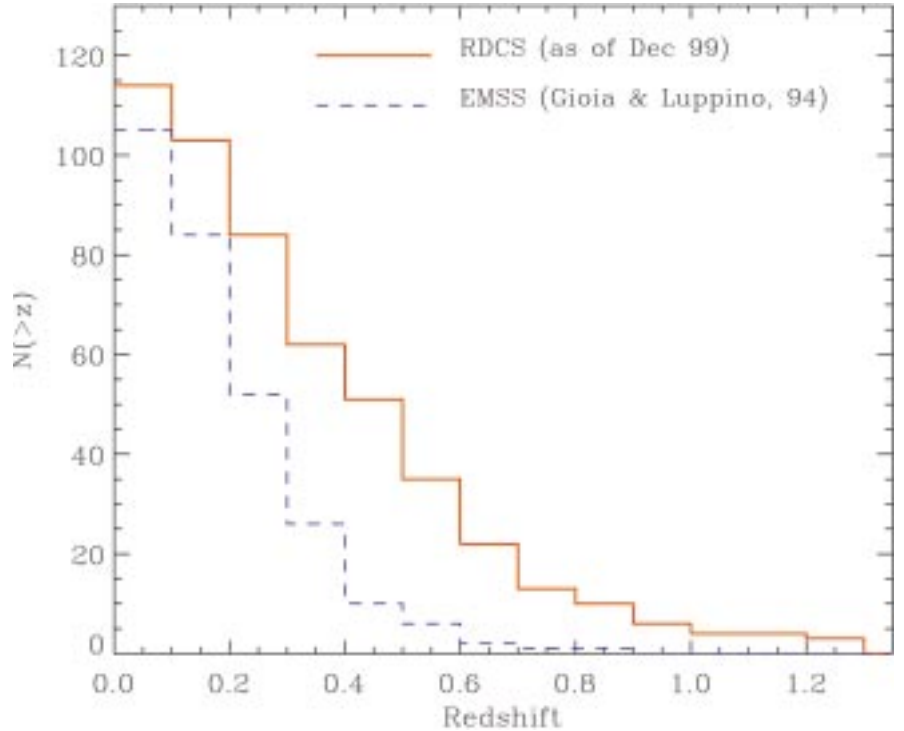


Figure 2: The cumulative redshift distribution of spectroscopically confirmed RDCS clusters to date. For comparison, the distribution of the EMSS sample (Gioia & Luppino, 1994) is shown.

clump is barely visible in a 1-hour R-band exposure with FORS1 (bottom left). Cluster galaxies are fainter than $K = 17$, with colours as red as $R - K = 6$. FORS1 spectroscopy in March 1999 yielded a redshift $z = 1.23$ for the 3 brightest cluster members, and further spectroscopic work is scheduled with FORS1 in March 2000. It is worth emphasising that spectroscopy of early-type galaxies at these redshifts is extremely hard, even with the VLT, requiring no less than 5 hours integration to securely identify a few absorption features (primarily the H+K break) embedded in the OH sky forest. The cluster in Figure 3 is the highest redshift cluster confirmed to date in the southern sky. Three other RDCS clusters in the northern sky were spectroscopically identified with the Keck telescope at $z > 1$ (Stanford et al. 1997, Rosati et al. 1999).

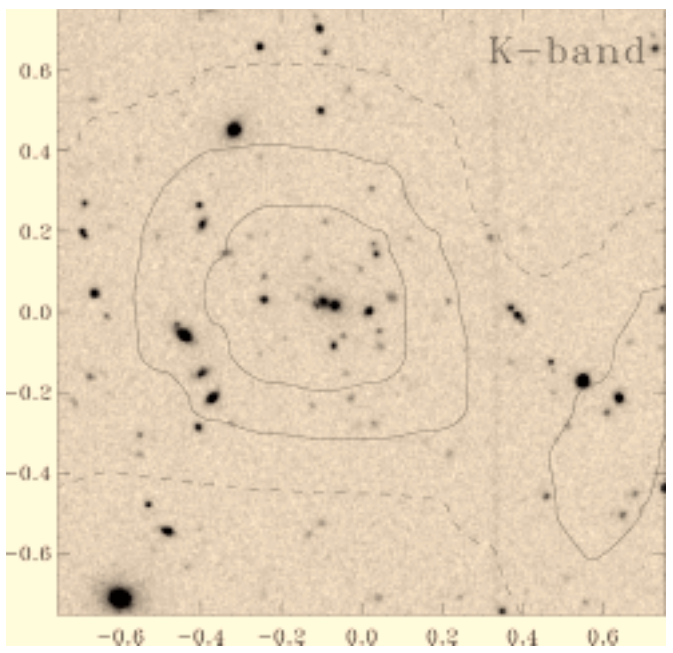
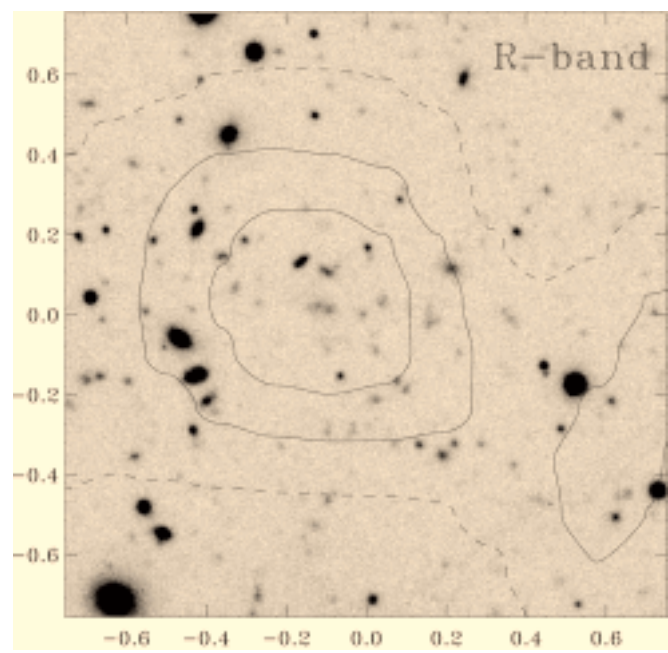
3. Some RDCS Highlights

An immediate advantage of an X-ray selected cluster sample, like the RDCS, is that one can use statistics such as number counts and luminosity functions to quantify the evolution of the cluster population, similar to what is done for galaxy redshift surveys. In Figure 4, we show the X-ray luminosity function (XLF, i.e. the number of clusters per comoving Mpc^3 , per unit X-ray luminosity) of a complete, spectroscopically identified RDCS subsample with a limiting flux of $3.0 \times 10^{-14} \text{ erg s}^{-1} \text{ cm}^{-2}$. This represents the best determination to date of the space density of distant

clusters out to $z \approx 1.2$. A maximum likelihood analysis of the sample confirms the visual impression that there is no significant evolution of the cluster space density out to $z \approx 1$, at luminosities below the local $L^*_X (\approx 4 \times 10^{44} \text{ erg s}^{-1} [0.5\text{--}2 \text{ keV}])$, roughly the Coma cluster). Careful analysis of the bright end of the XLF instead shows some mild negative evolution, i.e. a lack of the most luminous, possibly massive systems ($L_X \gtrsim 4 \times 10^{44} \text{ erg s}^{-1}$) at high redshifts. This result is consistent with the original findings of the EMSS (Gioia et al. 1990), although the strength of the effect is still a matter of some debate (Rosati et al. 1998, 1999).

The identification of the most distant clusters in the RDCS allows an estimate of the cluster abundance to be made for the first time at $z \approx 1$. This is shown in Figure 4 as a lower limit due to the incomplete optical identification at very low flux levels. According to this estimate, there is at least one cluster as luminous as 1/5 of the Coma cluster in $(150h_{50}^{-1})^3 \text{ Mpc}^3$ comoving, at $z \approx 1$.

Figure 3: RJK composite image of the most distant RDCS cluster in the southern sky ($z = 1.23$) obtained combining FORS1 and SOFI images. The field of view is $3.8' \times 3.8'$. Bottom: R-band and K-band image obtained with VLT/FORS1 and NTT/SOFI (1 hour exposure each), with overlaid ROSAT-PSPC contours (scale in arcmin).



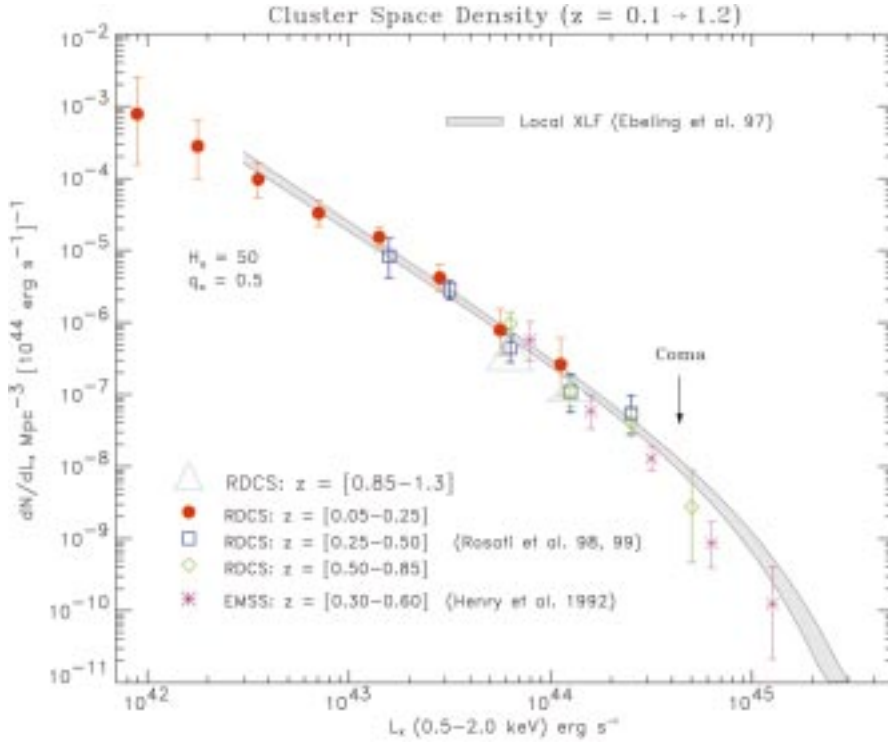


Figure 4: The best determination to date of the cluster X-ray Luminosity Function out to $z \approx 1.2$. Data points at $z < 0.85$ are derived from a complete RDCS sample of 103 clusters over 47 deg^2 , with $F_{\text{lim}} = 3 \times 10^{-14} \text{ erg s}^{-1} \text{ cm}^{-2}$. The triangles represent a lower limit (due to incomplete optical identification) to the cluster space density obtained from a sample of 4 clusters with $\langle z \rangle = 1.1$ and with $F_{\text{lim}} = 1.5 \times 10^{-14} \text{ erg s}^{-1} \text{ cm}^{-2}$.

That the space density of the bulk of the cluster population is approximately constant out to $z \approx 0.8$ has interesting consequences for cosmology. Despite the fact that we are not measuring cluster masses but X-ray luminosities, which depend of the thermodynamical history of the intra-cluster gas in a complicated fashion, it can be shown that significant constraints can be placed on cosmological models within the uncertainties of the $L_X - M$ relation and its evolution (see Fig. 5, Borgani et al. 1999a, 1999b). This analysis shows that it is difficult to reconcile an $\Omega_M = 1$ universe with the RDCS data and our current knowledge of the $L_X - T_X$ relation for distant clusters. The fact that a large fraction of relatively massive clusters is already in place at $z \sim 1$ indicates that the dynamical evolution of structure has proceeded at relatively slow pace since $z \approx 1$, a scenario which fits naturally in a low-density universe.

4. Conclusions

The sheer number of distant clusters spectroscopically identified in the RDCS illustrates the efficiency of the methodology used, as well as the strategy of the optical follow-up observations which were largely carried out with 4-m-class telescopes. By boosting the number of known clusters at $z > 0.5$ by a factor 5, the RDCS provides the basis for several follow-up studies. Some of

these programmes, such as the evolution of the cluster galaxy populations and the cluster mass distribution via lensing and dynamical methods, have already begun with the VLT.

In particular, the spectrophotometric properties of cluster galaxies at $z > 1$ are important diagnostics for constraining the mode and epoch of formation of E/S0 galaxies. The near-IR colours of the reddest members of the RDCS clusters which we have studied so far at $z > 1$ show that these galaxies form a remarkably homogeneous population,

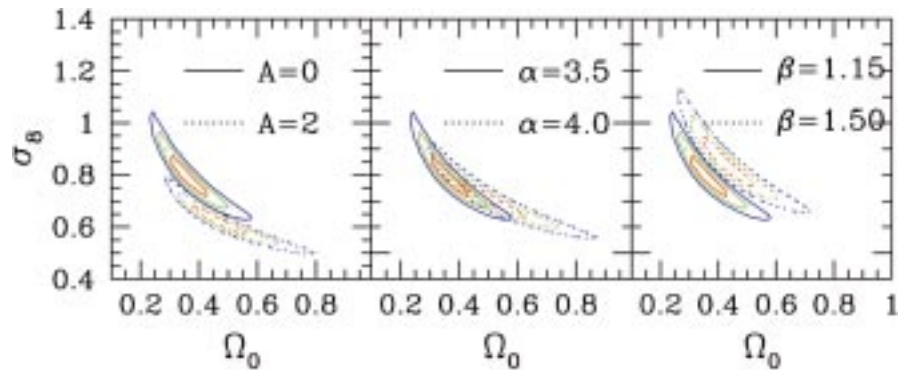


Figure 5: Constraints in the plane of the cosmological parameters Ω_0 (matter density parameter)– σ_8 (rms mass fluctuation on a $8h^{-1} \text{ Mpc}$ scale) derived from the observed evolution of the cluster abundance in the RDCS sample (Borgani et al. 1999a, 1999b). Contours are 1σ , 2σ and 3σ confidence level. The three parameters (A , α , β) describe the uncertainties in converting cluster masses into temperatures ($T \sim M^{2/3} / \beta$), and temperatures into X-ray luminosities ($L_X \sim T^\alpha (1+z)^A$). The two values for each parameter bracket the range which is allowed from current X-ray observations of distant clusters.

a property which is often exploited to constrain the formation scenario of E/S0s (e.g. Stanford et al. 1997). Deep ISAAC imaging would be crucial to investigate the (unknown) faint end of the cluster galaxy population at several magnitudes below L^* , at these high redshifts. The time-consuming spectroscopic work will benefit considerably from the planned upgrade of FORS2 with a red-sensitive CCD, coupled with high-throughput gratings.

Many exciting new observations of these clusters will be made in the near future. Further insight on the physical properties (temperature, metallicity) of the gaseous component of the most distant RDCS clusters will be possible with scheduled Chandra and XMM observations. In addition, significant progress towards our understanding of the formation of the galaxy populations at these large look-back times will come from combining VLT data with planned observations of these clusters with the Advanced Camera on HST (scheduled in 2001).

References

- Böhringer et al. 1998, *The Messenger*, 1998, No. **94**, p. 21.
- Borgani et al. 1999a, *ApJ*, **517**, 40.
- Borgani et al. 1999b, in "Large Scale Structure in the X-ray Universe", eds. M. Plionis & I. Georgantopoulos, Santorini, Greece, September 1999 (astro-ph/9912378).
- Della Ceca et al. 2000, *A&A*, **353**, 498.
- Gioia et al. 1990, *ApJ*, **356**, L35.
- Gioia, I.M. & Luppino, G.A. 1994, *ApJS*, **94**, 583.
- Henry et al. 1992, *ApJ*, **386**, 408.
- Rosati et al. 1995, *ApJ*, **445**, L11.
- Rosati et al. 1998, *ApJ*, **492**, L21.
- Rosati et al. 1999, *AJ*, **118**, 76.
- Rosati et al. 1999, in "Large Scale Structure in the X-ray Universe", eds. M. Plionis & I. Georgantopoulos, Santorini, Greece, September 1999 (astro-ph/0001119).
- Stanford et al. 1997, *ApJ*, **114**, 2232.

Spectral PSF Subtraction I: The SPSF Look-Up-Table Method

P. MØLLER, ESO

Introduction: Why Spectral PSF Subtraction?

The first FORS follow-up run of the STIS/NICMOS survey for Damped Ly α (DLA) galaxies was completed in August 1999. The purpose of the FORS spectroscopy is to search for Ly α emission lines from candidate DLA galaxies with projected distances from the underlying quasars as small as 0.30 arc-sec. The candidate DLA galaxies are typically some 8–10 magnitudes fainter than the underlying quasars.

To be able to look for the faint Ly α emission lines hidden under bright quasar spectra, we shall need a spectral reduction code optimised to subtract the two-dimensional (henceforth 2D) signal of the quasars with extremely high accuracy. By a strike of good fortune, a 1D spectral extraction code was designed several years ago with the specific aim to provide the best possible determination of the Spectral Point Spread Function along the slit. As outlined below there are minor, but important, differences between a 2D imaging PSF and the 1D Spectral PSF. To avoid confusion, we shall in what follows write SPSF for the 1D Spectral PSF.

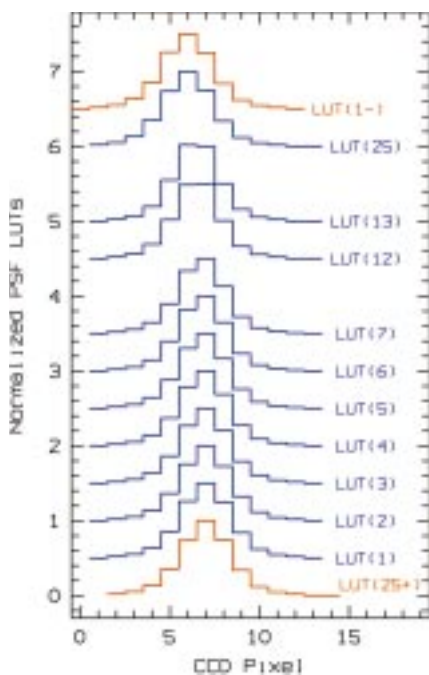


Figure 1: Attempt to represent the Look-Up-Table (LUT) used for the prediction of the Spectral PSF (SPSF) at any wavelength bin of the 2D spectrum. In this example, the increase in sampling (n) is 25 and the length of the SPSF (l) is 13. Each LUT entry (a row in Fig. 1) is a string of 13 numbers making up a single SPSF realisation (see Section 2).

The example presented above, the search for high redshift DLA galaxies, is merely one field in which SPSF subtraction is essential. The technique is potentially extremely useful in any field of astronomy dealing with separation of objects with small projected distances on the sky, or even objects covering each other. In this and in a following issue of *The Messenger* we are going to present three reports aimed at detailing the exact properties of the algorithm to be used for the reduction of our FORS spectra. This first report presents the details of the algorithm itself. The second report (Møller et al., 2000) presents, as a simple example of a research field in which exact SPSF subtraction can provide interesting new results, the serendipitous discovery of extended Ly α emission from the host galaxy of a radio-quiet high-redshift QSO. The third and last report will present the first confirmed identification of an intervening DLA galaxy from the STIS/NICMOS survey.

2. Maximum S/N Extraction of 1D Spectra

When 2D photon-counting detectors were first attached to spectrographs, it was immediately realised that by applying a proper weighting scheme to all pixels of the 2D spectrum, one may optimise the signal-to-noise (the S/N) of the extracted 1D spectrum. Determination of the optimal weights requires knowledge of the SPSF. The more precise guess of the actual SPSF one is able to obtain, the higher the resulting S/N of the extracted 1D spectrum. It is also true, however, that the improvement in S/N when going from a “fairly good SPSF” to the “exact SPSF” will be minor in most cases. Therefore, for the purpose of 1D extraction there is no strong incentive to optimise the model SPSF beyond a certain point. Extraction algorithms not optimised in this sense present no problem as far as the extraction of 1D spectra is concerned, but they will not be adequate for our purposes. This point is of some importance and will be detailed below.

In what follows we shall consider a 2D spectrum which falls roughly along the columns of a CCD. The rows will then (if we for now ignore the 2D distortion in wavelength space) represent bins in wavelength space.

A number of effects complicate the determination of the optimal weights:

- **The SPSF is wavelength dependent.** The seeing is typically better in the red than in the blue. For broadband imaging this means that a blue object will

have a slightly larger PSF than a red object. In spectroscopy, it means that the SPSF will be broad in the blue end, and narrow in the red end of the spectrum.

- **Focus changes along the spectrum.** Most spectrographs are not simultaneously in focus over the entire wavelength range. One therefore has to choose a compromise for the best over-all focus. This may introduce a quite unpredictable change of the SPSF width along the spectrum.

- **The spectrum does not lie exactly along the detector rows (or columns).** Most spectrographs have a distorted spectrum which is “C” or “S” shaped. Hence, the SPSF is typically shifting from one column into several other columns along the way.

The SPSF itself is a continuous and smooth function. However, what we actually observe is a discontinuous step-function induced by the process of observing the continuous function with an array of finite sized pixels. To emphasise the difference (which is extremely important in what follows) we shall refer to the observed step-function as a “realisation” of the SPSF. For a given SPSF, there will be an infinite number of different realisations, all differing by shifts on the detector smaller than a pixel. An example of several different realisations of the same SPSF from a FORS1 spectrum are shown in Figure 1.

Horne (1986) reported on an extremely powerful and simple algorithm that, as long as the spectrum is aligned well with the CCD rows or columns, determines the SPSF realisations along the spectrum with very good accuracy. A generalisation of the Horne algorithm to the case of spectra *not* aligned well with the CCD was found by Marsh (1989). As pointed out above, optimal weights for maximum S/N 1D extraction routines are derived from the SPSF realisations, and that was the goal of the Horne and Marsh algorithms. In the limit of very bright objects, the optimal weights are all identical and equal to 1, for faint objects the SPSF realisations are needed to determine the weights. For very faint sources and for sources with strong absorption features, several additional problems come into play. First of all the SPSF is essentially impossible to determine where there are bright skylines and where there is strong absorption (such as in the Lyman forest of quasar spectra). Hence, some sort of smoothing or fitting algorithm must be used to interpolate between the poorly determined bins. The smoothing (or in the case of the

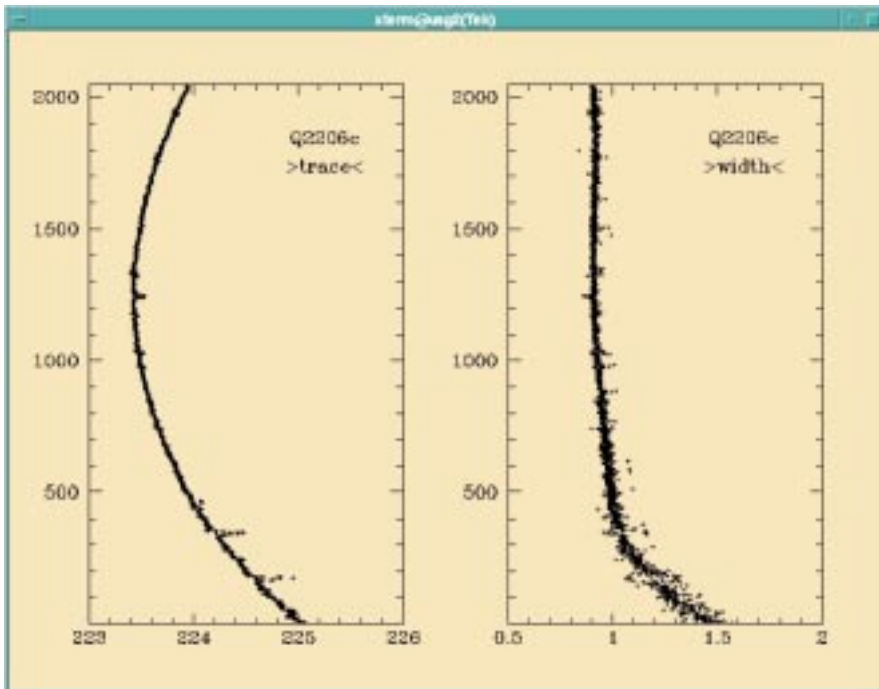


Figure 2: Output of the “trace” and “width” commands. The left frame plots the centroid of the SPSF and covers three CCD columns. The right frame plots the relative width of the SPSF as a function of wavelength (blue is down, red is up). The data are from FORS1/GRISM-600B taken under excellent seeing conditions, but note that we have rotated the FORS data 90 degrees.

Horne algorithm the polynomial fitting) introduces some imperfections in the weights. For the purpose of extracting the 1D spectrum, those imperfections are mostly of no consequence. For the purpose of searching for faint objects hidden under the bright spectrum, there are three specific problems. First, the SPSF determination is *in situ*. This means that the hidden object will be treated by the code as part of the SPSF, and it will be included in the data for the polynomial fitting. A narrow emission line then becomes somewhat harder to detect, a broad emission line will most likely be missed entirely, having been interpreted as a wavelength-dependent change in the SPSF. Second, most codes ignore the extended wings of the SPSF because they contain essentially no information (for the purpose of extracting a 1D spectrum). Fitting to low S/N wings *in situ* would in any case be a fit to mostly random noise. The wings are nevertheless important to remove if one wishes to search for faint extended emission. Third, since the main goal of our project is to search for faint emission in the Lyman forest of high redshift QSOs, we would expect major problems if we were to use the SPSF determined *in situ* on the basis of the few bits of QSO left between the many strong absorption lines in the forest.

All three problems listed above are related to, or made worse by, the fact that the SPSF determination is performed locally in each separate wavelength bin (*in situ*). Hence, the solution is to use a global SPSF determination algorithm. A code based on this principle

was developed and installed at Copenhagen University Observatory in 1989. It has been used only by myself and collaborators, mostly for extraction of quasar spectra but lately also for extraction of faint galaxy spectra of early-type galaxies at intermediate redshifts (Treu et al., 1999). A short summary of the method was given in Møller & Kjærgaard (1992) but details of the algorithm have never previously been published.

The code was developed for the purpose of 1D spectral extraction, but an extra option was included: The possibility to subtract the 2D version of the extracted spectrum. The 2D spectrum-removal option was intended mostly as a check that the algorithm had worked properly. In addition, since the code included “cosmic” rejection via sigma clipping, it provided a possibility to check if cosmics had been overlooked by the code. The 2D-subtraction option has, however, already been successfully applied in the search for DLA galaxies (Møller 1999).

3. The SPSF Look-Up-Table Method

3.1 General Overview: The Four Steps

The algorithm is iterative and based on four simple steps: (i) Trace the spectrum (determine the centroid of the SPSF in each wavelength bin), (ii) determine the width of the SPSF in each wavelength bin, (iii) determine the amplitude of the SPSF in each wavelength bin, (iv) predict the realisation of the SPSF in each wavelength bin.

Figure 2 shows an example of the first two steps, the “centroid trace” and “width” determinations on a FORS1/Grism-600B 2D spectrum. The second and third steps in the above list are in reality performed simultaneously via a two-parameter minimum χ^2 fit as follows. For a given guess of the width, the predicted SPSF realisation is scaled linearly in width, and the best-fitting amplitude is determined. The best global two-parameter fit is found. It is easy to show that minimum χ^2 fitting of an assumed SPSF realisation to the actual data in each wavelength bin is mathematically equivalent to a maximum S/N 1D extraction. After completion of the first three steps, a new and better determination of the SPSF is possible, and a new iteration of the four steps can be performed. When the iterations converge towards a global minimum of the total χ^2 , the process may be stopped and the fitted 2D spectrum subtracted from the input data frame.

The determination of the SPSF realisations is done on basis of the latest “trace”. The trace command determines the centroid of the SPSF with high accuracy in each wavelength bin. The code then subdivides all pixels into n subpixels in the spatial direction (along the slit). Effectively it then builds up an empirical Look-Up-Table (LUT) of n different realisations of the SPSF. Each of those realisations correspond to the subset of rows in the input data frame where the trace command determined that the centroid fell inside the same given sub-pixel. In practical terms, the LUT is an array of $(l \times n)$ numbers where l is the selected length of the SPSF (in CCD pixels) and n is the resolution into sub-pixels which is deemed necessary/possible for the given data. Typically we use $n = 25$, and will do so in the example given below.

3.2 The Core Algorithm: Creating the LUT

The final quality of the 2D spectral subtraction is depending critically upon how carefully the LUT was constructed. The first step of the LUT construction is the summing of all data-rows with the same sub-pixel trace position, which pass a set of additional quality conditions (S/N, no cosmics found in that bin). After the distribution of raw LUT data is completed, all n realisations are normalised. In Figure 1 we show (in blue) the normalised LUT determined from the example FORS spectrum used in Report 2. Clearly, the first entry (named LUT(1) in Figure 1) and the last entry (LUT(25)) are neighbour realisations in the same sense that e.g. LUT(3) and LUT(4) are, except that they are shifted by a full CCD pixel along the slit. This is exemplified by the two realisations reproduced in red in Figure 1. E.g. LUT(25+) is identical to LUT(25) but shifted by one pixel. As the

last step in the LUT construction algorithm, this process of expanding the 2D LUT by “adding on” shifted 1D LUT realisations is repeated ($l \times n$) times. By selection of the column corresponding to the leftmost pixel of LUT(1), the code obtains a single string of the ($l \times n$) numbers making up the complete LUT. This string of numbers hence contain the entire LUT, only now re-ordered in a way so that it is a single smooth and continuous function. This function corresponds to the input SPSF at n times improved sampling, but still containing the observationally induced CCD pixel smoothing.

It can be seen that if a single, or a few, of the individual entries in the 2D LUT grid are missing (by unfortunate locations of cosmics, sky-lines and absorption lines), then a whole row will be missing in the 2D LUT grid. In the continuous high-resolution representation of the LUT, however, a missing entry will only result in a set of single missing values at each 25th sub-pixel. Those can easily be determined via interpolation between good values. After interpolation to determine unknown values, possibly some smoothing if the spectrum in general has low S/N, the process is reversed, and the 2D LUT is reconstructed from the interpolated/smoothed high-resolution representation. This is the last step of a given iteration. If another iteration is started, the new LUT will be used.

4. Degeneracy of Results and Concluding Remarks

We have presented an algorithm that is specifically aimed at performing the best possible removal of a 2D spectrum to reveal faint emission-line objects “hidden” under a bright spectrum. A few notes should be added. **First:** As detailed in Section 2, an algorithm with this goal has to use a global approach to the determination of the SPSF. A global approach is clearly incompatible with the fact that the SPSF varies along the spectrum; some additional assumption is required. In the code described here, we have assumed that the SPSF at any wavelength can be obtained via a linear scaling in width of the same base SPSF. **Second:** Clearly, if two point sources are super-imposed at exactly the same position, there is no way the code can tell that there are in fact two different objects. It will regard the summed spectrum as that of a single point source. **Third:** If the emission-line object is not a point source, and if it extends across the bright point source, the code will try (as a default) to assign as much flux as possible to the point source. This means that part of the emission-line object will be assigned to the spectrum of the bright point source, and the code will “dig a hole” in the extended object at the position of the bright point source. In both of those two cases, there is hence a certain degeneracy

in the final solution as to how much flux should be assigned to the two objects. This degeneracy can be broken in several ways. Typically, one may assume that either the spectrum of the point source is smooth and continuous in the given spectral region, or one may assume that the extended object has a smooth and continuous surface brightness distribution at the position of the bright point source. In the case of two compact and well separated objects no additional assumptions are needed, the solution will be unique.

Acknowledgements

I wish to thank Michael I. Andersen who supplied the routines that perform the optimal fitting of Chebyshev polynomials, and Sandra Savaglio who provided extensive comments on several other functionalities of this data-reduction tool. I am grateful to Keith Horne for many useful comments on an earlier version of this report.

References

- Horne, K., 1986, *PASP*, **118**, 609.
 Marsh, T.R., 1989, *PASP*, **101**, 1032.
 Møller, P., Kjærgaard, P., 1992, *A&A*, **258**, 234.
 Møller, P., 1999, in *Astrophysics with the NOT*, Karttunen, H. and Pirola, V. (eds.), University of Turku, p. 80-88.
 Møller, P., et al., 2000, *The Messenger*, **99**, 33.
 Treu, T., Stiavelli, M., Casertano, S., Møller, P., Bertin, G., 1999, *MNRAS*, **308**, 1037.

SPSF Subtraction II: The Extended Ly α Emission of a Radio Quiet QSO

P. MØLLER¹, S.J. WARREN², S.M. FALL³, P. JAKOBSEN⁴, J.U. FYNBO⁵

¹ESO, Karl-Schwarzschild-Str. 2, Garching, Germany

²Blackett Laboratory, Imperial College of Science, Technology and Medicine, London, UK

³Space Telescope Science Institute, Baltimore, USA

⁴Astrophysics Division, Space Science Department of ESA, ESTEC, Noordwijk, The Netherlands

⁵Institute of Physics and Astronomy, University of Århus, Århus, Denmark

1. Introduction

A common trait of high-redshift radio galaxies is their extended Ly α emission. This emission-line nebulosity is generally aligned with the radio axis, and similar emission has been reported around radio-loud QSOs (Schneider et al. 1987, Heckman et al. 1991a,b, Hu et al. 1991). For radio-quiet QSOs, it appears that extended Ly α emission is much less common. Hu et al. (1991) found extended emission-line nebulosity around three of ten radio-loud QSOs, but from none of the seven radio-quiet QSOs in their sample. Steidel et al. (1991) and Bergeron et al. (1999) reported the detection of extended Ly α emission from two radio-weak QSOs,

and Bremer et al. (1992) reported the so far only detection of extended Ly α emission from a radio-quiet QSO.

Two methods have been used in all of the work quoted above, narrow-band imaging and direct inspection of two-dimensional (2D) CCD spectra to look for regions of emission extending away from the spectrum of the QSO. A tool that would allow modelling and subtraction of the 2D spectrum of the QSO would not only improve the chances of detecting faint emission lines in the vicinity of the QSO, it could also allow more detailed analysis. Our first report on spectral PSF (SPSF) subtraction (Møller, 2000) described a technique for SPSF subtraction. In this second report, as a simple example of an application

of the tool, we report the serendipitous discovery of extended Ly α emission from the host galaxy of the radio quiet $z = 2.559$ QSO Q2206-199.

2. Observations

On August 12, 1999, we obtained four FORS1/Grism 600B long slit spectra, each of 2000 sec integration time, of the radio quiet QSO Q2206-199. Our observing strategy was to obtain several spectra with different offsets along the slit, to minimise the effects of flat-field errors and other systematic effects. This is a crucial point to keep in mind when one is in search of extremely faint features close to, or on top of, a much brighter object.

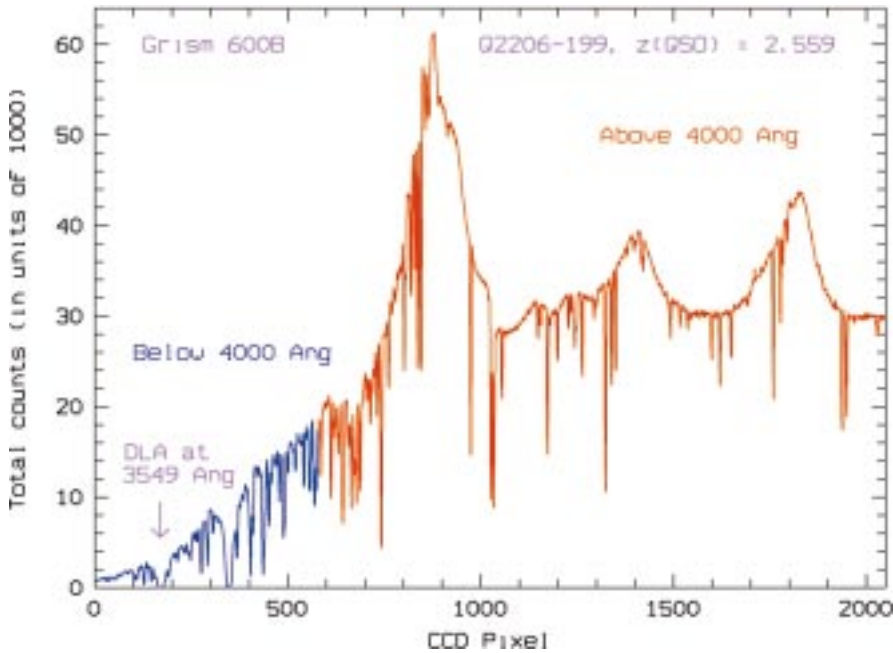


Figure 1: FORS1/600B raw extracted spectrum (8000 seconds) of the $z = 2.559$ radio quiet QSO Q2206-199.

The spectra were obtained with a PA of 236 deg. and the seeing from the automatic seeing monitor (the DIMM) during all exposures was recorded as 0.40–0.45 arcsec. After flat-fielding, shifting and co-addition of the four individual spectra, the measured combined FWHM of the QSO SPSF along the slit is 0.60 arcsec, which is an acceptable degradation of the SPSF as compared to the imaging PSF.

Following the co-addition we used the code described in Report 1 to perform the tracing of the spectrum, to determine the SPSF as a function of wavelength, and to extract the maximum signal-to-noise spectrum of the QSO. In Figure 1, we present the extracted spectrum. The vertical scale is total CCD counts per bin (the ADU conversion is 1.48 e⁻/count). The spectrum is clearly of very high S/N in the region above 4000 Angstrom (red part of the spectrum in Fig. 1), but below 4000 Angstrom (blue part), the combined instrument efficiency drops rapidly. Our target DLA system (at 3549 Angstrom) is deep into the low efficiency part of the spectrum, but despite the low efficiency, we obtained a very clear detection of Ly α emission from the DLA galaxy (to be reported in our third and last SPSF report).

3. Application of SPSF Subtraction: QSO Host Galaxies

The search for the host galaxies of QSOs and the interpretation of their spectral energy distributions has recently started to move from low ($z = 0.1$ – 0.3) towards higher ($z = 2$ – 3) redshifts, and has become a topic of current debate (Terlevich and Boyle 1993, Aretxaga et al. 1998, Fynbo, Burud and Møller 2000). A proposal as to how one

may detect extended line emission across QSO spectra was recently presented by Courbin et al. 1999. Spectroscopic detection of emission lines from the QSO host galaxies would be an important step forward, as it would clarify many of the current questions concerning the high redshift QSOs and their host galaxies.

1. **Is the redshift of the host galaxy the same as that of the QSO broad Ly α and CIV lines?** It has long been known that the QSO high ionisation lines are significantly blue shifted with respect to the low ionisation lines. The low ionisation lines are expected to represent the true systemic redshift of the QSO (Espey et al. 1989, Corbin 1990, Møller, Warren and Fynbo 1998). Emission lines from the host galaxy

should be found at the systemic redshift, hence they should be redshifted from the broad Ly α and CIV of the QSO.

2. **What is the velocity width of the extended line emission?** If the emission from the QSO host galaxy is in reality caused by simple dust reflection (see e.g. Fynbo, Burud and Møller 2000) of the QSO spectrum, such as has been reported for radio galaxies, then the host galaxy spectrum must have both Ly α redshift and line velocity widths identical to that of the QSO itself. If that is not the case then one can rule out the dust-reflection hypothesis.

3. **What is the dynamical mass of the QSO host galaxy?** If the extended line emission is not due to reflected QSO light, then the velocity profile over the spatial extent of the line emission reflects the dynamical state of the emitting gas. It may even be possible to determine a rotation curve. This could provide limits on the mass of the dark matter halos in which the high redshift quasars form.

Data of the quality shown in Figure 1 with high S/N at Ly α , excellent seeing and good sampling of the SPSF, clearly provide the best possible conditions to address those questions. In Figure 2 we show (left panel) a section of the 2D QSO spectrum centred on the Ly α emission line of the QSO. After maximum S/N extraction of the 1D spectrum as described above, we subtracted the minimum χ^2 fit of the 2D spectrum. For illustration purposes, we have (central panel of Fig. 2) only subtracted the central part of the fitted QSO spectrum. The residuals clearly show evidence for extended Ly α emission. The rightmost panel of Figure 2 shows the residuals after the PSF subtraction and after simple box-car smoothing to enhance the contrast of the extended emission over the background noise.

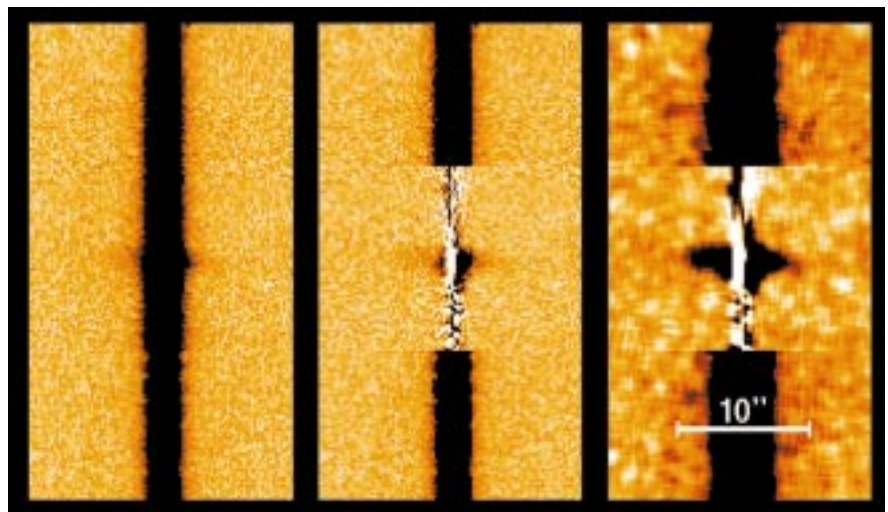


Figure 2: 2D spectrum covering the region around Ly α . **Left:** 2D spectrum after sky subtraction. **Centre:** 2D spectrum after sky subtraction and subtraction of the minimum χ^2 fit of the central part of the 2D QSO spectrum. **Right:** Same as the spectrum in the centre but after simple box-car smoothing to enhance the contrast of the extended emission over the background noise. The horizontal scale (along the slit) in all three panels is 0.2 arcsec per pixel.

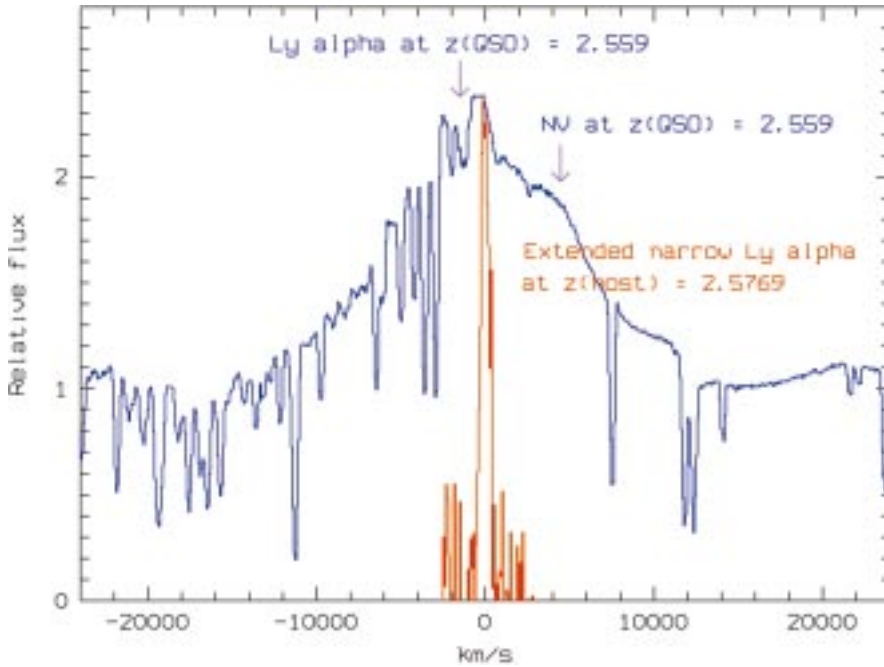


Figure 3: **Blue:** Spectrum of the Ly α line region of the QSO Q2206-199 normalised to 1 in the continuum. **Red:** Spectrum of the extended Ly α line of the host galaxy of Q2206-199. Note that the extended Ly α is much narrower than the QSO Ly α , and that the QSO emission-line redshift is blue shifted by 1500 km/s. The extended Ly α amplitude was scaled arbitrarily for easy comparison to the QSO spectrum.

Clearly, we detect extended Ly α emission over a region of almost 10 arcsec (roughly $50 h^{-1}$ kpc), and the three questions asked above can now be addressed.

4. Extended Ly α of a High-Redshift QSO Host Galaxy

The CCD columns very close to the central part of the 2D spectrum show large residuals at all wavelength bins. This is due to the large photon shot-noise. Faint objects cannot ever be detected close to the central part of the QSO SPSF because of this. To obtain the spectrum of the extended host galaxy we therefore ignored the central noisy

columns, and averaged the regions left and right of the residuals of the middle frame of Figure 2. This spectrum is plotted in red in Figure 3. Also in Figure 3, we have plotted the normalised spectrum of the broad Ly α and NV lines of the QSO Q2206-199. The expected position of the quasar emission lines (for $z_{\text{QSO}} = 2.559$) are marked in Figure 3. The emission redshift of Q2206-199 is taken from the literature and is based on the Ly α , SiIV, and CIV emission lines.

It is immediately clear that the broad lines of the QSO are blue shifted by 1500 km/s with respect to the extended Ly α , and also that the extended Ly α is much narrower than the broad QSO Ly α line. Those two observations confirm that the extended Ly α is indeed at the systemic redshift of the QSO and must be the signature of gas in the host galaxy. It is not caused by dust reflection of quasar light. The FWHM of the narrow Ly α is 760 km/s (at PA 236 deg E of N) and 510 km/s (at PA 56 deg E of N). It is interesting to

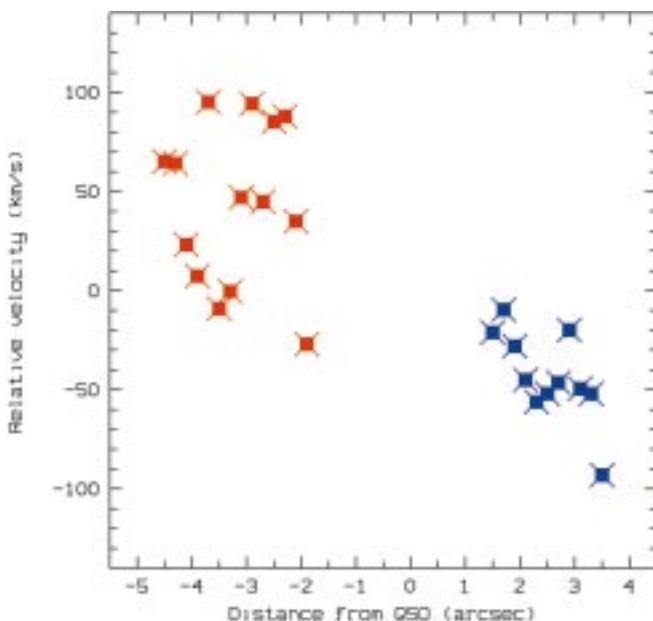


Figure 4: Relative projected motion of the host galaxy gas. The data clearly indicate rotation.

note that there is no hint of Ly α absorption at the redshift of the host galaxy.

From visual inspection of Figure 2 (right frame) it appears that the extended Ly α cloud is rotating. We shall now quantify this observation. For each CCD column where the extended Ly α was strong enough, we fitted a gaussian to the velocity profile. Also here, we ignored the noise-dominated columns close to the central part of the QSO spectrum. The centroids of the velocity profiles, as a function of the projected distance from the QSO, are plotted in Figure 4. It is clear from Figure 4 that the host galaxy gas is indeed rotating. With only a single slit orientation, we cannot know if we are on the major or minor axis of the host galaxy or somewhere in between, and we also do not know what the inclination angle of the galaxy is. Hence, the apparent rotation velocity of about $50\text{--}100 \text{ km/s}$ at a projected radius of about $25 h^{-1}$ kpc, is a lower limit, which places a lower limit of a few times $10^{10} h^{-1}$ Solar masses on the dynamical mass inside this radius. The most striking result from Figure 4 is, however, that the rotation velocity appears to keep growing outwards. Hence, there is likely a significant amount of mass located at even larger distances from the central QSO. This would support the view that QSOs at high redshifts are formed in deep potential wells.

Acknowledgements

Based on observations collected at the European Southern Observatory, Paranal, Chile (ESO Programme 63.0-0618).

References

- Aretxaga I., Terlevich R.J., Boyle B.J., 1998, *MNRAS* **296**, 643.
- Bergeron, J., Petitjean, P., Cristiani, S., Arnouts, S., Bresolin, F., Fasano, G., 1999, *A&A* **343**, L40.
- Bremer M.N., Fabian A.C., Sargent W.L.W., Steidel C.C., Boksenberg A., Johnstone R.M., 1992, *MNRAS* **258**, L23.
- Corbin, M.R., 1990, *ApJ*, **357**, 346.
- Courbin, F., Magain, P., Sohy, S., Lidman, C., Meylan, G., 1999, *The Messenger*, **97**, 26.
- Espey, B.R., Carswell, R.F., Bailey, J.A., Smith, M.G., Ward, M.J., 1989, *ApJ*, **342**, 666.
- Fynbo, J.U., Burud, I., Møller, P., 2000, *A&A*, submitted.
- Heckman T.M., Lehnert M.D., van Breugel W., Miley G.K., 1991a, *ApJ* **370**, 78.
- Heckman T.M., Lehnert M.D., Miley G.K., van Breugel W., 1991b, *ApJ* **381**, 373.
- Hu E.M., Songaila A., Cowie L.L., Stockton A., 1991, *ApJ* **368**, 28.
- Møller, P., Warren, S.J., Fynbo, J.U., 1998, *A&A*, **330**, 19.
- Møller, P., 2000, *The Messenger*, **99**, 31.
- Schneider D.P., Gunn J.E., Turner E.L., Lawrence C.R., Schmidt M., Burke B.F., 1987, *AJ* **94**, 12.
- Steidel C.C., Sargent W.L.W., Dickinson M., 1991, *AJ* **101**, 1187.
- Terlevich R.J., Boyle B.J., 1993, *MNRAS* **262**, 491.

The Late Phase of SN 1998bw

B. LEIBUNDGUT¹, J. SOLLERMAN^{1,2}, C. KOZMA², C. FRANSSON², P. LUNDQVIST²,
F. RYDE², P. WOUDT¹

¹ESO, ²Stockholm University

SN 1998bw is of exceptional interest. The time and position coincidence between the explosion of the SN and the explosion of GRB 980435 makes it likely that the two phenomena are related. The SN evolution has been extensively studied first with the 3.6-m/EFOSC2 during the first year, then was monitored with the VLT/FORS1 during the second year when the object became fainter than $m_V = 21$.

We report here on the late phase of SN 1998bw.

1. Introduction

Some supernovae are special. Supernova SN 1998bw was discovered when the optical counterpart of the γ -ray burst GRB980425 was sought in the BeppoSax error box. It became one of the most luminous stellar explosions ever observed in the optical (Galama et al. 1998), the brightest radio supernova at a time when most other supernovae are still deeply enshrouded in an ionised cocoon which blocks all radio emission (Kulkarni et al. 1998), and the temporal and positional coincidence make a connection to the γ -ray burst itself very likely (Galama et al. 1998). But SN 1998bw was peculiar in several other aspects as well. The spectrum looked different from any other known supernova and defied a clear classification for some time. Due to the lack of obvious hydrogen, helium or silicon lines near maximum light, each of these indicate a Type II, a Type Ib, and a Type Ia supernova, respectively, it was finally assigned a Type Ic classification.

The many deviations from known supernovae and the probable connection with the γ -ray burst triggered a substantial interest in SN 1998bw. It has been called the ‘Rosetta stone’ of γ -ray bursts and a detailed understanding of this explosion could provide insights into the nature of relatively close-by GRBs (the recession velocity of the parent galaxy is only 2550 km s^{-1}). The collapse of the core and subsequent explosion of massive stars had been proposed for GRBs before SN 1998bw (e.g. Woosley 1993). Supernovae from stars which have lost their hydrogen and even helium envelope can come from either massive stars which shed their upper layers in stellar winds (e.g. Wolf-Rayet stars) or binary stars which undergo a common envelope phase in which one star is stripped to the core. The connection of the γ -ray burst and the supernova explosion can be studied in detail for SN 1998bw.

The peculiarity of SN 1998bw was recognised almost immediately at ESO, and a dedicated follow-up programme

initiated. These data map the evolution during the first observing season extensively and will appear soon (Patat et al. 2000). Here we present the data of a smaller programme that also monitored SN 1998bw into the second year. The main reason for the interest at these epochs is in the possibility to directly study the nucleosynthesis and the hydrodynamic properties of the explosion.

2. Observations

We followed the spectral and photometric evolution of SN 1998bw with the 3.6-m/EFOSC2 and UT1/FORS1 from 33 days until 504 days after the outburst (Sollerman et al. 2000). The decrease in brightness can be appreciated in Figure 1 where the images from the 3.6-m from 33 days and from UT1 414 days after explosion are shown. The supernova faded from $V = 14.7$ to $V = 21.7$ over the year. The FORS1 image shows the supernova also superposed on an HII region which makes the photometry at late phases very difficult.

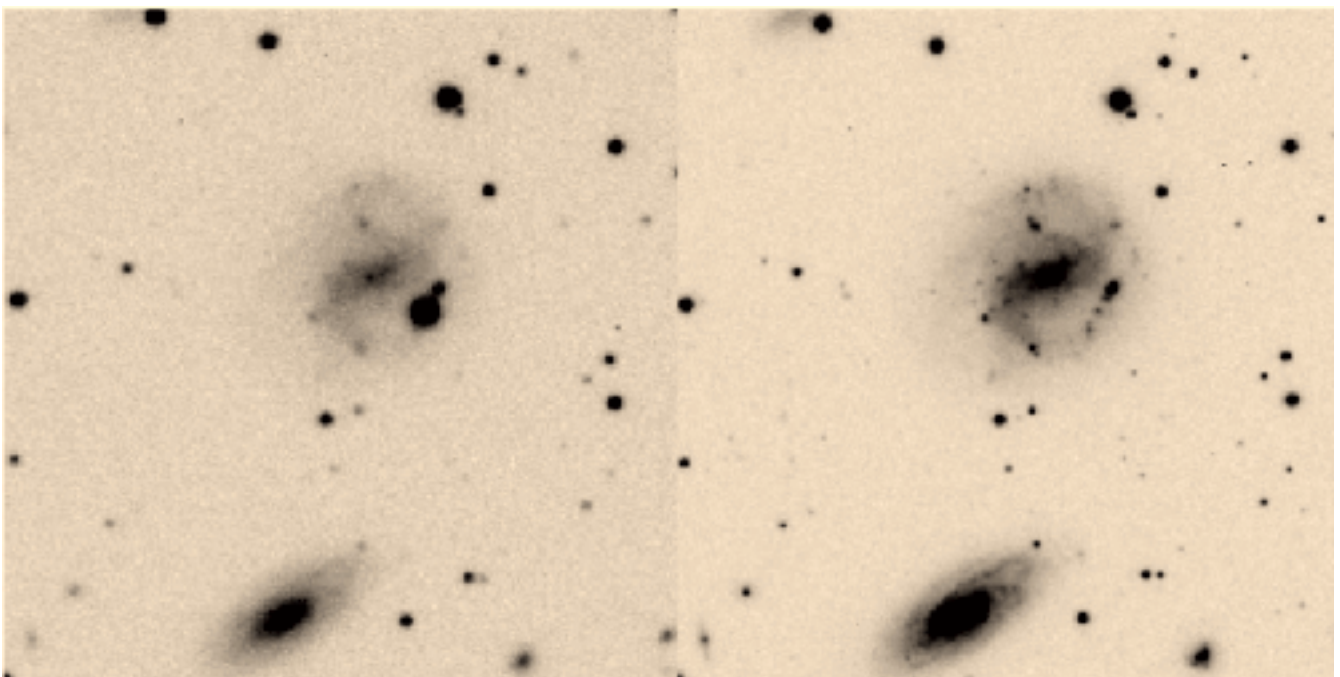


Figure 1: SN 1998bw in May 1998 (3.6-m with EFOSC2; left panel) and June 1999 (UT1 with FORS1; right panel). The supernova is superposed on a faint HII region.

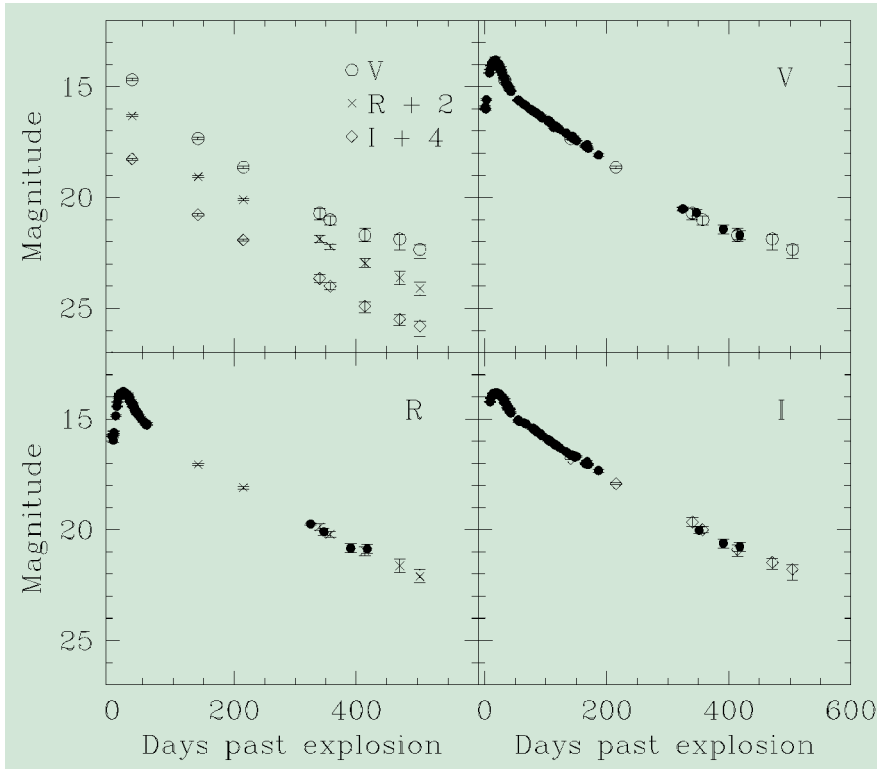


Figure 2: The V, R and I light curves of SN 1998bw. Our photometry (Sollerman et al. 2000) is plotted in the upper left panel. The other panels also include data from Galama et al. (1998; days 1–57), McKenzie & Schaefer (1999; days 63–187), and Patat et al. (2000; days 324–417).

The light curve of SN 1998bw shows an exponential decline in luminosity from about 50 to 400 days after explosion in V, R and I (Fig. 2). Only the last few points after 500 days start to show a deviation from this decline. A slight flattening of the light curve can be perceived at this epoch. We believe that the uncertainties in the background subtraction are not entirely responsible for this flattening and the supernova may be entering a new phase of its evolution.

The spectroscopic evolution of SN 1998bw is displayed in Figure 3. At early times, only very broad and not-well defined features can be seen. The lack of sharp lines is an indication of the high velocities in the ejecta and blending of many lines (e.g. Iwamoto et al. 1998). At late phases the regular features of Type Ib/c supernovae in their nebular phase, i.e. once the supernova ejecta have become optically thin, are observed. The familiar emission lines of Mg I] (λ 4571Å) or [Fe III], [Na I] (λ 5890, 5896Å), [O I] (λ 6300, 6364Å), [O II] (λ 7320, 7330Å), [Ca II] (λ 7292, 7324Å), and the Ca II IR triplet (λ 8498, 8542, 8662Å) are all present and change little in shape, but fade away continuously.

A slight narrowing of the emission lines with time can be observed. Of interest is further the blue continuum below 5500Å which is likely to be due to many blended Fe II and Fe III transitions. The narrow lines of H α , H β , [O III], and [S II] are from the underlying HII region.

The late-epoch spectroscopy hence confirms that SN 1998bw indeed comes from a massive star that has lost its envelope and we can observe the exposed core of the progenitor.

3. Interpretation

The large luminosity and the high velocities in the ejecta have been interpreted as due to an extremely powerful

explosion (Iwamoto et al. 1998, Woosley et al. 1999) of carbon-oxygen stars of 6 to 13 M_{\odot} (note that this is the mass at explosion and not the main-sequence mass which is more than about 40 M_{\odot}) and the production of about 0.5 to 0.7 M_{\odot} of ^{56}Ni . This ^{56}Ni mass is about 5 to 10 times higher than what is observed in other core-collapse supernovae. Other interpretations have proposed asymmetric explosions (Höflich et al. 1999) with less nickel synthesised in the explosion. We have modelled the light curve at late epochs and find that a large amount of nickel is indeed required to sustain the observed luminosity. Since asymmetries play a minor role at late phases, this measurement argues for a Ni mass around 0.7 M_{\odot} , within a factor of two.

The late-phase spectrum shows rather high velocities still, at least 10,000 km s $^{-1}$. Models based on the massive explosions proposed to fit the early spectrum and light curve do not fare too well at these late phases. Strong macroscopic mixing has to be applied to the models to obtain the rather peaked line shapes observed. Without the mixing, the lines would basically trace the mass shells in the ejecta and with a stratified composition, they would produce flat-topped line shapes. But the models also predict velocities that are too high to fit the observations.

Since the energy input into the ejecta is down-scattering of the γ -rays coming from the decay of ^{56}Co , the daughter nucleus of the original ^{56}Ni , it depends directly on the column density of matter in the ejecta. The optical depth to γ -rays is proportional to M_{ej}/v_{exp}^2 . A higher expansion velocity will thin out the ejecta faster, produce a steeper

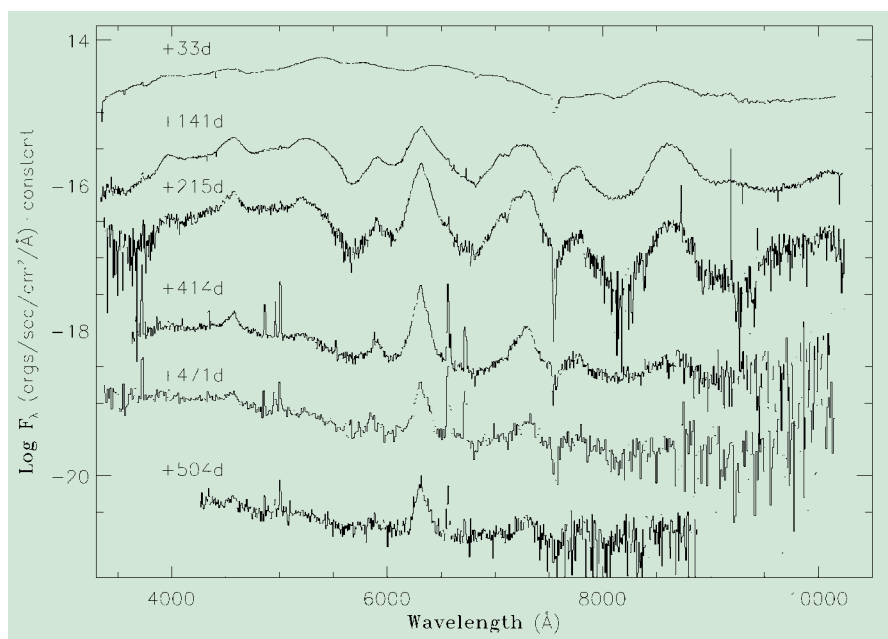


Figure 3: Spectral evolution of SN1998bw. For clarity, the spectra have been shifted by a constant factor. The wavelength scale has been corrected for the velocity of the parent galaxy (2550 km s $^{-1}$).

slope of the light curves, and hence require more nickel to power the late light curve. Decreasing the velocity boosts the late luminosity, and can reproduce the observed line shapes. However, these velocities were not predicted by the models that fit the early spectrum and light curve.

4. Conclusions

The monitoring of SN 1998bw through its second year has provided important new clues on the nature of this object. The late spectrum very much resembles the ones of other Type Ib/c supernovae. Hence, SN 1998bw can be tied to a class of objects we know fairly well. We confirm the large nickel mass required to power the optical radiation of this event, but find discrepancies by fitting the late spectrum with the models which were used to interpret the early phases. The implied energies are still unique for any supernova ever observed.

The connection of SN 1998bw to GRB980425 is still unclear, but we do not expect to see any signature of the burst at these late phases. The radio observations have been linked to the γ -ray burst and the relativistic expansion of material (Kulkarni et al. 1998, Li & Chevalier 1999). The X-ray emission from the GRB afterglow is coincident with the supernova as well (Pian et al. 1999). SN 1998bw remains a fascinating and puzzling object.

The combination of two instruments and telescopes to follow SN 1998bw to late phases has been very useful. The 3.6-m/EFOSC2 provided the early coverage and only at the end was the supernova 'handed' to UT1/FORS1. We were therefore able to secure a spectrum about every month and could follow this object further than would have been possible with the 3.6-m.

It is unlikely that there will be a third observing season for SN 1998bw. Unless the luminosity becomes constant, it will be too faint to be recovered.

There are known processes that could lead to such a constant flux, e.g. interaction with the circumstellar material or input from the accretion on a black hole. We have been following several such objects already and SN 1998bw will be worth at least a check in the next few months.

References

- Galama, T.J., et al. 1998, *Nature*, **395**, 670.
Höflich, P., Wheeler, J. C., & Wang, L. 1999, *ApJ*, **521**, 179.
Iwamoto, K., et al. 1998, *Nature*, **395**, 672.
Kulkarni, S.R., et al. 1998, *Nature*, **395**, 663.
McKenzie, E. H. & Schaefer, B.E. 1999, *PASP*, **111**, 964.
Li, Z.-Y. & Chevalier, R.A. 1999, *ApJ*, **526**, 716.
Patat, F., et al. 2000, in preparation.
Pian, E., et al. 1999, *A&ASS*, 138, 463.
Sollerman, J., et al. 2000, *ApJ*, submitted.
Woosley, S.E. 1993, *ApJ*, **405**, 273.
Woosley, S. E., Eastman, R.G., & Schmidt, B.P. 1999, *ApJ*, **516**, 788.

MISTRAL: Myopic Deconvolution Method Applied to ADONIS and to Simulated VLT-NAOS Images

Jean-Marc Conan¹, Thierry Fusco¹, Laurent M. Mugnier¹, Franck Marchis²

¹ONERA, Département d'Optique Théorique et Appliquée, France ([name](mailto:{name}@onera.fr)@onera.fr);

²ESO, Santiago, Chile (fmarchis@eso.org)

1. Introduction

The performance of high-resolution imaging with large astronomical telescopes is severely limited by the atmospheric turbulence. Adaptive optics [1, 2, 3] (AO) offers a real-time compensation of the turbulence. The correction is however only partial [2, 4, 5, 6, 7] and the long-exposure images must be deconvolved to restore the fine details of the object.

Great care must be taken in the deconvolution process if one wants to obtain a reliable restoration with good photometric precision. Two aspects add to the difficulty: the fact that the residual point spread function (PSF) is usually not perfectly known [8, 9, 10], and the fact that astronomical objects are usually a mix of sharp structures and smooth areas. "MISTRAL" (Myopic Iterative STep Preserving ALgorithm) [11, 8] has been developed to account for these two points. It is based on a rigorous Bayesian approach which allows us to easily account for the noise in the image, the imprecise knowledge of the PSF, and the available *a priori* information on the object (spatial structure, positivity...). A specific edge preserving object prior is proposed, which is in particular well adapted for planetary-like objects.

The notion of AO partial correction is first discussed in Section 2. The principle of our deconvolution technique is briefly summarised in Section 3. In Section 4, the photometric accuracy of MISTRAL is first demonstrated on simulated AO images. The simulation parameters correspond to NAOS, the AO system of the VLT. MISTRAL is then applied to ADONIS images of Io taken at thermal wavelengths using the COMIC camera. This allows an accurate mapping of Io's surface volcanic activity. We also used our deconvolution method on broadband filter (J, H, K) images of Uranus taken with SHARP-II+. The structures of the rings and its innermost satellites have been successfully detected.

2. Partially Corrected AO Images

Within the isoplanatic angle, the intensity $i(r)$ at the focal plane of the system consisting of the atmosphere, of the telescope and of the AO bench is given by:

$$\mathbf{i}(r) = \mathbf{h}(r) * \mathbf{o}(r) + \mathbf{n}(r), \quad (1)$$

where r is the spatial coordinate, $\mathbf{o}(r)$ is the observed object, $\mathbf{h}(r)$ is the system PSF and $\mathbf{n}(r)$ is an additive zero mean noise.

We consider here the case of AO corrected long exposure images. Such an image is presented in Figure 1. In this numerical simulation, we considered an 11th magnitude planetary-like object observed in the visible with the NAOS AO system [12] installed on the VLT. This system will provide high performance in the near IR ($SR \approx 70\%$ at high flux). Here we consider the case of observations at visible wavelength ($\lambda = 0.5 \mu\text{m}$). In such conditions, the image blur is very severe, the expected SR is only 2.1% for a 0.73 arcsec seeing. Neither the fine structures on the surface of the object, nor the stars in the background are apparent in the corrected image. A deconvolution is therefore required.

The deconvolution procedure needs a measurement of the PSF. The usual procedure consists in recording the corrected image of a nearby unresolved star shortly after observing the object of interest. Since the correction quality depends on the observing conditions (turbulence strength, magnitude of the source used for wavefront sensing), the unresolved star image is not a perfect measurement of the PSF associated with the image to be deconvolved [8, 11, 13, 14]. Actually, the main source of PSF variability is the seeing fluctuation.

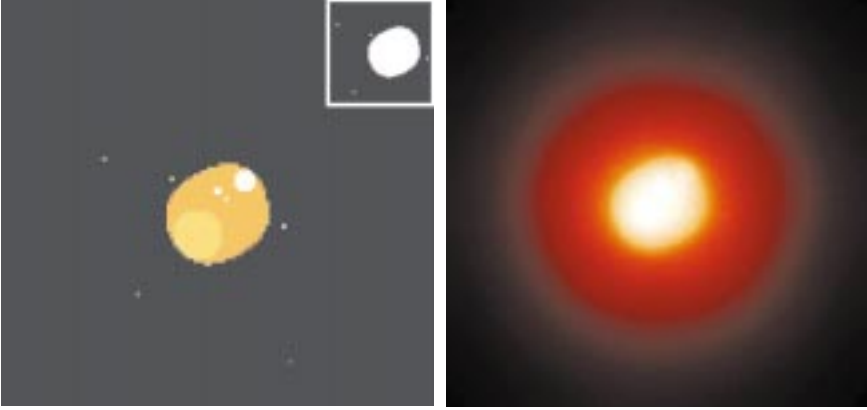


Figure 1: Planetary-type object ($m_v = 11$) and its simulated VLT-NAOS image at $0.5 \mu\text{m}$ and for a 0.73 arcsec seeing. The Strehl Ratio (SR) is 2.1%. The number of detected photons in the image is $10^8 \text{ photo} - e^-$, the background noise has a $31 e^-$ standard deviation. The Field of View is 0.8 arcsec , $128 \times 128 \text{ pixel}$ image. The planetary disk is constituted of a uniform level plus a broad feature 10% brighter, and three small spots, 30% brighter. Four stars are added in the field with a 2.5 magnitude difference between the brightest and the faintest. The faintest corresponds to 40,000 detected photons, which corresponds to a maximum contribution of 155 photons/pixel in the image. The true object top-right display gives a log-scale representation.

The sensibility of the Optical Transfer Function (OTF) to the seeing variations is illustrated in Figure 2. The OTFs are estimated for a seeing ranging from 0.65 to 0.93 arcsec. The corresponding SRs go from 3.8% down to 0.4%. The structure of the OTFs is typical of an AO corrected OTF [4, 5, 6, 7]: a low-frequency lobe and a high-frequency wing going up to the telescope cut-off frequency. The spatial frequencies between r_o/λ and D/λ , which would be lost without correction, are now preserved. The high-frequency level is however low and very dependent of the seeing conditions. Here it changes by a factor of ten for rather realistic seeing changes.

The OTFs presented here derive from a careful study of the system performance [12, 15]. The corresponding PSF at 0.73 arcsec seeing is shown in Figure 3. Note that despite the very low SR in the visible, a coherent peak is still clearly seen above the broad halo. This is characteristic of high-order correction systems such as the VLT-NAOS one working in the visible: the residual phase variance is large due to the short wavelength, but the phase is mainly constituted of high-order modes, hence the particular PSF profile. We will show in Section 4 that MISTRAL can restore high-resolution maps out of these low SR visible VLT-NAOS images. Note that this suggests that the SR is not a good measurement of the image quality, when quality means "restorability" [7].

Of course, the deconvolution can also be applied to IR images with more reasonable SRs as shown on ADONIS data in Section 5. But we first recall the deconvolution approach in the following section.

3. Deconvolution Approach

Most deconvolution techniques boil down to the minimisation (or maximisa-

tion) of a criterion. The first issue is the definition of a suitable criterion for the given inverse problem. The criteria presented here will be derived from a probabilistic approach. The second problem is then to find the position of the criterion's global minimum which is defined as the solution. In some cases, it is given by an analytical expression, but most of the time one has to use an iterative numerical method to solve the problem.

In the following sections, we first consider the case of an assumedly known PSF, so-called "classical" deconvolution; the method is then extended to the joint estimation of the object and the PSF, called here "myopic" deconvolution.

3.1 Deconvolution with known PSF

Following a probabilistic approach, called maximum *a posteriori* [MAP] [16],

the deconvolution problem can be stated as follows: we look for the most likely object \mathbf{o} given the observed image \mathbf{i} . This reads:

$$\begin{aligned} \hat{\mathbf{o}}_{\text{map}} &= \arg \max_{\mathbf{o}} p(\mathbf{o}|\mathbf{i}) = \\ &= \arg \max_{\mathbf{o}} p(\mathbf{i}|\mathbf{o}) \times p(\mathbf{o}) = \\ &= \arg \min_{\mathbf{o}} [J_n(\mathbf{o}) + J_o(\mathbf{o})]. \end{aligned} \quad (2)$$

The criterion to be minimised, $J = J_n + J_o$, is composed of a first term ($J_n = -\ln p(\mathbf{i}|\mathbf{o})$) accounting for the noise statistics in the image, plus a second term ($J_o = -\ln p(\mathbf{o})$) which allows to use the *a priori* knowledge we have on the object. This last term, of course, is a function of the type of object being observed. The choice of J_o for planetary-type objects is discussed in the Section 3.1.2.

If no prior knowledge is available, one can still use the previous equations with $p(\mathbf{o}) = 1$. One therefore only maximises $p(\mathbf{i}|\mathbf{o})$, also called likelihood of the data, to obtain a maximum-likelihood solution. In this case the criterion is only constituted of the term J_n .

3.1.1 Maximum likelihood with photon noise

If the image is corrupted solely by photon noise, the maximum likelihood [ML] solution minimises the following criterion, directly derived from the expression of Poisson statistics:

$$\begin{aligned} J_n^{\text{poisson}}(\mathbf{o}) &= -\ln p(\mathbf{i}|\mathbf{o}) = \\ &= \sum_r (\mathbf{h} * \mathbf{o})(r) - \mathbf{i}(r) \ln[(\mathbf{h} * \mathbf{o})(r)]. \end{aligned} \quad (3)$$

The Richardson-Lucy algorithm [RL] [17, 18] is an iterative numerical method which converges towards the global minimum of J_n^{poisson} .

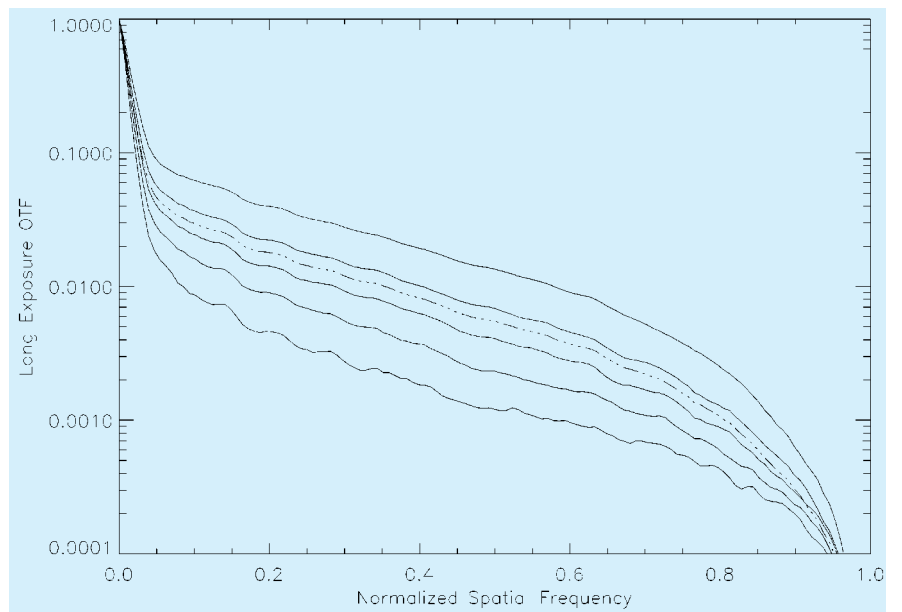


Figure 2: The OTFs are estimated for the following seeing values: from top to bottom, 0.65, 0.73, 0.79, 0.85 and 0.93 arcsec. The corresponding SRs are respectively: 3.8%, 2.1%, 1.3%, 0.8% and 0.4%. The mean OTF is also drawn (dashed line).

It is however well known that the restoration of the object using the sole data is an unstable process (see in particular Refs. [19] and [16] for reviews). The noise is highly amplified in the solution. Of course, one can stop the RL before convergence to limit the noise amplification but in this case the solution is poorly defined. For sure, it is no more the minimum of any criterion. A better solution is to regularise the problem with an adequate object prior as proposed in Section 3.1.2.

3.1.2 Edge preserving regularised deconvolution

In the MISTRAL algorithm, we consider a white non-stationary Gaussian noise in the image, which is a good approximation of a mix of photon and background (detector or sky-background) noise. Furthermore, the deconvolution is regularised by an object prior particularly adapted for planetary-like objects. This prior avoids the usual ringing artefacts [20] given by standard deconvolution techniques on such sharp edge objects [21, 8]. The criterion to be minimised is:

$$J(\mathbf{o}) = J_n(\mathbf{o}) + J_o(\mathbf{o}) = \sum_r \frac{1}{2\sigma^2(r)} (i(r) - (\mathbf{o} * \mathbf{h})(r))^2 + J_o(\mathbf{o}), \quad (4)$$

where $\sigma^2(r)$ is the image thresholded to the background noise variance. In the absence of background noise, this expression of J_n is actually a first-order development of Eq. 3. The regularisation term is defined as:

$$J_o(\mathbf{o}) = \mu \sum_r \left[\left(\frac{\Delta \mathbf{o}(r)}{\delta} \right) - \ln \left(1 + \frac{\Delta \mathbf{o}(r)}{\delta} \right) \right], \quad (5)$$

where $\Delta \mathbf{o}(r) = \sqrt{\Delta_x \mathbf{o}(r)^2 + \Delta_y \mathbf{o}(r)^2}$, $\Delta_x \mathbf{o}$ and $\Delta_y \mathbf{o}$ are the object finite difference gradients along x and y respectively.

This regularisation, called $L_1 - L_2$, is an isotropic version of the expression suggested by Brette [22]. The global factor μ and the threshold δ have to be adjusted according to the noise level and the structure of the object. This is currently done by hand but an automatic procedure is under study.

We use a fast conjugate gradient method [23] to minimise the global criterion J given in Eq. 4. This method is well adapted since the so-defined criterion is convex. An additional positivity constraint is used in MISTRAL, it is enforced with a reparameterisation method ($\mathbf{o} = \mathbf{a}^2$) [24] where \mathbf{a} are the new parameters used in the minimisation.

3.2 Myopic deconvolution

As mentioned in Section 2, the true residual PSF is seldom available. MIS-

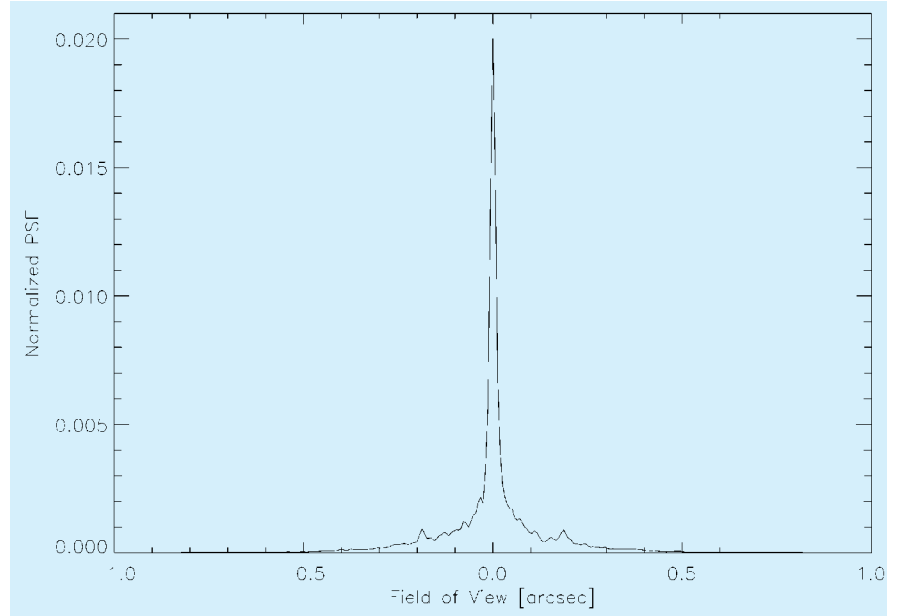


Figure 3: VLT-NAOS PSF at $0.5 \mu\text{m}$, for 0.73 arcsec seeing and a guide star magnitude $m_V = 11$. The PSF is normalised to its Strehl Ratio $SR \approx 2.1\%$.

TRAL has the ability to estimate both the object and PSF from the image and some imprecise PSF measurement. The Eqs. 2 and 4 can indeed be generalised, in the same probabilistic framework, to the case of a joint estimation of $[\mathbf{o}, \mathbf{h}]$. One obtains:

$$\begin{aligned} [\hat{\mathbf{o}}, \hat{\mathbf{h}}] &= \arg \max_{\mathbf{o}, \mathbf{h}} \rho(\mathbf{o}, \mathbf{h} | \mathbf{i}) = \\ \arg \max_{\mathbf{o}, \mathbf{h}} \rho(\mathbf{i} | \mathbf{o}, \mathbf{h}) \times \rho(\mathbf{o}) \times \rho(\mathbf{h}) &= \quad (6) \\ \arg \min_{\mathbf{o}, \mathbf{h}} [J_n(\mathbf{o}, \mathbf{h}) + J_o(\mathbf{o}) + J_h(\mathbf{h})]. & \end{aligned}$$

The myopic criterion is given by Eqs. 4 and 5, now a function of \mathbf{o} and of \mathbf{h} , plus an additional term $J_h = -\ln \rho(\mathbf{h})$ which accounts for the knowledge, although partial, available on the PSF. Assuming stationary Gaussian statistics for the PSF, J_h reads:

$$J_h(\mathbf{h}) = \frac{1}{2} \sum_f \frac{|\tilde{\mathbf{h}}(f) - \tilde{\mathbf{h}}_m(f)|^2}{PSD_h(f)}, \quad (7)$$

where $\tilde{\mathbf{h}}_m = E[\tilde{\mathbf{h}}]$ is the mean OTF, and $PSD_h = E[|\tilde{\mathbf{h}}(f) - \tilde{\mathbf{h}}_m(f)|^2]$ is the associated spatial Power Spectral Density [PSD].

Such a regularisation obviously ensures that the actual OTF is close to the mean OTF with respect to error bars given by the PSD, which characterises the fluctuations around the mean. In practice, the mean PSF and the PSD are estimated by replacing, in their definitions, the expected values ($E[\cdot]$) by an average on the different images recorded on the unresolved star. Ideally one would want to estimate the PSF from the wavefront sensing data [10, 25] which would avoid the errors due to seeing fluctuations. But even in this case, the myopic approach can be interesting to account for the PSF uncertainties due to constant aberration cali-

bration errors [9] or to the wavefront sensing noise for faint stars.

Note that the new criterion is convex in \mathbf{o} for a given \mathbf{h} , convex in \mathbf{h} for a given \mathbf{o} but it is not convex on the whole parameter space. However, it is possible to use starting points that are close to the global minimum, and we did not encounter minimisation problems with the conjugate gradient method. A positivity constraint is also used on the PSF ($\mathbf{h} = \mathbf{b}^2$).

4. Deconvolution of Simulated VLT-NAOS Images

The application of MISTRAL to the simulated VLT-NAOS visible image presented in Section 2 is discussed here.

Figure 4 shows the results obtained in the ideal case of a classical deconvolution using the true PSF. The deconvolution obtained with MISTRAL at convergence (360 iterations) of the minimisation of Eq. 4 is compared to the RL estimation stopped respectively at 1000, 6830 and 50,000 iterations. In each case a log-scale version of the restored object is shown in order to check the detection of the faint stars in the background.

A quantitative measurement of the restoration quality can be given in terms of distance to the true object, rms value expressed in photons/pixel and computed on the full field of view. The distance is 5150 photons/pixel for the MISTRAL estimate, and respectively 11,800, 9900 and 13,900 photons/pixel for the RL cases. The evolution of the distance with the computation time is given in Figure 5. The estimate obtained with 6830 iterations and shown in Figure 4 therefore corresponds to the best RL estimate. The starting point is always the image thresholded to a slightly positive level for implementation

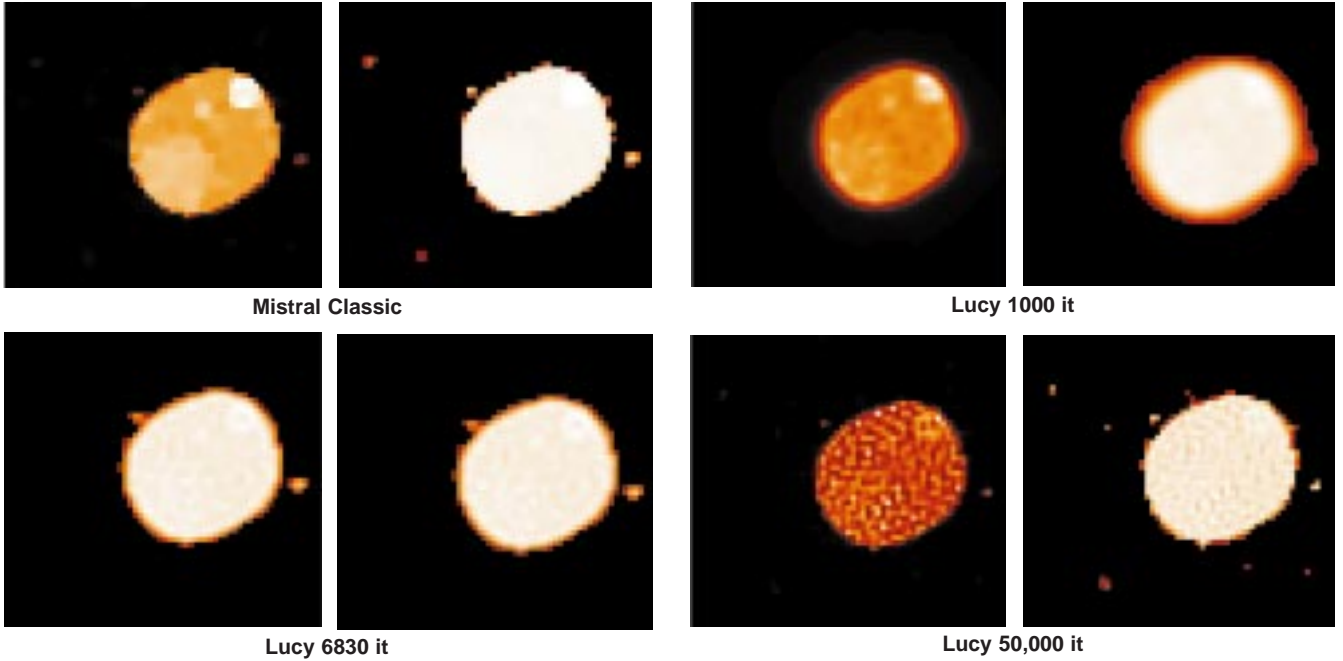


Figure 4: Classical deconvolution with MISTRAL and RL estimates with 1000, 6830 and 50,000 iterations. The PSF is the true PSF. The deconvolution is performed on the 0.8 arcsec field of view but only a 0.4 arcsec subfield is displayed. In each case we show the corresponding log-scale map (right-hand side panel in each pair of images). The distance to the true object is 5150 photons/pixel with MISTRAL and respectively 11,800, 9900 and 13,900 photons/pixel for the RL cases.

of the positivity. The RL estimate never reaches the distance obtained with MISTRAL and diverges for a large number of iterations. It goes from a low-resolution estimate with ringing artefacts to a very noisy one. The restoration quality is obviously much higher with our regularised algorithm. The global photometry is very precisely restored. The stars in the background are well detected and only slightly smoothed. This large dynamic is permitted by a good model of the image noise. Note also that MISTRAL reaches convergence in a quite reasonable amount of time (≈ 390 s and 360 iterations), roughly the same time required for RL to reach its best estima-

tion (≈ 330 s and 6800 iterations). Note also that MISTRAL is able to both restore the edge of the object and the structures on the surface.

We then consider the case of a poor estimation of the PSF. We recall that the image was obtained with a PSF corresponding to a 0.73 arcsec seeing. We assume that 5 images of an unresolved star were recorded shortly before or after. The seeing is supposed to be unstable and the seeing is actually 0.65, 0.73, 0.79, 0.85 and 0.93 arcsec respectively for each of these calibration images. The OTF estimates are shown in Figure 2 as well as the mean OTF. Since it can be difficult to estimate precisely the seeing conditions to select

the correct OTF, one may want to use a classical deconvolution assuming that the true OTF is the mean OTF. The result obtained with MISTRAL with this assumption is shown in Figure 6. Despite the fact that the mean OTF is close to the true one ($SR = 1.7\%$ instead of 2.1%), the restoration is poor: artefacts on the surface, apparent diameter underestimated, no detection of the surrounding stars. The distance to the true object is large ($\approx 23,000$ photons/pixel). The other approach is to use MISTRAL in the myopic mode (minimisation at convergence of Eq. 6) with the same mean OTF and a PSD which is nothing but the variance estimated out of these 5 OTF measurements for each spatial frequency. The restoration is very similar to that obtained with the true PSF. The distance to the true object is ≈ 6800 photons/pixel. Note however that part of the dynamic is lost. Only the two brightest stars are detected. The computation time required in the myopic case is ≈ 1900 s (1600 iterations) which is still quite reasonable.

5. Deconvolution of Experimental ADONIS Data

ADONIS, the AO system mounted on the 3.6-m telescope of the La Silla observatory, has been routinely used by the ESO community since 1993. The wavefront distortions of the visible incoming light are measured using one of the two Shack-Hartmann wavefront sensors (WFS). The 52-actuators deformable mirror and tip-tilt mirror control is performed by a modal optimisation. ADONIS is the only AO system providing an imaging facility in the 1–5 μm range via two NIR cameras. The plane-

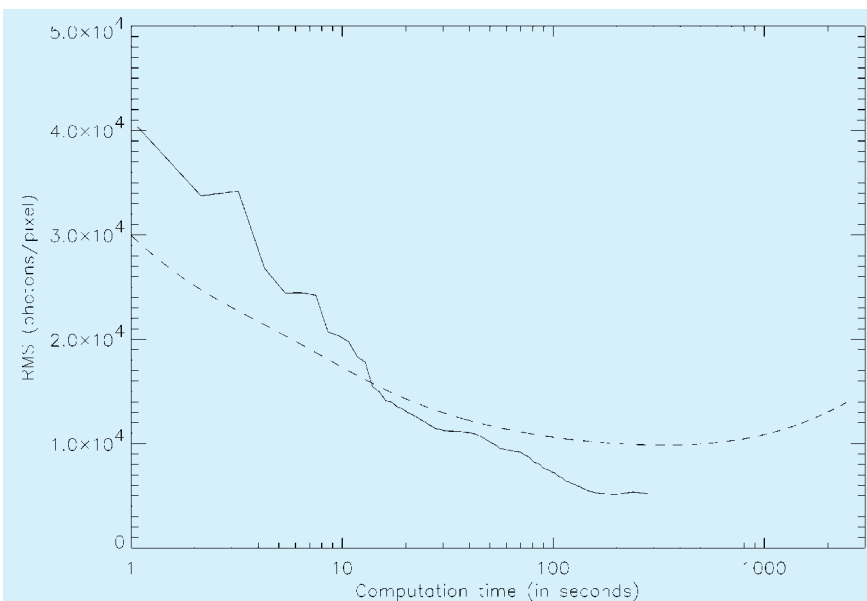


Figure 5: Distance to the true object, rms value expressed in photons/pixel, versus computation time: MISTRAL (solid line), RL (dashed line).



Figure 6: MISTRAL classical deconvolution with mean PSF considered as the true PSF and myopic deconvolution. In each case we show the corresponding log-scale map. The deconvolution is performed on the 0.8 arcsec field of view but only a 0.4 arcsec sub-field is displayed. The distance to the true object is respectively 23,000 and 6800 photons/pixel (see Section 4).

tary observations presented below have been performed without prefocal optics using broad-band filters.

5.1 Monitoring of Io's volcanism

Io's volcanic activity, attributed to internal heating due to tidal effects between Jupiter and Io, was first discovered from space with Voyager 1 and 2 in 1979. They have shown the presence of active volcanic centres, called hot spots, detectable by their IR emission. Since then, and because of the increase in IR detector sensitivity, Io's variable volcanos of the Jupiter-facing hemisphere have been studied by ground-based observations when Io is located in the shadow of Jupiter [27]. Since October 1996, ADONIS AO system coupled with its COMIC thermal camera (CEA/LIR/LETI detector, 128×128 , 100 mas/pixel) has been used to monitor Io's volcanic activity [28]. Observations performed with a L' broad-band filter ($\lambda_c = 3.8 \mu\text{m}$) using the satellite itself as reference (angular size ~ 1.0 arcsec, $m_v \sim 5$) allow a complete mapping of its surface. In this spectral range, the AO correction is quite efficient and the typical SR obtained is around 45% with a 0.8 arcsec seeing.

An AO corrected image and the corresponding PSF are presented in Figure 7. Only the bright Loki hot spot is detected on the AO corrected image. A deconvolution is required to study other structures. In addition to the residual blur, the image incorporates a rather uniform high-level background emission produced by the sky and the bench optical elements [29] and a variable and inhomogeneous background modulated by the AO correction [30]. A good background subtraction is of course important for the deconvolution.

We present in Figure 8 two consecutive images of Io's Jupiter-facing hemisphere taken in September 1998 and processed with MISTRAL [31]. We used the myopic mode to account for seeing variations. Loki, well-known hot spot located on the Jupiter-facing hemisphere, is quite active and surrounded by secondary outbursts. Standard deconvolution processes cannot be applied on these data. Indeed, in the absence of edge-preserving regularisation term, the whole energy of the disk tends to be concentrated in the bright Loki feature. Our observations are well correlated to, and complement those, made by

Galileo/NIMS spectrocamera [26] (see Fig. 8). The coupling of AO system with a thermal camera and the use of a specific deconvolution process for planetary objects, such as MISTRAL, is very promising for our understanding of Io's volcanism which can only be accomplished by a frequent monitoring of its activity.

5.2 Study of the Uranian system

Uranus has been observed with broad-band filters (J,H,K) using the SHARPII+ camera (Rockwell NICMOS3 detector, 1–2.5 μm , 100 mas/pixel) on May 2, 1999. These observations have been performed thanks to the capability of the Shack-Hartmann WFS to analyse the wavefront on an extended object. Because of the relatively small angular size of the planet (2.6 arcsec) and the excellent seeing condition (0.5 arcsec and very stable), the correction quality was high and we got a SR of 48% in K band (2.2 μm). The centroid position error, in each sub-pupil, is however higher on extended objects, hence a degraded AO performance on such extended objects. The image of an unresolved star is therefore a biased measurement of the

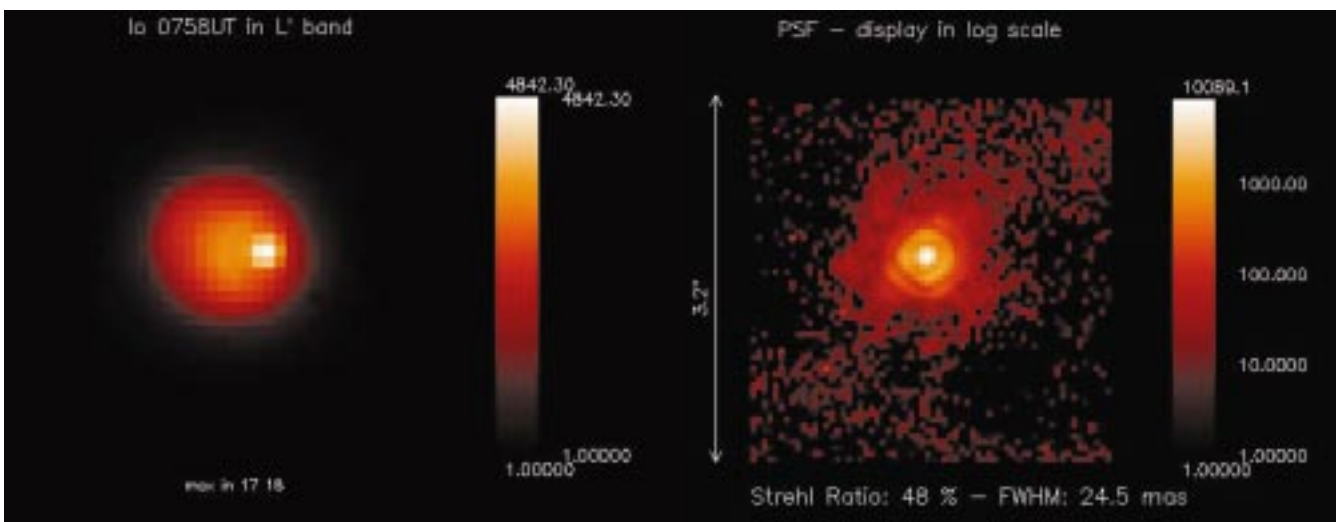


Figure 7: ADONIS image of Io and a log-scale representation of the corresponding PSF. Only the bright Loki hot spot is detected on the Io's disk.

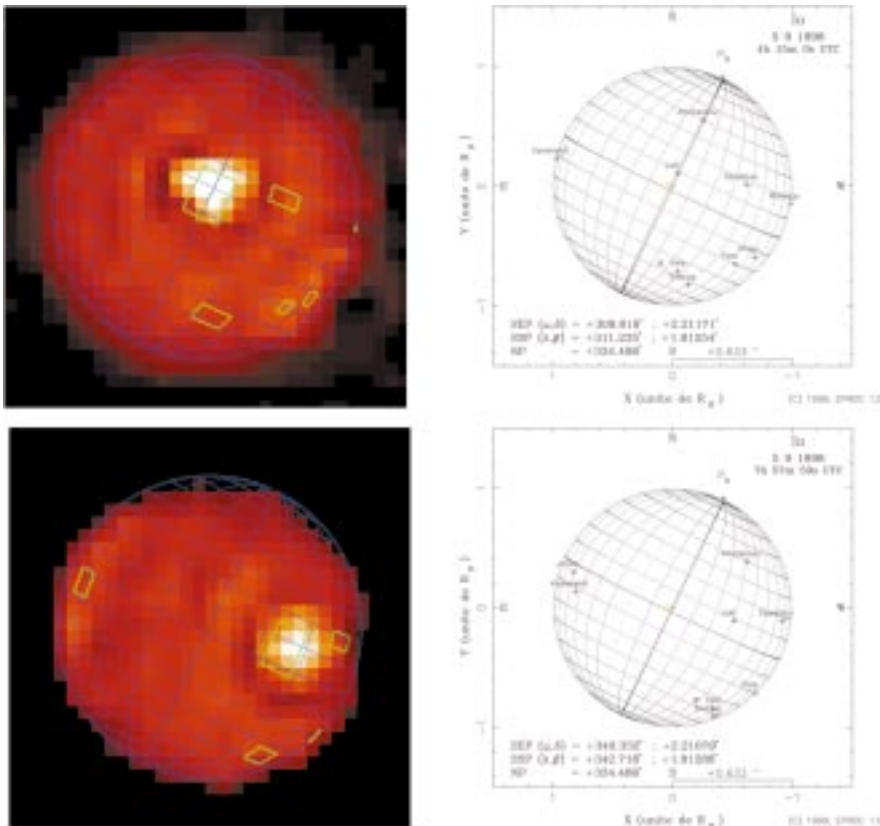


Figure 8: Two consecutive images of the Jupiter-facing hemisphere of Io observed with ADONIS/COMIC in L-band and processed with MISTRAL. The green boxes correspond to the projection of the hot spots detected by Galileo/NIMS during the first four orbits [26]. The right panel indicates the geometry of Io at the date of the observation and the name of the known hot spots (courtesy Bureau des Longitudes). See Section 5.

PSF and a myopic deconvolution method is definitely necessary to restore the initial sharpness of the images. Figure 9 displays a set of data after deconvolution with MISTRAL. In J (1.2 μm) and H (1.6 μm) bands, the planetary disk is not uniform as observed in the visible and shows bright polar haze distributed along a latitude. In K band, due to the methane atmospheric absorption band, the planet is dark and the brightest feature is the Epsilon ring with its longitudinal anomaly.

J and H band (Fig. 10), one can see the Epsilon ring and also some innermost ones. The exterior satellites Ariel, Miranda and Puck can be detected with standard deconvolution such as RL. But the myopic deconvolution process also reveals the presence of the innermost satellites, Portia, Rosalind, Bianca and Juliet (see Fig. 10) which have been discovered by Voyager 2 in 1986 and never re-observed since then. After these first successful observations, the monitoring of Uranus and its environment will continue. The AO system fa-

cility and the accurate MISTRAL deconvolution method will allow us to study the atmospheric activity of the planets, the colour and composition of the rings. The comparison of the positions of the faintest satellites with ephemerides will also better constrain physical parameters (body masses, flattening factor . . .) and to elaborate a more accurate analytical theory of the satellite motion [32].

6. Conclusion

MISTRAL is a myopic deconvolution algorithm particularly adapted for AO corrected images of astronomical objects. It accounts for the noise in the image, for the presence of sharp structures in the object and for the fact that the PSF is usually not perfectly known. Its ability to provide high photometric precision estimates with a quite reasonable computation time has been illustrated on simulated data. The simulation conditions correspond to a VLT-NAOS observation in the visible. Since the system is optimised in the near IR, the correction quality in the visible is low ($SR \approx 2\%$ here). Even in such severe conditions, a diffraction-limited restoration is obtained.

MISTRAL has also been applied to ADONIS images of Io in the thermal domain, and images of Uranus in the near IR. In addition to the bright hot spot Loki, secondary outbursts were observed on Io's Jupiter-facing hemisphere. Such observations are very promising for our understanding of Io's volcanism which can only be accomplished by frequent monitoring of its activity. Concerning Uranus, the structures of the rings and its innermost satellites have been successfully detected. We will continue a monitoring of Uranus and its environment. Solar-system studies (atmospheric activity of the planets, colour and composition of the rings, position of the faint satellites) require high-resolution and high-photometric-precision data. These can be ob-

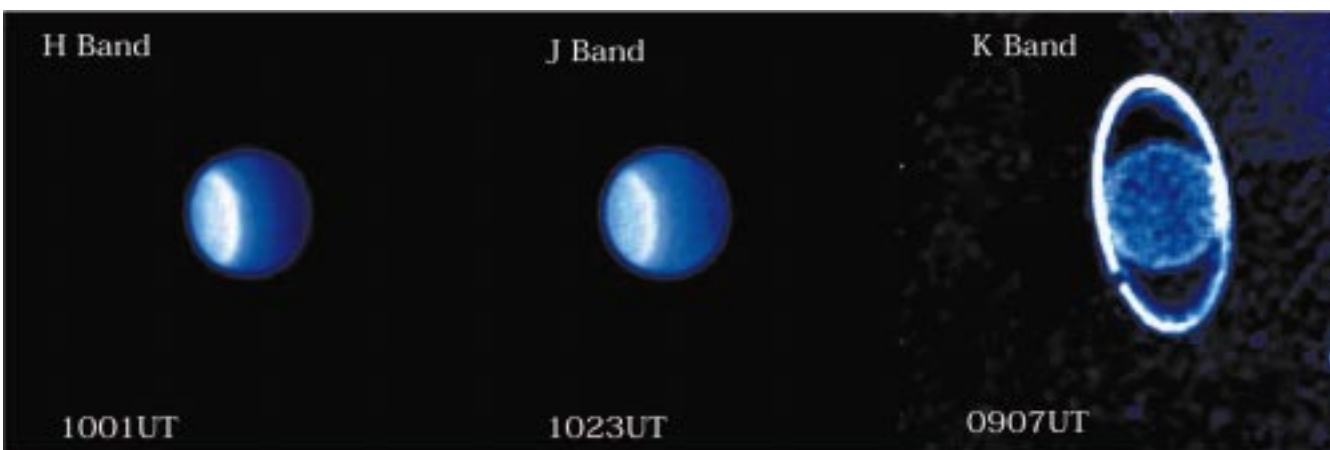


Figure 9: Uranus observed in May 1999 (north is down, east is left) after deconvolution by MISTRAL. In J and H bands, the hazy atmospheric regions are clearly visible around the pole. In K band, the methane atmospheric band absorbs the solar light and the bright feature observed is the Epsilon ring and its longitudinal anomaly.

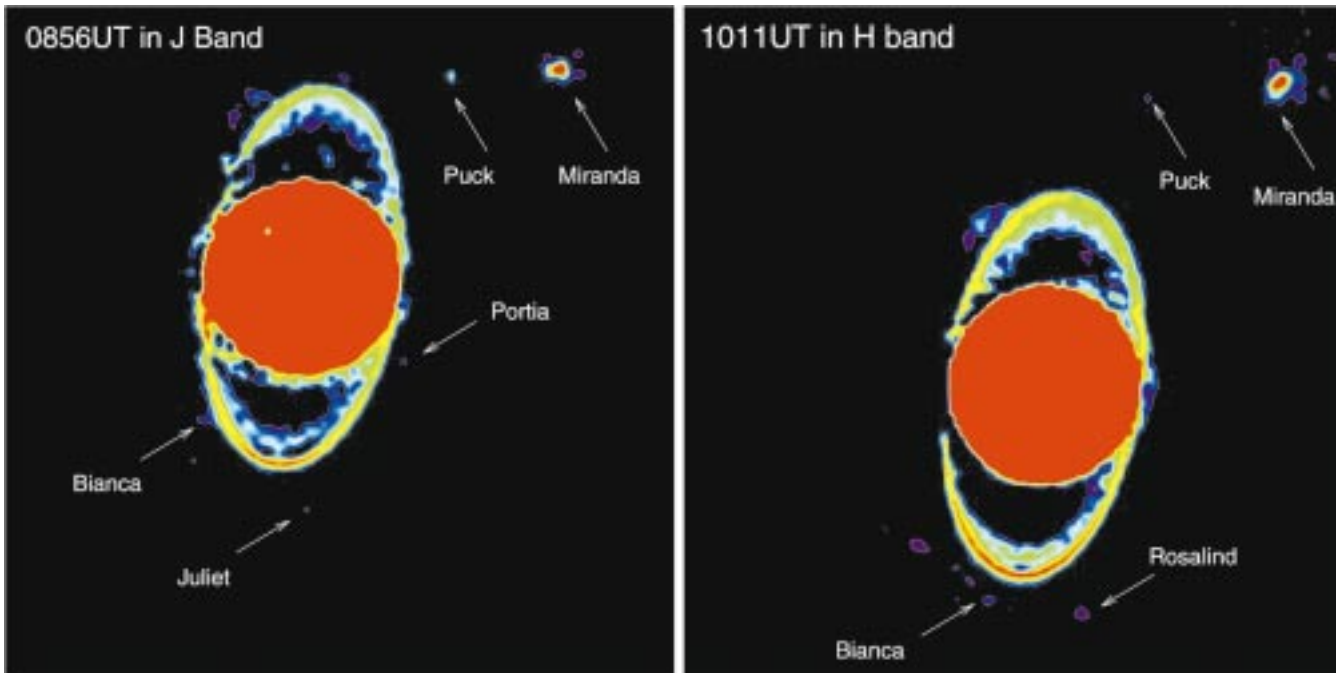


Figure 10: Logarithmic display of the MISTRAL images (north is up and east is left) showing the lowest intensity levels in the J and H images. Innermost rings and faintest satellites (first observed with Voyager in 1986) are also detected.

tained with large telescope AO observations in conjunction with a high-precision deconvolution technique.

7. Acknowledgements

The authors thank Gérard Rousset, Vincent Michau, Claude and François Roddier, Jérôme Idier and Guy Le Besnerais for many fruitful discussions. We are indebted to ESO-3.6-m support team, in particular the Telescope Operators for their assistance during these difficult and unusual planetary object observations.

References

- [1] J.W. Hardy, J. E. Lefevbre, and C.L. Koliopoulos, "Real time atmospheric compensation", *J. Opt. Soc. Am.* **67**, 360–369 (1977).
- [2] G. Rousset, J.-C. Fontanella, P. Kern, P. Gigan, F. Rigaut, P. Léna, C. Boyer, P. Jagourel, J.-P. Gaffard, and F. Merkle, "First diffraction-limited astronomical images with adaptive optics", *A&A* **230**, 29–32 (1990).
- [3] *Adaptive Optics in Astronomy*, F. Roddier, ed., (Cambridge University Press, 1999).
- [4] F. Rigaut, G. Rousset, P. Kern, J.-C. Fontanella, J.-P. Gaffard, F. Merkle, and P. Léna, "Adaptive optics on a 3.6-m telescope: results and performance", *A&A* **250**, 280–290 (1991).
- [5] M.C. Roggemann and C.L. Matson, "Power spectrum and Fourier phase spectrum estimation by using fully and partially compensating adaptive optics and bispectrum postprocessing", *J. Opt. Soc. Am. A* **9**, 1525–1535 (1992).
- [6] J.M. Conan, P.Y. Madec, and G. Rousset, "Image formation in adaptive optics partial correction", in *Active and Adaptive Optics*, (Garching, Germany, 1993).
- [7] J.-M. Conan, "Étude de la correction partielle en optique adaptative", Ph.D. thesis, Université Paris XI Orsay, 1994.
- [8] J.-M. Conan, T. Fusco, L. Mugnier, E. Kersalé, and V. Michau, "Deconvolution of adaptive optics images with imprecise knowledge of the point spread function: results on astronomical objects", in *Astronomy with adaptive optics: present results and future programs*, (Sonstofen, 1998).
- [9] T. Fusco, J.-P. Véran, J.-M. Conan, and L. Mugnier, "Myopic deconvolution method for adaptive optics images of stellar fields", *A&A Suppl. Ser.* **134**, 1–10 (1999).
- [10] J.-P. Véran, F. Rigaut, H. Maître, and D. Rouan, "Estimation of the adaptive optics long exposure point spread function using control loop data", *J. Opt. Soc. Am. A* **14**, 3057–3069 (1997).
- [11] J.-M. Conan, L. M. Mugnier, T. Fusco, V. Michau, and G. Rousset, "Myopic Deconvolution of Adaptive Optics Images using Object and Point Spread Function Power Spectra", *Appl. Opt.* **37**, 4614–4622 (1998).
- [12] G. Rousset et al., "Design of the Nasmyth Adaptive Optics System (NAOS) of the VLT", in *Astronomical Telescopes & Instrumentation*, D. Bonaccini and R. K. Tyson, eds., 3353 (Kona, Hawaii, 1998).
- [13] J.C. Christou, "Deconvolution of adaptive optics images", in *ESO/OSA topical meeting on astronomy with adaptive optics present results and future programs*, (1998).
- [14] E. Tessier, "Image quality with current adaptive optics instruments", *A&A Suppl. Ser.* **125**, 581–593 (1997).
- [15] J.-M. Conan, D. Mouillet, E. Gendron, and G. Rousset, "NAOS analysis report Issue 2.0", Rapport Technique VLT-TRE-NAO-11650-1-000000-0002, ONERA (1999), contract ESO.
- [16] G. Demoment, "Image Reconstruction and Restoration: Overview of Common Estimation Structures and Problems", *IEEE Trans. Acoust. Speech Signal Process.* **37**, 2024–2036 (1989).
- [17] W.H. Richardson, "Bayesian-based iterative method of image restoration", *J. Opt. Soc. Am.* **62**, 55–59 (1972).
- [18] L. B. Lucy, "An iterative technique for rectification of observed distributions", *Ap.J.* **79**, 745–754 (1974).
- [19] D. M. Titterton, "General structure of regularization procedures in image reconstruction", *A&A* **144**, 381–387 (1985).
- [20] J.-P. Véran, "Estimation de la réponse impulsionnelle et restauration d'image en optique adaptative – Application au système d'optique adaptative du Télescope Canada-France-Hawaii", Ph.D. thesis, Ecole Nationale Supérieure des Télécommunications, 1997.
- [21] L. M. Mugnier, J.-M. Conan, T. Fusco, and V. Michau, "Joint Maximum a Posteriori Estimation of Object and PSF for Turbulence Degraded Images", in *Bayesian Inference for Inverse problems*, **3459**, 50–61 (San Diego, CA (USA), 1998).
- [22] S. Brette and J. Idier, "Optimized Single Site Update Algorithms for Image Deblurring", in *Proceedings of the International Conference on Image Processing*, p. 65–68 (Lausanne, Switzerland, 1996).
- [23] Groupe Problèmes Inverses, "GPAV: une grande œuvre collective", internal report, Laboratoire des Signaux et Systèmes, CNRS/Supélec/Université Paris-Sud (1997).
- [24] E. Thiébaud and J.-M. Conan, "Strict a priori constraints for maximum-likelihood blind deconvolution", *J. Opt. Soc. Am. A* **12**, 485–492 (1995).
- [25] S. Harder, "Reconstruction de la réponse impulsionnelle du système d'optique adaptative ADONIS a Dartir des mesures de son analyseur de surface d'onde et Étude photométrique de la variabilité des étoiles YY Orionis", Ph.D. thesis, Université Joseph Fourier, Grenoble 1, 1999.
- [26] R. Lopes-Gautier, A. Davies, R. Carlson, W. Smythe, L. Kamp, L. Soderblom, F. E.

- Leader, and R. Mehlman, "Hot spots on Io: Initial results from Galileo's near infrared mapping spectrometer", *Geophys. Res. Lett.* **24**, 2439 (1997).
- [27] J. R. Spencer, J. A. Stansberry, C. Dumas, D. Vakil, R. Pregler, M. Hicks, and K. Hege, "History of high-temperature Io volcanism: February 1995 to May 1997", *Geophys. Res. Lett.* **24**, 2451 (1997).
- [28] F. Marchis, R. Prangé, and J.C. Christou, "Adaptive Optics mapping of Io's volcanism in the thermal IR", *Icarus* (1999), submitted.
- [29] D. Le Mignant, E. Gendron, and F. Marchis, "The ESO ADONIS adaptive optics system: Study of the 3-5 μ m background emissivity", in *ESO conference and workshop proceedings* **56**, 575 (Garching, Germany, 1998).
- [30] H. Geoffray, "Thermal background blurring on ADONIS system", in *ESO conference and workshop proceedings* **56**, 531 (Garching, Germany, 1998).
- [31] R. Prangé, F. Marchis, and T. Fusco, "Mapping and monitoring of Io's hot spots by use of the ESO Adaptive Optics system.", in *31st Annual Meeting of the DPS*, (Padova, Italy, 1999).
- [32] F. Marchis, J. Berthier, P. Descamps, T. Fusco, R. Prangé, and T. Sekiguchi, "Ground-based high resolution observations of the Uranian system in the near IR", in *31st Annual Meeting of the DPS*, (Padova, Italy, 1999).

A New Look at the Sombrero Galaxy



This image of Messier 104, also known as Sombrero Galaxy, because of its particular shape, was obtained with FORS1 at VLT Antu on January 30, 2000. The colour image was made by a combination of three CCD images obtained by Peter Barthel from the Kapteyn Institute at Groningen, Netherlands. He and Mark Neeser, also from the Kapteyn Institute, produced the composite images. The "Sombrero" is notable for its dominant nuclear bulge, composed primarily of old stars, and its nearly edge-on disk composed of stars, gas and intricately structured dust. The complexity of this dust and the high resolution of this image are most apparent directly in front of the bright nucleus, but it is also evident as dark absorbing lanes throughout the disk.

CERN, ESA and ESO Launch "Physics On Stage"

(Taken from ESO Press Release 04/00)

Physics is everywhere. The laws of physics govern the Universe, the Sun, the Earth and even our own lives. In today's rapidly developing society, we are becoming increasingly dependent on high technology. Computers, transport, and communication are just some of the key areas that are the result of discoveries by scientists working in physics.

But how much do the citizens of Europe really know about physics? Here is a unique opportunity to learn more about this elusive subject!

Beginning in February 2000, three major European research organisations are organising a unique Europe-wide programme to raise the public awareness of physics and related sciences.

"Physics on Stage" is launched by the European Laboratory for Particle Physics (CERN), the European Space Agency (ESA) and the European Southern Observatory (ESO), with support from the European Union. Other partners are the European Physical Society (EPS) and the European Association for Astronomy Education (EAAE).

This exciting programme is part of the European Week for Science and Technology and will culminate in a Science Festival during November 6–11, 2000, on the CERN premises at the French-Swiss border near Geneva.

Why "Physics on Stage"?

The primary goal of "Physics on Stage" is to counteract the current decline in interest and knowledge about physics among Europe's citizens by means of a series of highly visible promotional activities. It will bring together leading scientists and educators, government bodies and the media, to confront the diminishing attraction of physics to young people and to develop strategies to reverse this trend.

The objective in the short term is to infuse excitement and to provide new educational materials. In the longer term, "Physics on Stage" will generate new developments by enabling experts throughout Europe to meet, exchange and innovate.

"Physics on Stage" in 22 European Countries

"Physics on Stage" has been initiated in 22 European countries¹. In each of these, a dedicated National Steering Committee is being formed which will be responsible for its own national programme.

"Physics on Stage" is based on a series of high-profile physics-related activities that will inform the European public in general and European high-school physics teachers and media representatives in particular about innovative ways to convey information about physics. It will stress the intimate connection of this natural science with our daily lives. It will be accompanied by a broad media debate on these subjects.

What will happen during "Physics on Stage"?

During the first phase of "Physics on Stage", from now until October 2000, the individual National Steering Committees (NSCs) will survey the situation in their respective countries. The NSCs will collaborate with national media to identify new and exciting educational approaches to physics. These may involve demonstrations, interactive experiments, video and CD-Rom presentations, Web applications, virtual reality, theatre performances, etc.

Nationally run competitions will select some of the best and most convincing new ideas for presentations and educational materials which will receive development support from "Physics on Stage".

The project will culminate in November 2000, with approxi-

mately 400 delegates converging on CERN, in Geneva, for the Physics on Stage Festival. During this event, the national competition winners, science teachers, science communicators, publishers, top scientists and high-level representatives of the ministries and European organisations will brainstorm future solutions to bolster physics' popularity. The programme will also include spectacular demonstrations of new educational tools; the best will be disseminated over the national TV networks and other media to the European public.

Why CERN, ESA and ESO?

As Europe's principal organisations in physics research (particle physics, space and astronomy), the three recognised their mutual responsibility to address the issue through the creation of a new initiative and the creative use of their own research to attract the public and teachers alike.

About the "European Science and Technology Week"

The objective of the European Science and Technology Week is to improve the public's knowledge and understanding of science and technology – including the associated benefits for society as a whole. The Week focuses on the European dimension of research, such as pan-European scientific and technological co-operation.

The rationale for holding the Week has its roots in the importance of the role of science and technology in modern societies and the need, therefore, to ensure that the public recognises its significance in our lives.

The Week is a framework for special TV programmes, exhibitions, contests, conferences, electronic networking, and other science-related activities to promote the public understanding of science and technology.

The Week was launched in 1993, on the initiative of the European Commission. Raising public awareness of science and technology is now the subject of a clearly defined action within the Human Potential Programme of the Fifth Framework Programme.



ALMA Science Advisory Committee

The Atacama Large Millimetre Array (ALMA) project has formed a new committee to provide scientific advice to the project and outreach to the wider community. The committee holds monthly teleconferences and other meetings at regular intervals. The minutes of the teleconferences and reports from the meetings are placed on the following web site.

<http://www.eso.org:8082/committees/ASAC/index.html>

A list of the committee members can also be found on this web site. Comments or questions can be addressed directly to the individual committee members or to the committee by email via the web site. In addition, we are all willing to give colloquia or other presentations on the ALMA project.

¹The 22 countries are the member countries of at least one of the participating organisations or the European Union: Austria, Belgium, Bulgaria, the Czech Republic, Denmark, Finland, France, Germany, Greece, Hungary, Ireland, Italy, Luxembourg, the Netherlands, Norway, Poland, Portugal, the Slovak Republic, Spain, Sweden, Switzerland, United Kingdom.

ESO Studentship Programme

The European Southern Observatory research student programme aims at providing the opportunities and the facilities to enhance the post-graduate programmes of ESO member-state universities by bringing young scientists into close contact with the instruments, activities, and people at one of the world's foremost observatories. For more information about ESO's astronomical research activities please consult Research Projects and Activities. (<http://www.eso.org/projects/> or <http://www.eso.org/science/>). Students in the programme work on an advanced research degree under the formal tutelage of their home university and department, but come to either Garching or Vitacura-Santiago for a stay of up to two years to conduct part of their studies under the supervision of an ESO staff astronomer. Candidates and their national supervisors should agree on a research project together with the potential ESO local supervisor. This research programme should be described in the application and the name of the ESO local supervisor should also be mentioned. It is highly recommended that the applicants start their Ph.D. studies at their home institute before continuing their Ph.D. work and developing observational expertise at ESO.

The ESO studentship programme comprises about 14 positions, so that each year a total of up to 7 new studentships are available either at the ESO Headquarters in Garching or in Chile at the Vitacura Quarters. These positions are open to students enrolled in a Ph.D. programme in the ESO member states and exceptionally at a university outside the ESO member states.

The closing date for applications is June 15, 2000.

Please apply by using the ESO Studentship application form now available on-line (<http://www.eso.org/gen-fac/adm/pers/forms>)

European Southern Observatory
Studentship Programme
Karl-Schwarzschild-Str. 2, D-85748 Garching bei München, Germany
ksteiner@eso.org

PERSONNEL MOVEMENTS DEPARTURES

International Staff

(1 December 1999 – 31 March 2000)

ARRIVALS

EUROPE

DESSAUGES-ZAVADSKY, Miroslava (CH), Student
HAGGOUCHI, Karim (F), System Software Engineer
MODIGLIANI, Andrea (I), Astronomical Data Analysis Specialist
REJKUBA, Marina (Croatian), Student
REYES, Javier (E), Electronics/Electrical Engineer
RICHICHI, Andrea (I), Associate
TOKIVININE, Andrei (Russian), Associate

CHILE

HUTSEMEKERS, Damien (B), Operations Staff Astronomer
LAGER, Mikael (S), Microwave Engineer
ROBERT, Pascal (F), Electronics Engineer

DEPARTURES

EUROPE

ENGELBART, Lore (D), Secretary
GIANNONE, Gino (I), Software Engineer for Scheduling Tools
NICOLINI, Gianalfredo (I), Infrared Laboratory Technician
WOLF, Sebastian (D), Scientific Applications Developer for UVES
WOUDET, Patrick (NL), Fellow

CHILE

AUGUSTEIJ N, Thomas (NL), Astronomer
GEMPERLEIN, Hans (D), Infrared Instrumentation Engineer
GUNNARSSON, Lars-Göran (S), Microwave Engineer
JOGUET, Benoit (F), Student
PETR, Monika (D), Fellow
SCOBBIIE, James (GB), Telescope Software Scientist
TESCHNER, Klaus (D), Programmer

Local Staff

(1 December 1999 – 31 March 2000)

ARRIVALS

ILLANES, Esteban, Public Relations Officer, Vitacura
KAISER, Cristian, Personnel Assistant, Vitacura
MARDONES, Pedro, Electronics Engineer, Paranal
MIRANDA, Marcela, Administrative Secretary, Vitacura
QUINTANA, Rolando, Warehouse Administrative Assistant, Paranal
RIJO, Ariela, Electronics Technician, Paranal
SAGUEZ, Claudio, Warehouse Assistant, Paranal
TAPIA, Francisco, Warehouse Assistant, Paranal
ZARATE, Andres, Telescope Instrument Operator, Paranal

DEPARTURES

BRIONES, Jorge, Mecánico de Cúpulas, La Silla
PINO, Flavia, Personnel Administrative Assistant, Vitacura
PRADO, Pablo, Scientific Instrument Operator / Night Assistant, La Silla
ZAPATA, Joel, Warehouse Administrative Assistant, Paranal

Scientific Preprints

(October 1999 – February 2000)

1341. C.J. Cesarsky and M. Sauvage: A Mid and Far Infrared View of Galaxies. In: "Toward a New Millennium in Galaxy Morphology", edited by D. L. Block, I. Puerari, A. Stockton and D. Ferreira (Kluwer, Dordrecht).
1342. F. Kerber et al.: ISO Observations of Dust Formation in Sakurai's Object. Monitoring the Mass Loss of a Very Late Helium Flash Star. *A&A*.
1343. J. U. Fynbo, B. Thomsen and P. Møller: Ly α Emission from a Lyman Limit Absorber at $z = 3.036$. *A&A*.
1344. M.-H. Ulrich, A. Comastri, S. Komossa and P. Crane: The Steep Spectrum Quasar PG1404+226 with ASCA, HST and Rosat. *A&A*.
1345. V. Testa et al.: The Large Magellanic Cloud Globular Cluster NGC 1866: New Data, New Models, New Analysis. *AJ*.
1346. A. Fontana et al.: High Redshift Evolution of Optically and IR-Selected Galaxies: a Comparison with CDM Scenarios. *MNRAS*.
1347. D. Elbaz et al.: Source Counts from the 15 μ m ISOCAM Deep Surveys. *A&A*.
1348. M. Chadid, K. Kolenberg, C. Aerts and D. Gillet: First Detection of a Frequency Multiplet in the Line-Profile Variations of RR Lyrae: Towards an Understanding of the Blazhko Effect. *A&A*.
1349. T. Douvion, P. O. Lagage and C. J. Cesarsky: Element Mixing in the Cassiopeia A Supernova. *A&A Letters*.
1350. M. Romaniello, M. Salaris, S. Cassisi, N. Panagia: HST Observations of the LMC Field Around SN 1987A: Distance Determination with Red Clump and Tip of the Red Giant Branch Stars. *ApJ*.
1351. O. Marco and D. Alloin: Adaptive Optics Images at 3.5 and 4.8 μ m of the Core Arcsec of NGC 1068: More Evidence for a Dusty/Molecular Torus. *A&A*.
1352. D. Baade: Observed Periodic Phenomena. S. Steff and T. Rivinius: Heros Be Star Campaigns. *The Be Phenomenon in Early-Type Stars*. ASP Conference Series, Vol. 3 \times 10⁶, 2000. M. A. Smith, H. F. Henrichs and J. Fabregat, eds.
1353. F. Paresce and G. De Marchi: On the Globular Cluster IMF Below 1 M_{\odot} . *ApJ*.
1354. A. Pasquali et al.: R4 and Its Circumstellar Nebula: Evidence for a Binary Merger? *AJ*.
1355. F. R. Ferraro, P. Montegriffo, L. Origlia and F. Fusi Pecci: A New IR-Array Photometric Survey of Galactic Globular Clusters: A detailed Study of the RGB Sequence as a Step Towards the Global Testing of Stellar Models. *AJ*.
1356. M. Kürster et al.: An Extrasolar Giant Planet in an Earth-like Orbit. Precise Radial Velocities of the Young Star ι Horologii = HR 810. *A&A*.

ESO, the European Southern Observatory, was created in 1962 to "... establish and operate an astronomical observatory in the southern hemisphere, equipped with powerful instruments, with the aim of furthering and organising collaboration in astronomy ...". It is supported by eight countries: Belgium, Denmark, France, Germany, Italy, the Netherlands, Sweden and Switzerland. ESO operates at two sites. It operates the La Silla observatory in the Atacama desert, 600 km north of Santiago de Chile, at 2,400 m altitude, where several optical telescopes with diameters up to 3.6 m and a 15-m submillimetre radio telescope (SEST) are now in operation. In addition, ESO is in the process of building the Very Large Telescope (VLT) on Paranal, a 2,600 m high mountain approximately 130 km south of Antofagasta, in the driest part of the Atacama desert. The VLT consists of four 8.2-metre and three 1.8-metre telescopes. These telescopes can also be used in combination as a giant interferometer (VLTI). The first 8.2-metre telescope (called ANTU) is since April 1999 in regular operation, and also the second one (KUEYEN) has already delivered pictures of excellent quality. Over 1200 proposals are made each year for the use of the ESO telescopes. The ESO Headquarters are located in Garching, near Munich, Germany. This is the scientific, technical and administrative centre of ESO where technical development programmes are carried out to provide the La Silla and Paranal observatories with the most advanced instruments. There are also extensive astronomical data facilities. In Europe ESO employs about 200 international staff members, Fellows and Associates; in Chile about 70 and, in addition, about 130 local staff members.

The ESO MESSENGER is published four times a year: normally in March, June, September and December. ESO also publishes Conference Proceedings, Preprints, Technical Notes and other material connected to its activities. Press Releases inform the media about particular events. For further information, contact the ESO Education and Public Relations Department at the following address:

EUROPEAN
SOUTHERN OBSERVATORY
Karl-Schwarzschild-Str. 2
D-85748 Garching bei München
Germany
Tel. (089) 320 06-0
Telefax (089) 3202362
ips@eso.org (internet)
URL: <http://www.eso.org>

The ESO Messenger:
Editor: Marie-Hélène Demoulin
Technical editor: Kurt Kjær

Printed by
J. Gotteswinter GmbH
Buch- und Offsetdruck
Joseph-Dollinger-Bogen 22
D-80807 München
Germany

ISSN 0722-6691

1357. K. Adelberger: Star Formation and Structure Formation at $1 \leq z \leq 4$. *Clustering at High Redshift*, ASP Conference Series, Vol 1999, A. Mazure and O. LeFevre, eds.
1358. J.U. Fynbo, W. Freudling and P. Møller: Clustering of Galaxies at Faint Magnitudes. *A&A*.
1359. M.-H. Ulrich: The Active Galaxy NGC 4151: Archetype or Exception? *A&A Review*, Variability of Active Galactic Nuclei. Contribution for the *Encyclopedia of Astronomy and Astrophysics*, Oxford Institute of Physics and McMillan Publ. Co. 1999.
1360. T. Broadhurst and R.J. Bouwens: Young Red Spheroidal Galaxies in the Hubble Deep Fields: Evidence for a Truncated IMF at $\sim 2 M_{\odot}$ and a Constant Space Density to $z \sim 2$.
1361. G. A. Wade et al.: Magnetic Field Geometries of Two Slowly Rotating Ap/Bp Stars: HD 12288 and HD 14437. *A&A*.
S. Hubrig et al.: Rapidly Oscillating Ap Stars versus Non-Oscillating Ap Stars. *A&A*.
M. Gelbmann et al.: Abundance Analysis of roAp Stars. V. HD 166473. *A&A*.
1362. F. R. Ferraro et al.: Another Faint UV Object Associated with a Globular Cluster X-Ray Source: The Case of M92. *ApJ*.
1363. A. Grazian et al.: The Asiago-ESO/RASS QSO Survey. I. The Catalog and the Local QSO Luminosity Function. *AJ*.

NEW ESO PROCEEDINGS AVAILABLE

The Proceedings of the Bäckaskog Workshop on

EXTREMELY LARGE TELESCOPES

(ESO Conference and Workshop Proceedings No. 57)

have been published. The 306-page volume, edited by Torben Andersen, Arne Ardeberg and Roberto Gilmozzi, is available at a price of DM 60.- (prepayment required).

Payments have to be made to the ESO bank account 2102002 with Commerzbank München, or by cheque, addressed to the attention of

ESO, Financial Services, Karl-Schwarzschild-Str. 2,
D-85748 Garching bei München, Germany

Contents

Successful Commissioning of UVES at Kueyen	1
TELESCOPES AND INSTRUMENTATION	
S. D'Odorico: UVES at Kueyen: Bright Prospects for High-Resolution Spectroscopy at the VLT	2
R. Hanuschik and P. Amico: VLT Pipeline Operation and Quality Control: FORS1 and ISAAC	6
B. Leibundgut, B. Pirenne, M. Albrecht, A. Wicencac and K. Gorski: Access to VLT Data in the ESO Archive	12
M. Sarazin: Chile Astroclimate, a Biannual Update	13
R. Heald and R. Karban: ESO Demonstration Project with the NRAO 12-m Antenna	14
O. Hainaut and the NTT Team: News from the NTT	15
New Pictures from Paranal Observatory	15
REPORTS FROM OBSERVERS	
E. Tolstoy, J. Gallagher, L. Greggio, M. Tosi, G. De Marchi, M. Romaniello, D. Minniti and A. Zijlstra: Imaging With UT1/FORS1: The Fossil Record of Star-Formation in Nearby Dwarf Galaxies	16
M. Franx, A. Moorwood, H.-W. Rix, K. Kuijken, H. Röttgering, P. van der Werf, P. van Dokkum, I. Labbe and G. Rudnick: FIRES at the VLT: the Faint InfraRed Extragalactic Survey	20
R.P. Mignani, P.A. Caraveo and G.F. Bignami: Optical Observations of Pulsars: the ESO Contribution	22
P. Rosati, C. Lidman, R. Della Ceca, S. Borgani, M. Lombardi, S.A. Stanford, P.R. Eisenhardt, G. Squires, R. Giacconi and C. Norman: The ROSAT Deep Cluster Survey: Probing the Galaxy Cluster Population out to $z = 1.3$	26
P. Møller: Spectral PSF Subtraction I: The SPSF Look-Up-Table Method ...	31
P. Møller, S.J. Warren, S.M. Fall, P. Jakobsen and J.U. Fynbo: SPSF Subtraction II: The Extended Ly α Emission of a Radio Quiet QSO	33
B. Leibundgut, J. Sollerman, C. Kozma, C. Fransson, P. Lundqvist, F. Ryde and P. Woudt: The Late Phase of SN 1998bw	36
J.-M. Conan, T. Fusco, L. M. Mugnier and F. Marchis: MISTRAL: Myopic Deconvolution Method Applied to ADONIS and to Simulated VLT-NAOS Images	38
A New Look at the Sombrero Galaxy	45
ANNOUNCEMENTS	
CERN, ESA and ESO Launch "Physics On Stage"	46
ALMA Science Advisory Committee	46
ESO Studentship Programme	47
Personnel Movements	47
Scientific Preprints	47